Materials Advances

ROYAL SOCIETY OF CHEMISTRY

REVIEW

View Article Online
View Journal | View Issue

Cite this: *Mater. Adv.*, 2021, 2, 6942

Crystal facet and surface defect engineered low dimensional CeO_2 (0D, 1D, 2D) based photocatalytic materials towards energy generation and pollution abatement

S. Sultana, S. Mansingh and K. M. Parida *

Surface defect engineering and crystal facet engineering are two important strategies which effectively enhance the efficiency of a photocatalyst by modulating its physiochemical properties. To date, surface defect and morphology dependent photoactivity has been explored by using different nanostructured photocatalysts. Among them CeO_2 based materials have recently received foremost interest, due to their easily tunable surface structure and low formation energy for surface defects. Therefore, in this review we have comprehensively summarized the recent achievements and progress in surface defect enriched low dimensional nanostructured CeO_2 and CeO_2 based heterostructure photocatalysts towards clean fuel generation reactions such as water splitting, CO_2 reduction, N_2 fixation and organic/inorganic environmental pollutant removal applications. The present review highlights the design of CeO_2 with particular crystal facets and morphology and the positive impact of the crystal facets on the construction of different CeO_2 based heterostructure materials (0D–2D, 0D–1D, 1D–2D, 2D–2D, 0D–3D, *etc.*) with other low dimensional photocatalysts. Next, the surface defects, crystal facets and heterojunctional interfaces responsible for improved photoactivity are briefly discussed with proper experimental evidence and the mechanism along with the theoretical concept is explained. Further, this review sheds light on the current challenges and future perspectives in this research area.

Received 21st June 2021,
Accepted 5th September 2021

DOI: 10.1039/d1ma00539a

rsc.li/materials-advances

1. Introduction

Energy shortage and environmental pollution are pressing concerns that adversely impact the sustainable development of our society. Hence, the development of green, sustainable and energy-efficient methods for energy production and pollutant detoxification is of utmost concern. With regard to this, semiconductor photocatalysis has gained enormous popularity as it can convert solar energy into some useful energy feedstocks and also act as a boon for remediation of environmental pollutants.[1–8] However, a major difficulty faced in this area is the low efficiency of the photocatalyst. The efficacy of a photocatalytic system generally depends upon three mechanistic features such as appropriate excitation, bulk diffusion and surface charge transfer.[9–12] In order to achieve the higher efficiency of a photocatalyst, all these three properties have to be controlled in a single platform. With the development of modern technology and advanced characterization techniques,

Centre for Nano Science and Nano Technology, SOA Deemed to be University, Bhubaneswar – 751 030, Odisha, India. E-mail: paridakulamani@yahoo.com, kulamaniparida@soa.ac.in; Fax: +91-674-2581637; Tel: +91-674-2379425

Dr Sabiha Sultana received her bachelor's degree (1st Rank) from Utkal University, Bhubaneswar, in the year 2012 and MSc in Chemistry from Ravenshaw University, Cuttack, in the year 2014. Then, she joined as a PhD student under the supervision of Prof. Kulamani Parida at the Centre for Nano Science and Nano Technology, S'O'A Deemed to be University, and recently completed her PhD degree. Her research area focuses on the development of nanostructured materials such as metal oxides, metal sulphides, and phosphides, and their application towards water splitting, N_2 reduction, CO_2 reduction, and pollution abatement. She has published 14 research articles in various international journals.

Dr Sriram Mansingh received his BSc (2nd Rank), MSc and MPhil (1st Rank) from Utkal University, India. Then, he completed his PhD degree at the Siksha 'O' Anusandhan (Deemed to be University) Bhubaneswar, India, under the guidance of Prof. Kulamani Parida. His current research mainly focuses on the development of nanostructured materials such as metal oxides, metal sulphides, and phosphides, and their application towards water splitting, N_2 fixation and organic/inorganic pollutant detoxification. He has published 24 research articles in various international journals and one patent.

the terminologies surface defect engineering and crystal facet engineering have come to light very recently.[13–15] It is found that either of these two approaches is a game changing entity for enhancing the reactivity and selectivity of a photocatalyst by modulating its physical and chemical properties.

Crystal facet engineering can efficiently modify the kinetic parameters responsible for the improved charge pair transfer and separation parameter and reaction rates of a photocatalytic reaction. In brief, morphologies with different exposed facets have different atomic rearrangement and co-ordination, and hence different morphologies exhibit different surface electronic structures (band gap, band edge potential, *etc.*), electrical conductivity, surface built-in electric field, reaction centers and reactant adsorption sites.[16–19] By simply changing an exposed plane to another one, there is a drastic change in the photoactivity and selectivity of a photocatalyst for a photocatalytic reaction[15], so there is an increased interest in morphology tuning and crystal facet engineering. While considering a multicomponent system, crystal facet engineering in nanostructured hybrids is quite complicated, as a heterostructural interface is evolved between the individual components. Those hybrids possess individual components with their own crystal planes of different orientation as well as a distinct interface with different band energy alignment. In most of the cases, proper band alignment at the interface between two individual components is found to be very crucial for interfacial charge transfer and separation. Hence the rational design of photocatalytic systems with active surface planes and suitable interfaces is very challenging.[20–26] The Arienzo group prepared TiO_2 with (001) and (101) exposed facets by using a morphology directing agent. Both theoretically and experimentally, they proved that the 001 surface is more active for photocatalytic oxidation reaction while the exposed 101 surface is a reductive surface, as it didn't directly assist the oxidative process.[22] In another example, Bomio *et al.* prepared a $PbMoO_4$ photocatalyst with predominant 111, 100, 011 and 110 facets by using a template directing agent. They found that the 001 surface exhibited the lowest activity for RhB photodegradation as the surface acts as a recombination centre of photogenerated electrons and holes.[23] Further, Zhu *et al.* prepared 010 and 011 facet exposed $BiVO_4$. They found that the morphology and the distinct facets play a vital role in the anisotropic charge distribution at the photocatalyst surface. For the 011 facet the surface photovoltage signal was 70 times higher than that on the 010 facet; hence the former could be a better photocatalyst.[24] Further, Naresh *et al.* explained the interaction of two exposed facets of two individual components in a heterostructure. They reported that 110 exposed Cu_2O (rhombic dodecahedra) was a more active photocatalyst towards MO degradation than 111 exposed Cu_2O (octahedral), while cubic 100 exposed facet Cu_2O is photocatalytically inactive. But when these are made into heterostructures with 200 exposed ZnS, $Cu_2O(111)$/ZnS(200) performed well in comparison to $Cu_2O(110)$/ZnS(200). The reason was attributed to the unfavourable band alignment within $Cu_2O(110)$ and ZnS(200), showing the lowest charge separation efficiency.[25] Hence photocatalytic activity is also strongly related to the exposed facet as well as their interfacial interaction.

Surface defects are another interesting feature which has a positive role in enhancing the photoactivity of a photocatalyst; hence defect engineering is catching more scientific significance for modifying the properties of a photocatalyst. In general, defects are created in a slightly reductive environment where the periodic arrangement is broken with little lattice distortion, and this can change intrinsic semiconductor properties such as orbital hybridization, conductivity, atom coordination number, and light absorption ability and can also change the electron density around the Fermi level.[27–30] Basically there are two types of defects, *i.e.* bulk defects and surface defects, and among these two, surface defects enhance the charge separation efficiency of a photocatalyst while bulk defects act as a recombination center for photogenerated charge carriers.[31,32] The surface defects are again classified into many divisions on the basis of dimension such as point defects, line defects, planar defects and volume defects. Surface anion vacancies (oxygen, sulphur and nitrogen) are regarded as the most explored type of vacancy which are employed in photocatalysis to modify the activity of the photocatalyst by enhancing its light absorption ability and charge transfer and separation efficiency and drive the surface reactions.[33,34] Moreover, in a multicomponent nanohybrid, additional defects, *i.e.* interfacial defects, are found which enhance the photoactivity by accelerating the interfacial charge pair separation.[35] However the controlled design of desirable vacancies in single and multicomponent photocatalysts without complete lattice distortion is very demanding. Hence, many studies have been concentrated on the design of a photocatalytic system with the combination of both surface defects and exposed crystal facets. For example, Li *et al.* prepared an oxygen vacancy enriched BiOBr(001) nanosheet and tested its effectivity towards the photocatalytic nitrogen reduction reaction. They found that the

Prof. Kulamani Parida is a globally distinguished scientist in the area of materials science, catalysis and nanotechnology. He superannuated as a Chief Scientist and a Professor of Academy of Scientific and Innovative Research (AcSIR) from CSIR-IMMT, Bhubaneswar, in 2014. His adoration for Chemistry and passion towards research couldn't let Prof. Parida sit idle after retirement. With the same devotion and dedication, Prof. Parida (Director) started the 'Centre for Nano Science and Nano Technology' a research unit of Siksha 'O' Anusandhan (deemed to be university), Bhubaneswar. His research interests include the design and development of advanced materials encompassing a wide variety such as metal oxides/phosphates/sulfates, cationic and anionic clays, perovskites, MOFs, carbon based materials including graphene, g-C_3N_4, and naturally occurring materials such as manganese nodules, manganese nodule leached residues, and manganese oxides of natural origin for fine chemical, energy and environmental applications. He has published more than 500 research articles and 10 review articles in renowned international journals. He has 18 524 citations to his credit with an h-index of 72 and an i10-index of 326. He has 27 national and international patents to his credit and is the author of four book chapters. For more details: https://kmparidaimmt.weebly.com/.

oxygen vacancy centres successfully activated the adsorbed nitrogen on BiOBr by π-back donation and significantly promoted the interfacial electron transfer from BiOBr to the activated nitrogen.[36] In another report, Zhang *et al.* designed a defect enriched WO_3 nanosheet and found that the as-prepared photocatalyst efficiently coupled sunlight into aerobic coupling of amines to the corresponding imines with excellent stability and enhanced the kinetic rate 6 times compared with defect deficient WO_3. They deduced that defect engineering can serve as a versatile approach to refine the photocatalyst.[37] Apart from the surface defects, interfacial defects in a heterojunction photocatalyst also play a vital role in photocatalysis. Zhang *et al.* successfully prepared a heterostructure between MoS_2 QDs and $ZnIn_2S_4$ in a 2-D architecture with interfacial S-vacancies. The vacancies acted as electron traps and avoided the vertical transmission of electrons.[38] Hence the heterostructure exhibited a high photocatalytic hydrogen evolution rate, which was higher than that of neat systems without vacancies.

Rare earth cerium oxide (CeO_2) is considered as one of the most attractive metal oxides which can easily be tuned into different shapes with desired exposed facets. Further, another feature, *i.e.* surface defects, can easily be formed with very slight energy expense at the CeO_2 surface. Due to these special features, it is often used as a catalyst in various catalytic applications such as solid oxide fuel cells (SOFCs), ultraviolet adsorbents, glass polishing materials, water gas shift reaction, PROX (CO oxidation), oxygen sensors, selective organic transformation, photocatalytic water oxidation and pollutant degradation.[27,39–43] In addition to this, CeO_2 has other special features such as cost-effectiveness, high stability, low toxicity and specific physical and chemical characteristics, such as high oxygen storage capacity (OSC), oxygen ion conductivity and fast shuttling of oxidation state ($Ce^{3+} \rightarrow Ce^{4+}$), which makes it an ideal candidate for photocatalysis.[44–59] In brief, the rare earth CeO_2 has a crystal structure of triclinic, tetragonal or cubic phase. However, mostly CeO_2 crystallizes in the cubic fluorite structure with a space group of $Fm\bar{3}m$ (a = 0.541134 nm) over the temperature range extending from room temperature to its melting point.[48] The fluorite structure consists of a face centred cubic unit cell of Ce^{4+} while eight oxygen anions occupy the tetrahedral interstitial sites. As a result, each Ce^{4+} is octahedrally coordinated by eight oxygen anions while each oxygen ion is tetrahedrally coordinated by four Ce^{4+} cations forming a CeO_8 cluster as the basic unit. In cubic CeO_2, mainly three exposed planes (111), (110) and (100) are observed, but due to thermodynamic restrictions, CeO_2 predominantly exposes the (111) plane, as it is very stable and requires low surface energy. The (111) surface plane is terminated by three-fold co-ordinated oxygen atoms, while the polar (100) surface is terminated by two-fold co-ordinated oxygen atoms. The (110) surface is terminated by a CeO_2 plane with three-fold co-ordinated oxygen and six-fold co-ordinated cerium atoms.[29]

Surface defects especially oxygen vacancies are termed as the most important feature of CeO_2, which regulates all its properties. In a slightly reductive environment or at a low partial pressure of oxygen, surface defects (oxygen vacancies, interstitial metal defects) are generated on CeO_2, as they require low formation energy. In brief, surface defects in CeO_2 are generally created when the on plane oxygen is released from the lattice yielding a CeO_7 type cluster with the concomitant oxygen vacancy formed in the crystal lattice. Further, these vacancies are accompanied by localization of the electrons left behind in the Ce 4f state leading to the formation of two Ce^{3+} ions. Hence, altogether oxygen vacancies and Ce^{3+} are termed as surface defects on CeO_2 as shown in Fig. 1(a).[50,51] The reaction of defect formation is as follows,[51] where $O_O^{\times}$ is the oxide ion in the lattice, $V_O^{\bullet\bullet}$ is the charged oxygen vacancy and e′ represents the electrons in the conduction band:

$$O_O^{\times} \leftrightarrow V_O^{\bullet\bullet} + 2e' + 1/2O_2(g)$$

In addition to the doubly charged oxygen vacancy, singly charged and neutral vacancies are also present in the defective CeO_2 lattice.[54] Huang *et al.* reported a neutral oxygen vacancy $\left(V_O^0\right)$ centre in CeO_2 with very low formation energy in an oxygen-deficient environment. It acts as a deep donor with negative U (repulsive potential) behaviour leading to excellent photoactivity. In addition to this, easy shuttling of $Ce^{3+\leftrightarrow 4+}$ helps to generate an anion Frankel defect which enhances oxygen storage as well as release capability.[52] Further, to know the structure and geometry of oxygen vacancies, Esch *et al.* thoroughly studied the defect formation and nature of defects from STM images and DFT calculations. They found that two types of oxygen vacancies are predominantly formed: the first type is the simple one oxygen vacancy which appears as a depression surrounded by three lobes, shown by the magenta triangle in Fig. 1(b), and the second type, which is called the subsurface vacancy, appears as triple protrusions centred on third layer oxygen sites (shown by the cyan triangle in Fig. 1(b)). The delocalization of the electron left behind determines which type of vacancy can be formed on CeO_2. Hence, a permutation and combination of single and subsurface oxygen vacancies creates different dimeric and trimeric vacancy clusters with different orientation, which causes a major structural rearrangement in the crystal lattice of CeO_2.[57]

Next is the optical property of CeO_2. Theoretically the optical band gap of CeO_2 is 6–8 eV because of the transition between O 2p and Ce 5d states.[49] And, the experimental result reveals a bandgap of around 3 eV due to the charge transfer spectra of Ce(IV)–O(II), while the band gap may vary from 3.2 to 2.8–2.7 eV. The drastic change in the band gap and in the colour from yellow to blue-black arises only due to the presence of surface defects in CeO_2.[53] The change is due to the oxygen vacancy, which creates a Ce^{3+} state; thus the energy of the 4f orbitals shifts towards lower potential and hence shortens the bandgap. The density of state (DOS) of Ce 4f for Ce(III) is larger than that of Ce(IV) in the positive energy range, which indicates that Ce(III) can be more easily excited than Ce(IV) under light irradiation, which suggests that the oxygen vacancy enhances visible light absorption.[55] In addition to the optical property, the oxygen vacancy of CeO_2 also has a profound effect on the electrical as well as magnetic character. With the increase in oxygen vacancy concentration, the movement of the oxygen atom becomes

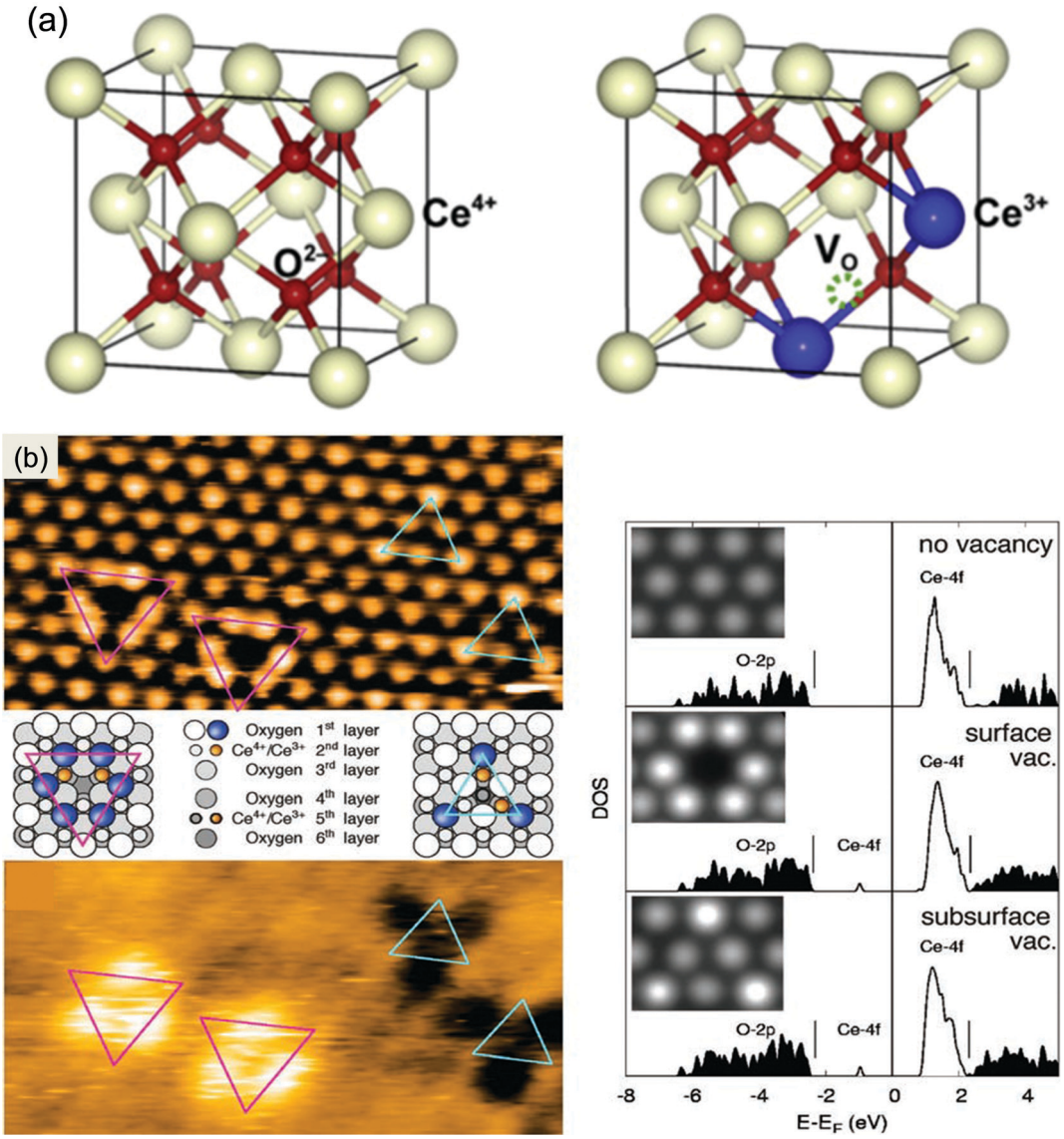

Fig. 1 (a) Crystal structure of CeO_2 with the formed oxygen vacancy. Reprinted from ref. 50 with permission from Elsevier. (b) Filled-state and empty-state STM images of single and subsurface vacancies and related structural models and calculated density of states (DOS) and simulated filled-state STM images. Reproduced from ref. 57 with permission from Science.

easier in the crystal, as the vacancy easily migrates throughout the lattice *via* a vacancy hopping mechanism at an elevated temperature, and hence the crystal has a high electrical conductivity.[56–58] This increased diffusion rate in the lattice is a probable cause of the increase in catalytic activity.[58] Chen *et al.* reported that the intrinsic surface defects also have a direct relationship with the magnetic behaviour of CeO_2. They found that an increase in the local oxygen vacancies and Ce^{3+} concentration directly increases the magnetism of CeO_2 nanoparticles. However, after a certain concentration of Ce^{3+} the magnetic properties gradually decrease and vanish completely. The reduction of magnetic moments may be due to ion pair formation by oxygen vacancies which favours antiferromagnetism. Further, from the X-ray magnetic circular dichroism measurement and theoretical analysis, they found that the electrons in Ce bear magnetic moments and show magnetism *via* bound magnetic polarons which are constituted by oxygen vacancies and an oxygen mediated super-exchange framework (Ce^{3+}–O–Ce^{3+}).[5] Therefore it is confirmed that oxygen defects and shuttling of oxidation states in CeO_2 lead to some peculiar changes in optoelectronic, electrical as well as magnetic properties.

Another interesting feature of ceria is its morphology variation; ceria can be easily tailored to different morphologies such as nanorods, nanotubes, nanocubes, nanopolyhedra, and nanosheets with exposed active facets. Moreover, particle size and morphology have a prominent effect on the intrinsic surface defect formation in CeO_2. From the literature survey, it was found that the smaller the particle size is, the higher the surface to volume ratio will be, and hence the more defects there will be. Additionally, designing a particular shape or exposure of a specific plane in CeO_2 decides

the formation and concentration of defects. Based on the DFT calculation, the (100) plane exhibits the lowest energy for vacancy formation, while the (111) crystal plane requires more energy. So based on this, nanostructures of (100) and (110) exposed facets contain more surface defects than (111) oriented surface structures.[60–64] Wu's group evaluated the surface defects and and their relationship with the photoactivity of different exposed planes of three types of CeO_2 nanostructures such as nanorods, nanocubes and nano-octahedra. *Via* UV-Raman spectroscopy and O_2 adsorption analysis, they found that both oxidized and reduced CeO_2 of nanorod morphology ((110) + (100)) has the most intrinsic defects followed by nanocubes (100) and nano-octahedra (111). Furthermore, the team observed that some defects are of one electron containing singly charged species while some are two electrons containing doubly charged.[63] Recently by combining experimental and theoretical results, Oliveira and his group concluded that CeO_2 consisting of the (111) exposed plane contains only one vacancy, due to the presence of the $[CeO_7{\cdot}V_{\times}^{0}]$ cluster, while (100) and (110) crystal planes exhibit two vacancies, because of the presence of the $[CeO_6{\cdot}2V_{\times}^{0}]$ cluster. In the samples consisting of (100) and (110) facets with two vacancies, there is a resonance between the vacancies which stabilizes the interaction between electrons and holes. Moreover, the one vacancy containing facet shows higher stability for the formed holes only, which reduces the electrical resistance to some extent. Hence the morphology containing (100) and (110) planes shows higher photoactivity and lower electrical resistance than the (111) plane containing morphology.[54] In most cases, surface defects, exposed planes and morphology of CeO_2 are the key factors that decide the enhancement in catalytic as well as photocatalytic activity.[62–64] However, the vacancies can easily be healed in an oxidative environment (O-rich) and sometimes act as hole trapping centers which retards photo-efficiency. Importantly, designing a specific facet exposed system is very challenging. So fabricating CeO_2 based nanomaterials with controlled surface defects and a well compatible merged facet interface is getting more attention and interest.

Therefore more emphasis has been given to the construction of hybrid/heterostructure based photocatalytic systems for potential application in the photocatalysis field. So far many such CeO_2 based photocatalytic systems have been made and from the recent studies it was found that the construction of heterostructure photocatalysts of different morphologies, with other visible light semiconductors, is a feasible and effective method to improve the photogenerated electron–hole separation which ultimately improves the photocatalytic efficiency under visible light. In this approach, a wide bandgap metal-oxide semiconductor, *i.e.* CeO_2, is often combined with a narrow bandgap semiconductor such as other metal oxides, sulphides, phosphides, and selenides to form a heterostructure oriented system.[45–48] Further, the *in situ* generation of surface defects helps to minimize the hole–electron recombination and provides a strong interfacial surface for reactant binding and the corresponding dissociation, resulting in improved photoefficiency. Regarding this concept, several articles corresponding to the CeO_2 based photocatalytic systems have been published in the field of solar fuel generation and pollutant removal, which we have discussed in the application section.

Nanostructured CeO_2 has witnessed numerous possible scientific advancements and has always been the centre of attraction in photocatalysis, as summarized in Fig. 2. Currently, extensive studies have been made towards developing efficient CeO_2 based photocatalytic systems by adopting different advanced strategies such as surface interface tuning and defect engineering. Hence, there are several reviews on CeO_2 covering areas such as its properties, synthesis, nanostructure and catalytic application.[27,39,45–48] However, a systematic review on the current progress and growth trend of exposed facet and defect mediated CeO_2 based materials is highly needed to update the scientific society with regard to photocatalysis. So in this review, we have specifically discussed the strategic updates and the latest progress in exposed facet, morphology dependent CeO_2 with defect engineering and then CeO_2 based heterostructured materials towards various photocatalytic applications. In brief, the review elaborates the basic concepts and the design strategy of lower dimension (2D, 0D, 1D, 3D) CeO_2 with particular crystal facets and broadly summarizes the synthetic strategy involving CeO_2 based materials with a distinct

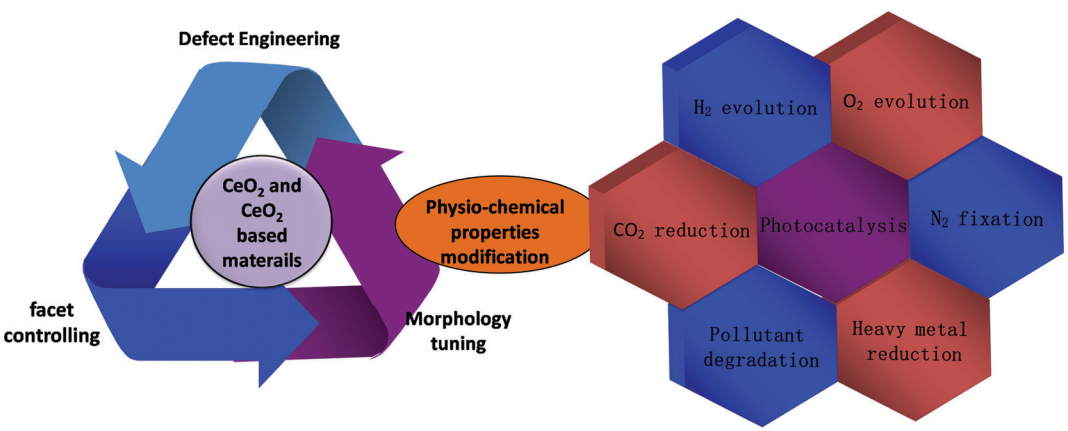

Fig. 2 Complete schematic illustration of CeO_2 based materials' property tuning and applications.

morphological interface such as 0D–2D, 0D–1D, 1D–2D, 2D–2D, 0D–3D, *etc.* Further, it also narrates the detailed defect chemistry of such heterointerface systems in different photocatalytic applications such as water splitting (H_2 and O_2 evolution), CO_2 reduction, N_2 reduction, and pollutant removal (dyes, phenolic derivatives, antibiotics and heavy metals) along with elucidation of morphology dependent activity correlations. At last, we throw some light on the challenges encountered and provide future direction for improvement of CeO_2 based materials to achieve benchmark efficiency.

2. Crystal facet engineering and defect designing

During the last two decades, several synthetic methods have been reported for the preparation of nanostructured CeO_2. Generally the methods used for the synthesis of shape and size selective CeO_2 with appropriate exposed active planes are precipitation, hydrothermal treatment, surfactant/capping agent-assisted solvothermal method, thermal decomposition, sol–gel combustion, template-directed synthesis, sonochemical method, microemulsion technique, electrochemical deposition and many more.[65–91] More often two or more methods are combined to prepare facet orientated CeO_2 as summarized in Fig. 3(a). Sun *et al.*, Zhang *et al.* and Wang *et al.* have thoroughly explained the hidden mechanism and the science behind the adopted strategy toward designing different shape-selective nanostructured CeO_2.[39,45,46] Hence, in this section, we have briefly summarized some of the essential points for the synthesis of lower-dimensional facet oriented CeO_2 and cited some latest examples of the corresponding synthesis.

The controlled nucleation and growth rate of CeO_2 crystals determines the formation possibility of a particular facet, size and shape. Hence, appropriate additives such as precipitating agents/mineralisers [NaOH, urea, HMT, ammonia, *etc.*], template [soft, hard and self], surfactant/capping agent, organic ligands, polymers, *etc.*, are often used to manage the exposed plane, shape and size of nanostructured CeO_2. For example, the commonly used solutions to obtain facet oriented CeO_2 are NaOH solution (cubes, rods, wire (110)), PO_4^{3-} (octahedral, rod), and $NH_3{\cdot}H_2O$ (nanowires). In addition to these, the concentration of precipitants and the reaction temperature and time are also important for obtaining different exposed facets.[65–96] Oliveria *et al.* prepared CeO_2 of different morphology by simply varying the synthesis time *via* microwave-assisted hydrothermal synthesis. They found that when using cerium nitrate and NaOH, at first they obtained sheet like morphology, and after a certain time these sheets were elongated to form nanorods while after some time polyhedron type morphology was obtained followed by nanocubes.[54] Further, it was reported that anions like Cl^-, NO_3^-, SO_4^{2-}, and PO_4^{3-} mainly coming from the cerium precursor and the added precipitants have also influenced the morphology and the properties of CeO_2. For example, Jiang *et al.* prepared CeO_2 nanocubes and nanorods by using two different cerium precursors; for nanocubes, they used cerium chloride while for nanorods they used cerium nitrate. After the hydrothermal treatment at 110 °C for only 24 h, from both cerium precursors in NaOH solution, they got rod like morphology, while a further higher temperature treatment (180 °C) yielded nanocube type morphology with only the chloride containing precursor.[15] In another report by Zhu *et al.*, 110 exposed facet nanorods were prepared from cerium chloride and NaOH *via* hydrothermal treatment at 140 °C for 18 h, while 100 exposed nanocubes were prepared from the same concentration of NaOH with cerium nitrate precursor at 180 °C for 24 h.[95] The controlled design of one kind of exposed facets requires more complicated reactions; hence in most of the cases nanostructured ceria is prepared by controlling the most active plane while other facets are also present but in a dormant form. Therefore a number of systematic studies on morphology oriented low dimensional nanostructured ceria with one (in some cases more than one) active facet have been carried out. From the conclusive research

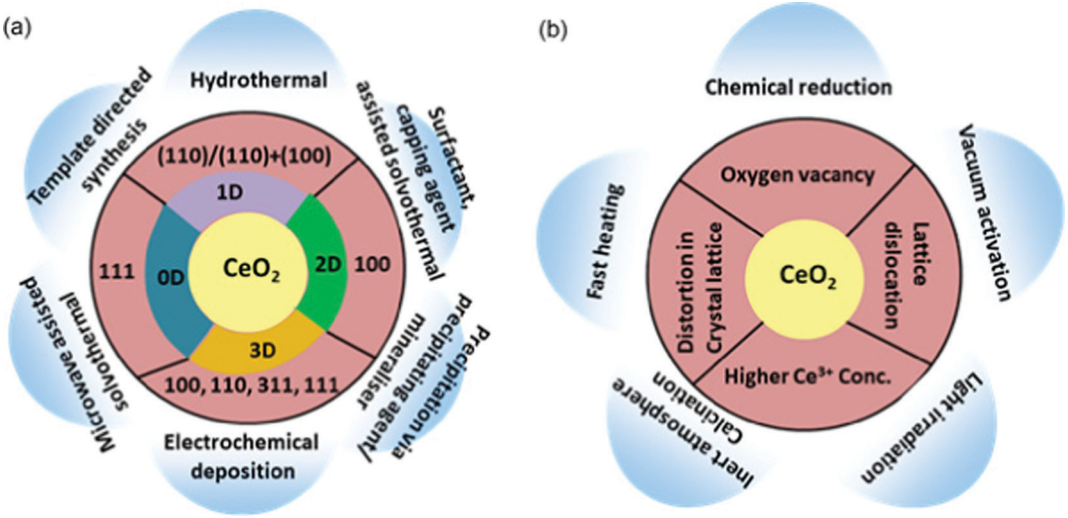

Fig. 3 (a and b) Strategy for crystal facet designing and defect engineering.

experiments it was found that by controlling the dimension of nanostructured CeO_2 the desired active crystal facets can be controlled simultaneously. For example, by making 1-D nanorods or nanowires, 110 + 100 exposed facets are controlled wisely, while high surface to volume ratio 100 planes are controlled by making 2-D nanosheet and 3D-nanocube like structures.[81,97,98] For example, Imagawa and Lin *et al.* prepared 100 exposed facet CeO_2 nanoplates by using oleic acid and oleylamine, while Hao *et al.* prepared monodispersed 100 exposed ceria nanocubes by a simple hydrothermal method by using decanoic acid as an organic surfactant.[99] In another report, a 200 exposed crystal facet CeO_2 nanocube was prepared by Yang *et al.* using *tert*-butyl amine as the facet directing agent.[100] Next, Liu *et al.* reported another CeO_2 morphology, *i.e.* an octahedron with a predominant 111 exposed facet, *via* a hydrothermal method followed by high pressure.[101] Hence, the synthesis of lower-dimensional CeO_2 with controlled exposed facets requires conceptual designing and experimental evidence, which we have briefly discussed in the below segments.

In addition to crystal facet engineering, surface defect designing is another crucial strategy for remodifying the photocatalyst property. Doping is considered as an effective strategy to generate defects in CeO_2; however, dopants form deep impurity levels within the forbidden band of semiconductors, where they act as recombination centres and impair photocatalytic activity.[102] So in this review we have excluded the doping concepts and their impact on CeO_2 based materials. Further, a number of synthetic methods such as chemical reduction, light irradiation, vacuum activation, inert atmosphere (N_2, Ar, H_2) calcination, *etc.* are often combined with the general nanostructured CeO_2 preparation methods to achieve higher defect density at the surface as schematically presented in Fig. 3(b).[28,103–106] Moreover, the different exposed facets exhibited different energy for vacancy formation. In general it is found that the 110 and 100 planes exhibited higher energy for surface vacancy formation while the 111 plane required a minimum energy. Among 110 and 100, 110 CeO_2 has lower energy for vacancy formation than 100 CeO_2. So *via* controlling the facets one can control the defects in CeO_2. To further enhance the vacancy concentration, additional treatments as mentioned above are considered. For example Zhang *et al.* prepared oxygen vacancy enriched CeO_2 nanorods by a one step hydrothermal method followed by *in situ* reduction treatment. Briefly, they used the cerium precursor and NaOH along with $NaBH_4$ and treated the solution hydrothermally. $NaBH_4$ here acts as a reducing agent and *in situ* generates oxygen vacancies during the growth of nanorods.[103] And in some cases $NaBH_4$ treatment was carried out after the complete preparation of CeO_2 to increase the surface defect concentration.[104] Next, Zhao *et al.* prepared defective CeO_2 NRs by a simple hydrothermal method followed by calcination in different atmospheres (such as argon, a mixture of argon and hydrogen gas and air atmosphere) at 800 °C. *Via* systematic analysis through XPS, they found that in an Ar–H_2 atmosphere maximum surface vacancies were produced, due to the reducing nature of hydrogen gas.[69] Further, Aslam *et al.* synthesized nanosized CeO_2 by using Triton X-100 as a surfactant *via* a solution combustion method followed by 500 °C calcination. They found that when the as-prepared CeO_2 was additionally treated with direct sunlight, some CeO_{2-x} was formed on the CeO_2 surface. This defective CeO_2 exhibited enhanced absorption in the visible region and its band gap reduced from 2.9 to 2.6 eV.[105] Hezam *et al.* reported another O_v enriched CeO_2 *via* a sunlight assisted combustion method. They found that more defects are present in CeO_2 prepared by the sunlight assisted combustion method compared to that by the conventional solution combustion method.[106]

3. Synthesis of nanostructured CeO_2 and CeO_2 based materials

3.1 Zero-dimensional CeO_2

In recent years 0D quantum dots (QDs) have attracted great attention due to their size-derived properties which keep them one step ahead of their corresponding normal nanoparticles. The quantum confinement effect modulated extraordinary opto-electronic properties and prominent active sites make zero-dimensional materials promising candidates in a variety of applications including photocatalysis, electrocatalysis and biocatalysis.[107] Different synthesis methods like non-hydrolytic sol–gel, hydrothermal, microwave-assisted solvothermal methods, *etc.*[65–68] with suitable capping agents have been reported for the synthesis of CeO_2 QDs. In this context, Xin *et al.* proposed a synthetic route to prepare monodisperse CeO_2 QDs by heating a cerium precursor in triethylene glycol (TEG). In short, they obtained uniform monodisperse 5 nm QDs *via* a facile low cost, polyol condensation route which is based on the hydrolysis of the cerium alkoxide complex at an elevated temperature in the presence of an organic solvent (TEG) as shown in Fig. 4(a). The prepared CeO_2 QDs show good redispersion ability and a high specific surface area.[65] Further, Hassan and co-workers suggested two methodologies for the preparation of different size CeO_2 QDs. In the typical hydrothermal process, they used a mixed solution of cerium precursor along with a particular molar concentration of bases (NaOH, NH_4OH) and obtained 7 nm size QDs. While in the next strategy, they obtained 3 nm QDs *via* the non-hydrolytic sol–gel method by using the cerium precursor in polyamine and then adding the organic capping agent diphenyl ether to control the size of the nanoparticles.[66] Moreover, in the above processes, more than one metal precursor was used in addition to the surfactant/capping agents which is quite essential for restricting the growth of QDs. In light of this, Lehne *et al.* used a single metal–organic precursor, *i.e.* a heteroleptic alkoxide complex of cerium, to obtain highly crystalline CeO_2 QDs with a narrow size distribution *via* the microwave-assisted solvothermal synthesis in *N*-methyl pyrrolidine.[67] Adding more to the text, for the biomedical application of quantum dots, their synthesis, storage and self-agglomeration were considered as serious parameters for their effective utilization. Hence incorporation of a suitable capping agent or organic moiety over the surface of QDs is an apparent solution. Arumugam's group synthesized 2.4 nm CeO_2 QDs capped with the anionic group 2-amino-3-chloro-5-trifluoromethyl pyridine (ACTP). From XRD it

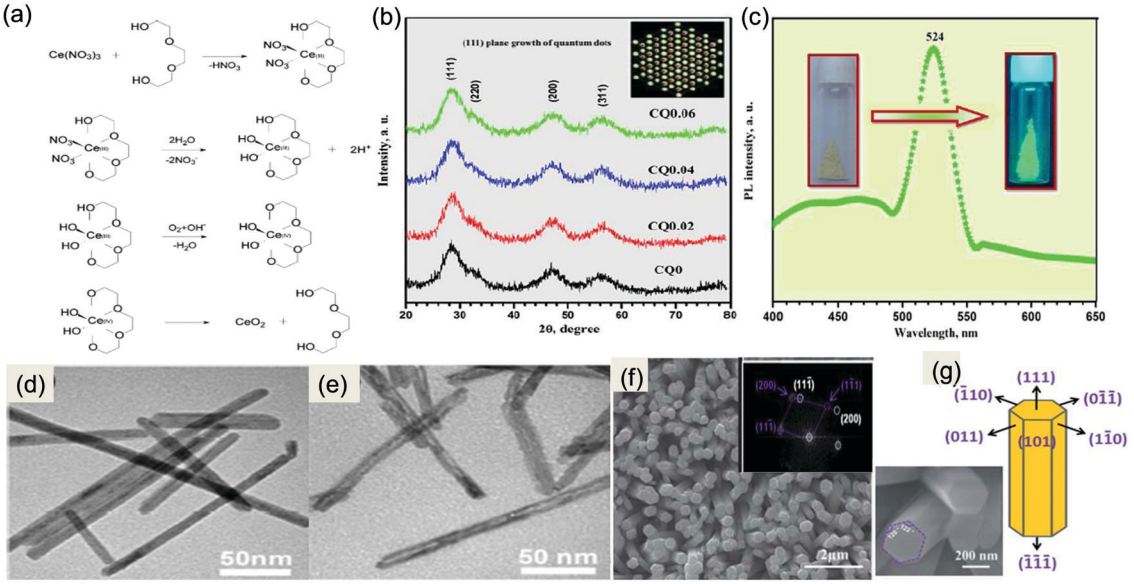

Fig. 4 (a) Proposed mechanism for Ce chelated complex formation with the corresponding decomposition to quantum dots. Reprinted from ref. 65 with permission from Wiley. (b) and (c) XRD pattern of plane and ACTP capped CeO_2 QDs; (inset) schematic (111) plane growth of QDs and PL spectrum of CeO_2 QDs, exhibiting strong green emission at 524 nm. Reprinted with permission from ref. 68, copyright 2016 American Chemical Society. (d) and (e) TEM micrographs of CeO_2 nanorods and nanotubes. Reprinted from ref. 70 with permission from Springer Nature. (f) SEM images and FFT pattern showing the single-crystalline nature. (g) Schematic diagram of facet oriented CeO_2 NRs and its resemblance with the FESEM image (inset).[76] Reproduced by permission of The Royal Society of Chemistry.

was observed that capped as well as uncapped QDs exhibited a dominant (111) plane as shown in Fig. 4(b), and the QDs' orientation was along the 110 direction. Further, they found another interesting fact, *i.e.* the synthesized QDs exhibited strong green emission at 295 nm (Fig. 4(c)), which confirms that the synthesized sample was in the quantum range with particle size ~2.4 nm that is below its Bohr radius of 7–9 nm. Furthermore, it was found that due to the dielectric confinement effect the band gap energy values of QDs gradually decreased with the increasing amount of the capping agent, which is a good sign for photocatalysis.[68]

3.2 One-dimensional CeO_2

One-dimensional (1D) nanostructures (nanowires, nanorods and nanotubes) have been intensively researched due to their fascinating physical and structural behaviour along with high chemical reactivity. Because of their high aspect ratio, they are beneficial for many potential technological applications.[108] Different mediators such as mineralizers, organic solvents, and surfactants are used to kinetically control the 1D anisotropic crystal growth and other parameters like temperature, pH, concentration, *etc.* are also optimized for obtaining a thermodynamically favoured 1D structure.[69–77,104] Zhao *et al.* prepared single-crystalline nanorods *via* the hydrothermal method (140 °C for 56 h) by using $NH_3{\cdot}H_2O$ as an alkaline agent without the use of any surfactant or capping agent followed by calcination.[69] The study showed that the additional use of a capping agent/surfactant increases the probability of one-dimensional growth at lower temperature and consumes less time.[54–60] Further, Cao *et al.* reported an interesting methodology (etching–dissolution–deposition) for the preparation of hollow nanotubes at low temperature. In this procedure, they first prepared CeO_2 nanorods hydrothermally by using NaOH as a precipitating agent, and then they added a Ce salt precursor to the prepared CeO_2 nanorod suspension under heating to obtain CeO_2 nanotubes. They proposed that the surface Ce^{3+} underwent hydrolysis and further dissolution at the tips of the nanorods resulting in nanotube formation. Further, the redeposition and crystallization on the outer sides of the nanorods yielded CeO_2 nanotubes of an average diameter of 11.8 nm, as shown in Fig. 4(d and e).[70] In another work, Kuiry *et al.* prepared CeO_2 nanotubes of diameter 40 nm and length 250 nm by using bis(2-ethylhexyl)sulfosuccinate sodium salt (AOT) as a surfactant in toluene–water solvent through the micro-emulsion technique.[72] Besides, 1D CeO_2 has been synthesized by using some hard templates such as AAO, ZnO, $K_xMn_yO_z$, *etc.* as these substrates encourage 1D nucleation.[73–75] For example, Wu's team first prepared $K_{1.33}Mn_8O_{16}$ nanowires through the hydrothermal technique and then deposited CeO_2 over them by a second hydrothermal treatment. The $K_{1.33}Mn_8O_{16}$ nanowire template was instantaneously removed due to the release of an excess of HNO_3 during the precipitation of CeO_2 in the second hydrothermal treatment, leaving behind CeO_2 nanotubes with a diameter of 90 ± 10 nm which fits with the diameter of $K_{1.33}Mn_8O_{16}$ nanowires.[75] Furthermore, the electrochemical deposition technique is now more popular for the growth of 1D nanostructures like nanorods and nanotubes over a conductive substrate.[76,77] Lu *et al.* reported hexagonal CeO_2 nanorods with prominent (110) exposed planes by a facile cathodic electrodeposition technique over a Ti substrate using $Ce(NO_3)_3{\cdot}6H_2O$, NH_4Cl, and KCl chemicals at a current density of 0.5 mA cm^{-2}.

They found that the average diameter of the grown nanorods was about 200–400 nm and the length was up to 800 nm as shown in Fig. 4(f and g), while two sets of diffraction spots in the FFT pattern as shown in the inset of Fig. 4(f) confirmed the single crystalline nature with some defects.[76] And Zhang *et al.* fabricated nanorod and nanowire CeO_2 over a Cu substrate by using the same nitrate precursor at a current density of 0.44 mA cm^{-2} and 0.88 mA cm^{-2} respectively for 2 h at 70 °C. They found well-aligned CeO_2 nanorods with an average diameter of about 200 nm while the diameter of nanowires was about 80 nm.[77]

3.3 Two-dimensional CeO_2

Recently 2D materials have attracted a lot of interest because of their size-derived special properties such as high conductivity, high mobility, high mechanical strength and large spin diffusion length. Their excellent properties make them an outstanding material for many catalytic and energy applications.[109] Metal oxide semiconductors, *i.e.* CeO_2, with a cubic crystal structure have no intrinsic driving force for 2D anisotropic growth.[78] So, the synthesis of 2D CeO_2 is generally carried out by using a template/surfactant/mineraliser for controlling the crystal growth along two or more facets.[78–83] Yu *et al.* synthesized CeO_2 nanosheets *via* a two-step hydrothermal treatment. At first, the inorganic–organic Ce–EDA hybrid nanorods were prepared by using a hydrothermal reaction at 150 °C between 1,2-ethanediamine (EDA) and $Ce(OAc)_3$. Then, the hybrid nanorods were again hydrothermally treated at 280 °C to form single-crystal-like $CeOH(CO)_3$ nanosheets which were further calcined to obtain 2.4 nm thick ultrathin mesoporous CeO_2 nanosheets as schematically represented in Fig. 5(a).[79] Further, Yu and his research team described the synthesis of ultrathin ceria nanosheets by using a single surfactant/stabilizer (6-amino hexanoic acid) only. They found that the thickness of the nanosheet was approximately 2.2 nm and the lateral dimension was up to 4 mm as shown in Fig. 5(b and c). In the preparation procedure, at first small ceria nanocrystals stabilized by AHA were formed, and later these crystals were organized into ultrathin nanosheets through 2D self-assembly, followed by an *in situ* re-crystallization process.[78] Huang *et al.* prepared 2D CeO_2 nanosheets through electrochemical anodic deposition methods (0.2 mA cm^{-2} for 60 min at 70 °C) over a substrate by using cerous nitrate and NH_4NO_3.[80] Likewise, Wang *et al.* reported ultrathin ceria nanoplates *via* a simple and robust solution-phase synthesis method where a soft

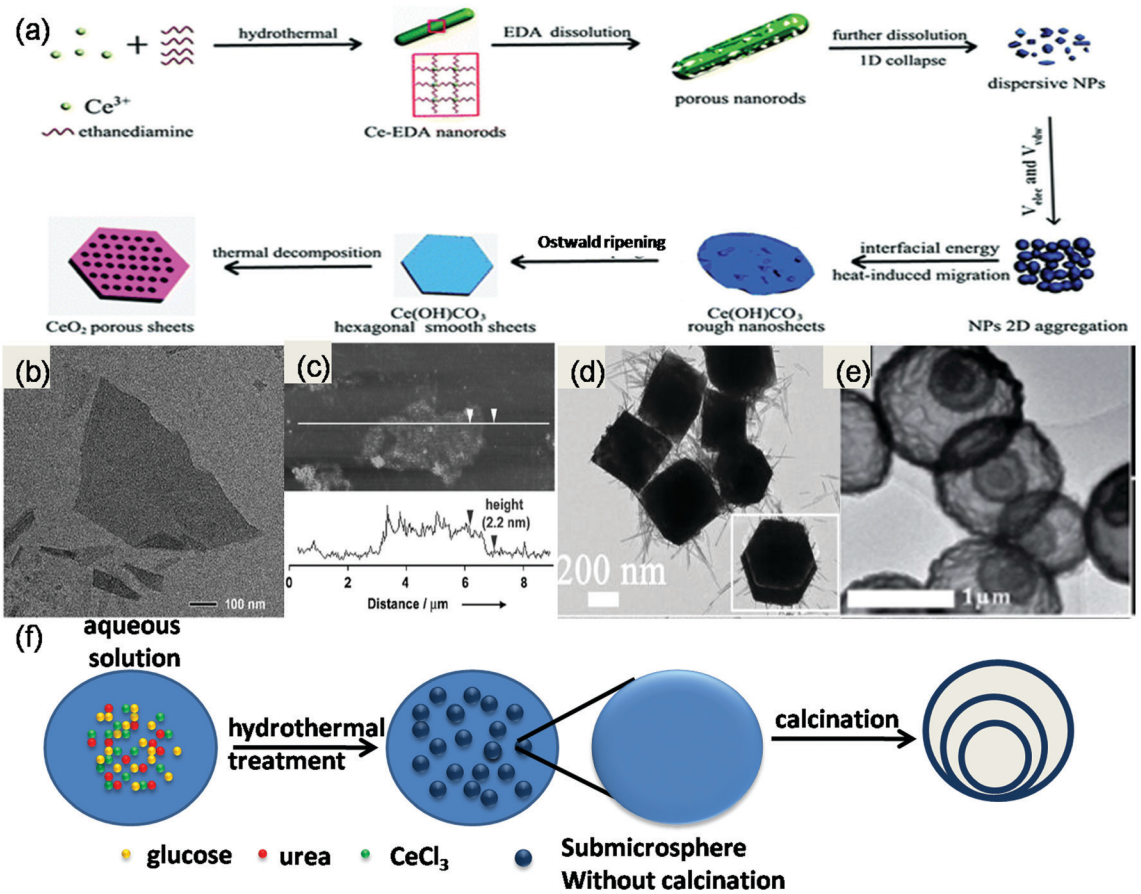

Fig. 5 (a) Structure evolution mechanism of porous CeO_2 sheets.[79] Reproduced by permission of The Royal Society of Chemistry. (b) and (c) Ultrathin CeO_2 nanosheets with AFM showing the single-crystalline nature. Reprinted from ref. 78 with permission from Wiley. (d) TEM micrographs of hexahedron prism anchored octahedral CeO_2. Reprinted with permission from ref. 84, copyright 2015 American Chemical Society. (e) TEM micrographs of multishell CeO_2 and (f) complete synthetic route for preparation of this.[91] Reproduced by permission of The Royal Society of Chemistry.

surfactant (oleic acid or oleylamine) was used in the presence of a mineraliser (sodium diphosphate or sodium oleate) to prepare highly efficient ceria nanoplates. They concluded that thickness and morphology solely depend upon the reaction time. And the nanoplates possessed a high surface to volume ratio and the desirable high OSC(100) plane.[81]

3.4 Three dimensional CeO_2

The three-dimensional nanoarchitecture with a large aspect ratio, high porosity, high surface area and high oxygen storage capacity has emerged as a promising candidate for different types of catalytic oxidation reactions.[110] Generally, template or surfactant-assisted methods are applied to synthesize 3D (prism, octahedron, ordered mesoporous, sphere, hollow architecture, *etc.*) CeO_2 materials.[84–91] Li *et al.* synthesized hexahedron prism anchored octahedral 3D CeO_2 by using phosphate ions as a mineraliser through a simple hydrothermal method, where the nanorods emerged out from the tinctured octahedra as shown in Fig. 5(d). The unique hierarchical 3D structure provides selected redox facets and spatial charge separation sites, which are quite effective in enhancing the photocatalytic activity.[84] A pillow like CeO_2 microstructure of 10 μm length and 4 μm width was prepared by Han and co-workers by a facile solvothermal method by using a cerium salt and ammonium nitrate as starting materials at pH 10. The obtained CeO_2 pillows have a BET surface area of 191 $m^2\ g^{-1}$ and a pore diameter ranging from 2 to 10 nm.[85] Through a novel hydrothermal method followed by a controlled calcination method, Sun *et al.* prepared monodisperse flowerlike CeO_2 microspheres containing a micro/nanostructure. Because of the simultaneous polymerization–precipitation process open three-dimensional (3D) porous and hollow structures were formed consisting of nanosheets as the petals with an average thickness of about 20 nm.[86–88] Besides, mesoporous ceria attracts a lot of attention as a versatile catalyst and support specimen because of its high surface area and porosity, because of which it can increase the dispersion of active secondary components. Adding more to it, Ji *et al.* reported an ordered mesoporous (OM) CeO_2 by using cubic *Ia3d* mesoporous MCM-48 silica where the obtained OM structure CeO_2 achieved very high efficiency towards photocatalytic dye degradation.[89] Further, hollow core–shell 3D structures are also investigated due to their peculiar advantageous properties. In this direction, Fang *et al.* communicated a variety of hollow 3D structures of CeO_2 like cubic, polyhedral and spherical through the template-engaged (Cu_2O) coordinating etching technique.[90] However, template-free synthesis is more convenient and easy nowadays. Qi and team prepared multi-shelled CeO_2 hollow microspheres (Fig. 5(e)) by a simple hydrothermal method followed by calcination without using any hard or soft template. Firstly, the reaction precursor glucose was subjected to a condensation and polymerization process under hydrothermal conditions resulting in carbon microspheres. Subsequently, Ce^{3+} ions got attached to the deprotonated functional groups inside the carbon microspheres in an alkaline environment. Finally, the as-formed carbon microspheres were used as sacrificial templates to obtain triple-shelled CeO_2 hollow microspheres *via* calcination in air as shown in Fig. 5(f).[91]

3.5 Nanostructured CeO_2 based materials

Considering the popularity of nanostructured CeO_2 in different photocatalytic applications, a wide variety of facet based CeO_2 heterojunctional systems such as CeO_2–metal oxide, CeO_2–metal sulphide/selenide, CeO_2–metal phosphide, CeO_2–carbonaceous materials, CeO_2–metals,[111–133] *etc.* have been synthesized and utilized in different energy and environmental applications thoroughly. More importantly, manipulation of the morphology of non-CeO_2 based components is very essential regarding the design of efficient interfaced nanostructured CeO_2 based composite photocatalysts. This is because the dimensionality of the other units and interfacial contact between them mainly determine the activity of the composites.[134] On the basis of dimensionality and size, CeO_2 based composite materials are classified into 0D–2D, 0D–1D, 1D–2D, 2D–2D, 0D–3D, *etc.* as schematically represented in Fig. 6(a). Their synthetic procedure follows either *in situ* growth methods or *ex situ* assembly approaches or the one-pot method. But most often two or more methods are combined in these multistep reaction procedures to prepare different nanostructured CeO_2 based materials. For example, small-sized 2D nanosheets can grow vertically or wrap on the surface of relatively large 1D CeO_2NRs. Du *et al.* reported small MnO_2 nanosheets decorated over CeO_2 nanowires *via* an *in situ* growth method. They reported a two-step hydrothermal method in which first CeO_2 nanowires were synthesized from $Ce(OH)_3$ nuclei, and then these nanowires were dispersed in $KMnO_4$ solution to obtain the 2D–1D heterostructure.[111] In another method reported by Jiang *et al.*, CeO_2 nanorods were derived from the Ce-MOF precursor. As shown in Fig. 6(b and c), $ZnIn_2S_4$ nanosheets were beautifully anchored on top of CeO_2 nanorods. They carried out the beautiful 2D–1D heterostructure synthesis *via* a low-temperature solvothermal procedure. As shown in the HRTEM image, a beautiful interface is formed between the 111 plane of CeO_2 and the 102 plane of $ZnIn_2S_4$ forming a facet merged interface.[112] Additionally, CeO_2 nanosheets decorated over Au nanorods were reported by Jia *et al.*, where simple site-selective growth of crystalline CeO_2 nanosheets on the end of AuNRs was observed resulting in the formation of a 2D–1D heterostructure. The AuNR capped CeO_2 heterostructure was prepared as follows: at first the AuNRs were prepared by using CTAB as a surfactant. Then the nanorods were re-dispersed again in CTAB solution and K_2PtCl_4 was subsequently added to the above solution followed by the addition of a cerium precursor at moderate temperature. The design of the site-selective heterostructure was based on the following points: (i) the AuNRs have a different crystal structure and curvature difference (at the side and the end), so the less dense molecular chains of CTAB at the ends offer less steric hindrance for the other species to reach the AuNR than those of the sides, and hence $PtCl_4^{2-}$ ions preferentially adsorb at the two ends of AuNRs as shown in Fig. 6(d), (ii) further the ceria precursor is rapidly hydrolyzed into $Ce(OH)_3$ at elevated temperature and is easily oxidized by the pre-adsorbed $PtCl_4^{2-}$ to produce the nuclei for the further growth of CeO_2. The preferential adsorption of $PtCl_4^{2-}$ and the autoredox

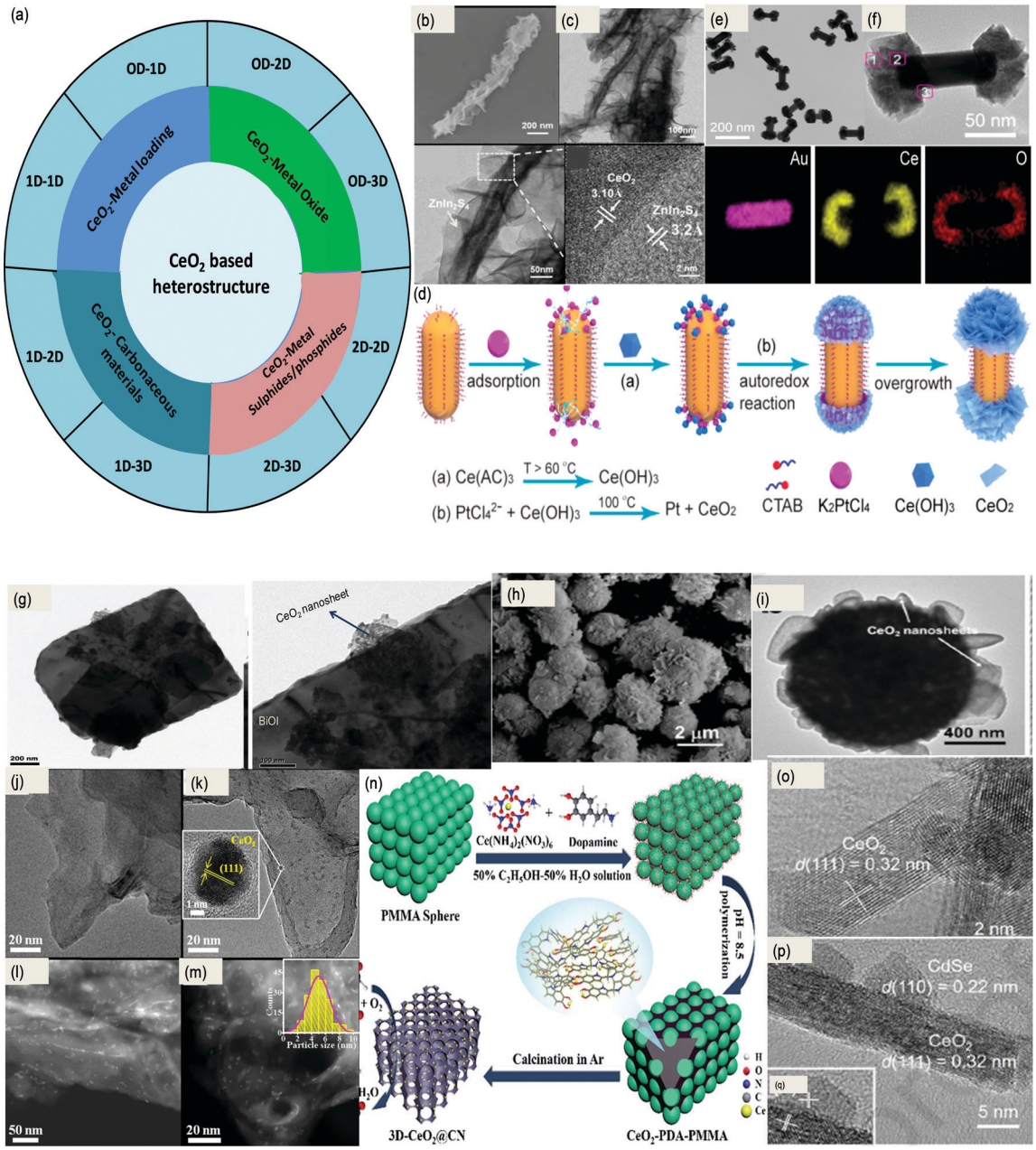

Fig. 6 (a) Schematic representation of different types of CeO_2 based heterostructure. (b) and (c) FESEM and TEM (HRTEM) images of the CeO_2–$ZnIn_2S_4$ heterostructure showing the 2D–1D interface between 111 (CeO_2) and 102 ($ZnIn_2S_4$) planes. Reprinted from ref. 112 with permission from Elsevier. (d) Schematic illustration of the synthesis process of a Au/end-CeO_2 nanostructure. (e and f) TEM, HAADF-STEM and the corresponding elemental map images of the Au/end-CeO_2 nanostructures. Reprinted with permission from ref. 113. (g) TEM images showing the face-to face BiOI and CeO_2 2D–2D heterostructure. Reprinted with permission from ref. 117, copyright 2019, 2018 American Chemical Society. (h and i) SEM and TEM images of the 3D–2D heterostructure consisting of Bi_2O_3 and CeO_2. Reprinted from ref. 119 with permission from Elsevier. (j and k) TEM and HRTEM images showing the uniform distribution of CeO_2 QDs over g-C_3N_4 and (l and m) corresponding HAADF images and particle size distribution. Reprinted from ref. 123 with permission from Wiley. (n) Schematic representation of the synthesis procedure of 0D–3D CeO_2@CN.[128] Reproduced by permission of The Royal Society of Chemistry. (o–q) TEM and HRTEM images showing the CdSe QD decorated CeO_2 NRs with lattice fringes and a clear interface. Reprinted from ref. 131 with permission from Elsevier.

reaction between $PtCl_4^{2-}$ and $Ce(OH)_3$ result in site-selective nucleation and growth of CeO_2 nanosheets at the end of the Au nanorod heteronanostructure as shown in the TEM images in Fig. 6(e and f).[113] Further, Feng and co-workers prepared a FeOOH/CeO_2 heterolayered nanotube (1D–1D) over Ni foam through the electrodeposition technique by using ZnO as a hard template. First, they deposited the CeO_2 layer over the ZnO NRs placed vertically over the nickel foam substrate, and then they deposited the FeOOH layer over the top of CeO_2 followed by removal of the ZnO template to yield a core–shell type 1D–1D heterostructure.[114]

Compared to other heterostructures, 2D–2D materials possess maximum hetero-interfaces and strong physical and electronic

coupling effects, which further facilitate the anti-recombination process and thus contribute to high photocatalytic performance. For example Wen *et al.* reported a face to face heterostructure, where they first prepared CeO_2 microplates *via* a sol–gel auto-combustion method and then BiOBr nanosheets were loaded onto the surface of CeO_2 with the assistance of ethylene glycol by a facile deposition–precipitation technique.[116] Further, Parida and co-workers prepared a series of 2D/2D-BiOI/CeO_2 nanocomposites through a simple precipitation technique followed by *ex situ* coupling. Initially, they prepared a CeO_2 nanosheet coupled with a dodecyl sulphide ion layer and then sonicated it in formamide solution. In this process the CeO_2 nanosheet got free and rectangular BiOI microplates were introduced onto this resulting in a beautiful face to face 2D–2D heterostructure as shown in Fig. 6(g).[117] Moreover, Zhang *et al.* delineated a one-pot synthetic strategy to produce vertical 2D–2D Co_3O_4–CeO_2 nanosheets over Ti mesh *via* the hydrothermal method; then the samples were further selectively calcined in the presence of sodium hypophosphite to produce an efficient CoP–CeO_2/Ti hybrid.[118] Furthermore, Yang *et al.* prepared a 3D–2D core–shell type Bi_2O_3@CeO_2 heterostructure through a simple two-step hydrothermal process followed by high-temperature calcination. They observed that the high-temperature treatment facilitates the outward diffusion of the interior Bi_2O_3 leading to the formation of a more prominent 3D–2D heterojunction effective for photocatalysis. As shown in Fig. 6(h and i) 2D CeO_2 nanosheets are very beautifully attached to the Bi_2O_3 sphere leading to an efficient heterostructure.[119] Gong *et al.* prepared a CeO_2@MoS_2 (3D–2D) hybrid heterostructure *via* a facile two-step wet chemistry strategy. At first, they prepared CeO_2 hollow spheres by a template-assisted method and then few-layered ultrathin MoS_2 nanosheets were deposited on the hollow CeO_2 spheres through a hydrothermal process.[120]

Furthermore, CeO_2 QDs are in the limelight because of their outstanding size-derived properties and visible light absorbing nature; however, the associated drawbacks like self-aggregation and high charge carrier recombination restrict their photoactivity. So CeO_2 QDs are often combined with 1D nanorods,[121,122] 2D nanosheets[123–126] and also with 3D[127–129] structured materials to improve their catalytic activity. Li *et al.* prepared a 0D–1D heterostructure where CeO_2 QDs were decorated over sulphur doped carbon nitride nanotubes through an *in situ* deposition–precipitation technique without using any surfactant or template. They found that the CeO_2 QDs are distributed inside as well as outside of S–CN nanotubes.[121] Likewise, Xia and the group proposed a strategy for the preparation of CeO_2 QDs on a template. They prepared quantum sized nanoceria on to the surface of polymeric carbon nitride nanosheets (PCN) without using for growth inhibitor essential for QDs preparation. The synthetic strategy they reported is as follows: the cerium precursor was mixed with the suspension of PCN; here Ce ions adsorbed on the surface of PCN because a strong coulomb interaction existed between the positively charged Ce ion and the lone pair electron of nitrogen atoms. Upon further heating, the adsorbed Ce ions hydrolyzed with water in the presence of DMF and further calcination yielded QDs of CeO_2 uniformly decorated over PCN as shown in Fig. 6(j and k). It was observed from HAADF-TEM images as shown in Fig. 6(l and m) that 5 nm sized CeO_2 QDs are uniformly anchored over PCN nanosheets producing a 0D–2D heterojunction.[123] Again, Zhang *et al.* reported a 0D–2D heterostructure between 10 nm CeO_2 nanoparticles and $ZnIn_2S_4$ nanosheets. At first, through a simple solvothermal method, the $ZnIn_2S_4$ nanosheet was prepared and the Ce^{3+} precursor was added into the alcohol–water mixed solution containing $ZnIn_2S_4$ to obtain the heterostructure. They termed the 0D CeO_2 nanoparticle on the 2D $ZnIn_2S_4$ nanosheets as a ''chess piece'' on the ''checkerboard'' type morphology of CeO_2.[124] Further, Luo *et al.* reported an interesting synthesis procedure for the *in situ* generation of CeO_2 QDs within the pores of 3D-nitrogen doped porous carbon. In the first step, self-assembled PMMA colloidal spheres were prepared and the voids were filled with ceric ammonium nitrate and dopamine solution. At pH 8.5, dopamine underwent self-polymerization and got adhered to the PMMA scaffold and in the meantime the cerium precursor was chelated by the same as shown in Fig. 6(n). Further, upon calcination the hard template (PMMA) was removed to generate the 0D–3D heterostructure.[128]

Besides these, 0D QD decorated CeO_2 nanostructures have gained a huge positive response; for example, quantum sized particles are decorated over nanorods, nanosheets, and nanoflowers of CeO_2 giving rise to various heterointerfaces with noticeable performance.[130–133] In this direction, Ma *et al.* reported a 0D–1D heterostructure containing CdS QDs over CeO_2 NRs through a solvothermal technique.[130] In addition to this work, the team also studied a 0D–1D CdSe QDs–CeO_2 nanorod heterostructure as shown in Fig. 6(o) through a wet chemistry method (details discussed below). They first dispersed CeO_2 nanorods and then added a Cd salt precursor and a capping agent, *i.e.* L-cysteine, followed by dropwise addition of a Se precursor to obtain the heterostructure. From the TEM micrographs (Fig. 6(p and q)) a clear interface between 0D CdSe QDs(110) with 1D CeO_2(111) nanorods is seen.[131] Further Ma *et al.* also reported another heterostructure, *i.e.* CdS QD decorated Fe–CeO_2 based nanoflowers (3D), through a simple solvothermal method in the presence of dodecanethiol and oleylamine.[133]

In the past decade, nanostructured CeO_2 and CeO_2 based materials have received increasing attention as photocatalysts for pollutant degradation and solar fuel generation because of the unique properties such as biocompatibility, chemical inertness, strong oxidizing capability, higher charge separation and transportation efficiency and most importantly absorption of more photonic energy. So in the following section, we have summarized different photocatalytic applications of CeO_2 and CeO_2 based materials, with a thorough description of the theoretical concept along with some examples.

4. Photocatalytic water reduction and oxidation

Water splitting is a process of breaking water into its elemental constituents such as di-hydrogen and oxygen. It is a very promising approach but the process is a multielectron, endothermic uphill

reaction that requires a high positive Gibb's free energy. Thus specific energy such as solar light is required to cleave a high energy HOH bond. Generally, 2.458 eV energy is required to split one water molecule to generate one hydrogen molecule, which works under 1.23 V potential difference for the displacement of two electrons. So a photocatalyst that has the ability to decrease the overpotential required to carry out the reaction is the need of the hour.[135–140]

4.1 Hydrogen evolution

The hydrogen evolution reaction is a major half-reaction of water splitting which generates sustainable clean H_2 energy. To replace fossil fuels, different fuels have been investigated recently, among which hydrogen has emerged as an appealing clean and green energy resource for future generation energy systems. It has a high energy density as compared to other hydrocarbon fuels and doesn't release any harmful toxic gases into the environment after its use. Thus, it can minimize pollution as well as reduce greenhouse gas emissions. Currently, most of the H_2 is prepared from either the hydrocarbon steam reforming process or the coal gasification process, which are high energy-consuming processes and require very high temperature processing. So its generation by utilising solar energy through water splitting is the most suitable and promising approach.[135–157] In this regard CeO_2 and CeO_2 based materials are explored both theoretically and practically towards the photocatalytic H_2 evolution reaction as summarized in Table 1.

Water splitting over ceria includes 2 major steps: the first is water hydroxylation and the second is H_2 formation. First water molecularly adsorbs by the oxygen atom on the top of the Ce atom of $CeO_2(111)$, while water adsorbs dissociatively near the oxygen vacancy of defect enriched $CeO_2(111)$ and in both cases one H of water bonds with the surface oxygen atom. Then water dissociation into hydroxyl takes place and the surface vacancies facilitate the water dissociation step. And finally hydroxyl decomposition occurs and liberates H_2 through an asymmetric process, which involves oxidation of Ce^{3+} to Ce^{4+}.[158–160] Further, in the case of excessive hydroxylated CeO_2, water hydroxylation and liberation of H_2 might involve a new intermediate, *i.e.* Ce–H. It is found that the OH species plays a very important role in water splitting and its formation and H_2 liberation mainly depend upon the surface vacancy.[160] Further Mullins *et al.* did theoretical calculations over both planes of reduced $CeO_2(100)$ and $CeO_2(111)$. They found that dissociation is much more favorable on $CeO_2(100)$ than on $CeO_2(111)$; however, in the reduced state H_2 generation occurs much more on $CeO_2(111)$

Table 1 Complete results of the H_2 evolution performance of CeO_2 and CeO_2 based heterostructures

Materials	Light source	Experimental conditions	Activity	Ref.
Defective CeO_2 NRs	300 W Xe lamp	Na_2S–Na_2SO_3 sacrificial agent	5.020 μmol h^{-1} g^{-1}	71
Single crystalline hexagonal CeO_2 NRs(110)	300 W Xe lamp	Na_2S–Na_2SO_3 sacrificial agent	741 μmol h^{-1} g^{-1}	76
Au@CeO_2	50 W Xe lamp	Methanol sacrificial agent, Pt co-catalyst	8.7 μmol h^{-1} mg^{-1}	162
Au@CeO_2	300 W Xe lamp ($\lambda > 420$ nm)	Methanol sacrificial agent	4.05 μmol mg^{-1} h^{-1}	163
CdS QDs/CeO_2NRs	300 W Xe lamp ($\lambda > 300$ nm)	Na_2S–Na_2SO_3 sacrificial agent	101.12 μmol h^{-1} g^{-1}	130
CdSe QDs/CeO_2NRs 111 facet	300 W Xe lamp ($\lambda > 300$ nm)	Na_2S–Na_2SO_3 sacrificial agent	283.32 μmol h^{-1} g^{-1}	131
CdS/CeO_2	300 W Xe lamp ($\lambda > 420$ nm)	Lactic acid	8.4 mmol h^{-1} g^{-1}	165
$Mn_{0.2}Cd_{0.8}S$ QDs/2D CeO_2	Xenon lamp with a power of 5 W, $\lambda > 400$ nm	Na_2S–Na_2SO_3 sacrificial agent	8.73 mmol g^{-1} h^{-1}	166
MoS_2(2 wt%)–CeO_2	150 W Xe lamp	Methanol sacrificial agent	2.542 mmol h^{-1} g^{-1}	167
1D/2D-CeO_2/$ZnIn_2S_4$	300 W Xe lamp AM 1.5G filter	50 μL of BA was dispersed in 5 mL of acetonitrile	1496.6 μmol g_{cat}^{-1} h^{-1}	112
0D/2D CeO_2/$ZnIn_2S_4$	300 W Xe lamp ($\lambda > 420$ nm)	Na_2S–Na_2SO_3 sacrificial agent	847.42 μmol h^{-1} g^{-1}	124
SnS_2–Ce_2S_3–CeO_2	300 W Xe lamp AM 1.5G filter	TEOA	240 μmol g^{-1} h^{-1}	168
CeO_2/ZnS–CuS	300 W Xe lamp	Methanol sacrificial agent	13.47 mmol g^{-1} h^{-1}	169
CeO_2 QDs/carbon	300 W Xe lamp	Methanol sacrificial agent	582 μmol g^{-1} h^{-1}	129
CeO_2@N,S-C	300 W Xe lamp	TEOA	555 μmol h^{-1} g^{-1}	170
CeO_2/g-C_3N_4	300 W Xe lamp ($\lambda > 420$ nm)	TEOA, 1.5 wt% Pt	0.83 mmol h^{-1} g^{-1}	171
c-CeO_2(100) and g-C_3N_4	300 W Xe lamp ($\lambda > 420$ nm)	TEOA, 3 wt% Pt	860 μmol h^{-1} g^{-1}	173
rCN{110} > cCN{100} > oCN{111}	300 W Xe lamp ($\lambda > 420$ nm)	TEOA, 3 wt% Pt	rCN – 1100 μmol h^{-1} g^{-1}	174
CeO_2 QD-S-doped g-C_3N_4 NR	300 W Xe lamp ($\lambda > 420$ nm)	TEOA, 1 wt% Pt	2923.8 μmol h^{-1} g^{-1}	121
CeO_2/ZnONTs FTO	300 W Xe lamp	Na_2S–Na_2SO_3 sacrificial agent	2.7 μmol cm^{-2} h^{-1}	175
CeO_2–ZrO_2	300 W Xe lamp	Na_2S–Na_2SO_3 sacrificial agent	≈4 μmol g^{-1} h^{-1}	176
$W_{18}O_{49}$/CeO_2	300 W Xe lamp ($\lambda > 400$ nm)	TEOA	0.2061 mmol g^{-1} h^{-1}	177
MOF-derived NiO/CeO_2	300 W Xe lamp	Methanol sacrificial agent	29.6 μmol h^{-1} g^{-1}	178
CeO_2/$CeVO_4$/V_2O_5	300 W Xe lamp	MB aqueous solution (50 mg L^{-1})	47.42 μmol g^{-1} h^{-1}	179
CeO_2–MoS_2/g-C_3N_4 as 0D/2D	UV light emitting diodes (UV-LEDs) ($\lambda > 420$ nm)	Na_2S–Na_2SO_3 sacrificial agent	1308 μmol g^{-1} h^{-1}	139
(110) CeO_2-IT/2HMoS_2	UV-light emitting diodes	Na_2S–Na_2SO_3 sacrificial agent	73.1 μmol h^{-1}	180
CeO_2–CuO QDs/graphene	300 W Xe lamp	Methanol sacrificial agent	2481 μmol g^{-1} h^{-1}	181
3DOM Ag/CeO_2–ZrO_2	300 W Xe lamp	Na_2S–Na_2SO_3 sacrificial agent	6.62 μmol h^{-1}	182
Ag–ZnO–CeO_2 Rod–rod	300 W Xe lamp AM 1.5G filter	Glycerol	18 345 μmol g^{-1} h^{-1}	183
MoS_2/CeO_2–Co_3O_4	5 W LED lamp ($\lambda > 420$ nm)	TEOA	221 μmol in 3 h	184
Ni–P/CeO_2–TiO_2	Solar stimulator (1 sun)	—	1300 μmol/5 h	185

than on the former due to the different adsorption sites. On reduced CeO_{2-x}(111) the dissociated water easily reoxidizes the ceria substrate, liberating H_2.[161] In accordance with the above prediction different CeO_2 based materials were explored in the water splitting reaction as follows. Lu *et al.* synthesized single crystalline hexagonal CeO_2 NRs, directly grown on Ti substrates with highly exposed (110) planes, which showed significant photocatalytic activity for hydrogen evolution (741 μmol g^{-1}) in Na_2S–Na_2SO_3 solution. They also tested the hydrogen evolution activity in methanol as a scavenger, where CeO_2 NRs exhibited a higher activity than commercial CeO_2, CdS as well as P25 due to the presence of exposed 110 active planes; however the yield rate was one fourth of that obtained with the sodium sulphide/sulphite scavenger because of the special redox capacity of the latter. Moreover, they observed a red shift in the absorption edge of CeO_2 NRs due to the presence of Ce^{3+} defects, hence harvesting more visible light which may be another cause of enhanced activity, and in addition the presence of Ce^{3+} acted as an intermediate medium which accelerated the hole consumption of the sacrificial agent, hence enhancing the availability of reducing electrons for the water reduction reaction.[76] Further, Dong *et al.* reported another defective CeO_2 NR towards photocatalytic hydrogen evolution. They prepared high surface area (65.26 m^2 g^{-1}) CeO_2 NRs by a simple hydrothermal method with a higher percentage of Ce^{3+} (22.53%) and oxygen vacancies (0.74).[71] The as-prepared nanorods displayed hydrogen production at a rate of 5.020 mmol g^{-1} h^{-1} under solar light irradiation, and the enhanced activity was attributed to the favourable band structure, which enabled the effective photonic energy absorption along with the redox shuttle of Ce^{3+} to Ce^{4+}, which retarded the charge recombination.

However nanostructured CeO_2 alone doesn't give appreciable results as compared to others, because of its high recombination rate of photogenerated excitons and the low ability for solar light absorption. Hence, CeO_2 is often combined with noble metals[162,163] or other photocatalysts/co-catalysts.[164–169] Dao *et al.* developed a novel route for the synthesis of the Au@CeO_2 core–shell functionalized with Pt. The Au@CeO_2 nanostructure photocatalyst was further tested for the H_2 evolution reaction under visible light and it exhibited H_2 production efficiency at a rate of 8.7 μmol h^{-1} mg^{-1}. The enhanced activity was attributed to the SPR effect of Au, which was helpful for visible light absorption and the corresponding charge carrier generation. Further, the photogenerated hot electrons travel *via* direct injection and cross tunnelling into the conduction band of CeO_2, where they travel to the Pt co-catalyst and reduce the adsorbed H^+.[162] Further, a number of modified nanostructured CeO_2 materials in combination with other low bandgap materials such as metal sulphides[112,124,130,131,164–169] have been reported compared to neat CeO_2. You *et al.* synthesized a type II heterojunction composite between CdS NPs and CeO_2 NRs and tested its photocatalytic activity towards the hydrogen evolution reaction. Under visible-light irradiation ($\lambda > 420$ nm) the as-prepared 1 : 1 ratio CdS/CeO_2 achieved an optimum H_2 evolution rate of 8.4 mmol h^{-1} g^{-1}, with a high apparent quantum yield (AQY) around 11.2%. The enhanced activity can be attributed to the promoted lifetime and separation efficiency at the heterojunction interface.[165] Recently, Ma *et al.* reported the H_2 evolution activity of CdS QD decorated CeO_2 NRs and observed an optimum rate of H_2 production, *i.e.* 101.12 μmol h^{-1} g^{-1} (3 atm% CdS) which was 45 times higher than that of neat CeO_2 NRs under light irradiation (300 W Xe lamp $\lambda > 300$ nm) as shown in Fig. 7(a). The enhanced photoactivity for a prolonged period of 60 h was mainly attributed to higher light absorption ability, enhanced charge transfer and separation efficiency and greater lifetime of photogenerated charge carriers due to the presence of the CdS component. The efficient charge transfer mechanism was found to be of the Z-scheme type instead of the heterojunction type charge transfer mechanism as shown in Fig. 7(b) where higher reducible electrons resided at the conduction band of CdS while higher oxidizable holes were quenched by the sulphide/sulphite scavenger over the CeO_2 surface. They represented solid evidence of the Z-scheme, where the catalyst responds to both hydroxyl and superoxide radicals in the spin trapping ESR experiment as shown in Fig. 7(c and d) despite the incapability of neat CdS for hydroxyl radical generation, thereby proving that the photogenerated charge separation occurred through the Z-scheme rather than the conventional double charge transfer mechanism.[130] Moreover, in addition to CdS, Ma *et al.* reported CdSe QD decorated CeO_2 NRs for photocatalytic hydrogen evolution and they found a rate of 283.32 μmol h^{-1} g^{-1}, which is higher than that of the neat component. Further through DFT analysis they found that the 111 exposed facet interwinged heterostructure increases the water adsorption ability and creates a lower energy barrier for water dissociation, while the same Z-scheme mechanism was followed by this heterostructure also.[131] Wang *et al.* reported another 0D–2D heterostructure where $Mn_{0.2}Cd_{0.8}S$ quantum dots were decorated over a 2D CeO_2 building block and gave rise to a perfect 0D(101)–2D(111) interface. They used different types of scavengers such as methanol, lactic acid and the sulphide + sulphite mixture and observed that the catalytic efficiency was continuously decreased in methanol and lactic acid solution, while the activity was retained in the sulphide+ sulphite solution. As the photocatalyst contains metal sulphide, upon light irradiation the metal sulphide corrodes down which retards its long term activity in the methanol scavenger solution. Hence, they observed that $Mn_{0.2}Cd_{0.8}S$–CeO_2 exhibited a maximum hydrogen production rate of 8.73 mmol g^{-1} h^{-1} in the sulphite/sulphide scavenger solution with an apparent quantum efficiency greater than 2 at 400 nm. The introduction of CeO_2 prolonged the lifetime of the photogenerated charge pair through the Z-scheme, and thereby increased the charge separation efficiency and lowered the charge transfer resistance.[166] Recently, 1D/2D and 0D/2D heterostructures between CeO_2 and $ZnIn_2S_4$ have gathered attention, as $ZnIn_2S_4$ can easily be tuned to two dimensional nanosheet materials.[112,124] Jiang *et al.* prepared $ZnIn_2S_4$ nanosheets which were grown *in situ* on the surfaces of CeO_2 nanorods. The 2D/1D composites exhibited a hydrogen production yield of 1496.6 μmol g_{cat}^{-1} h^{-1} in tandem with the selective oxidation of aromatic alcohol, due to the synergistic advantage of both CeO_2 and $ZnIn_2S_4$. The combined effect of both the moieties especially that of the excellent $ZnIn_2S_4$ nanosheets is

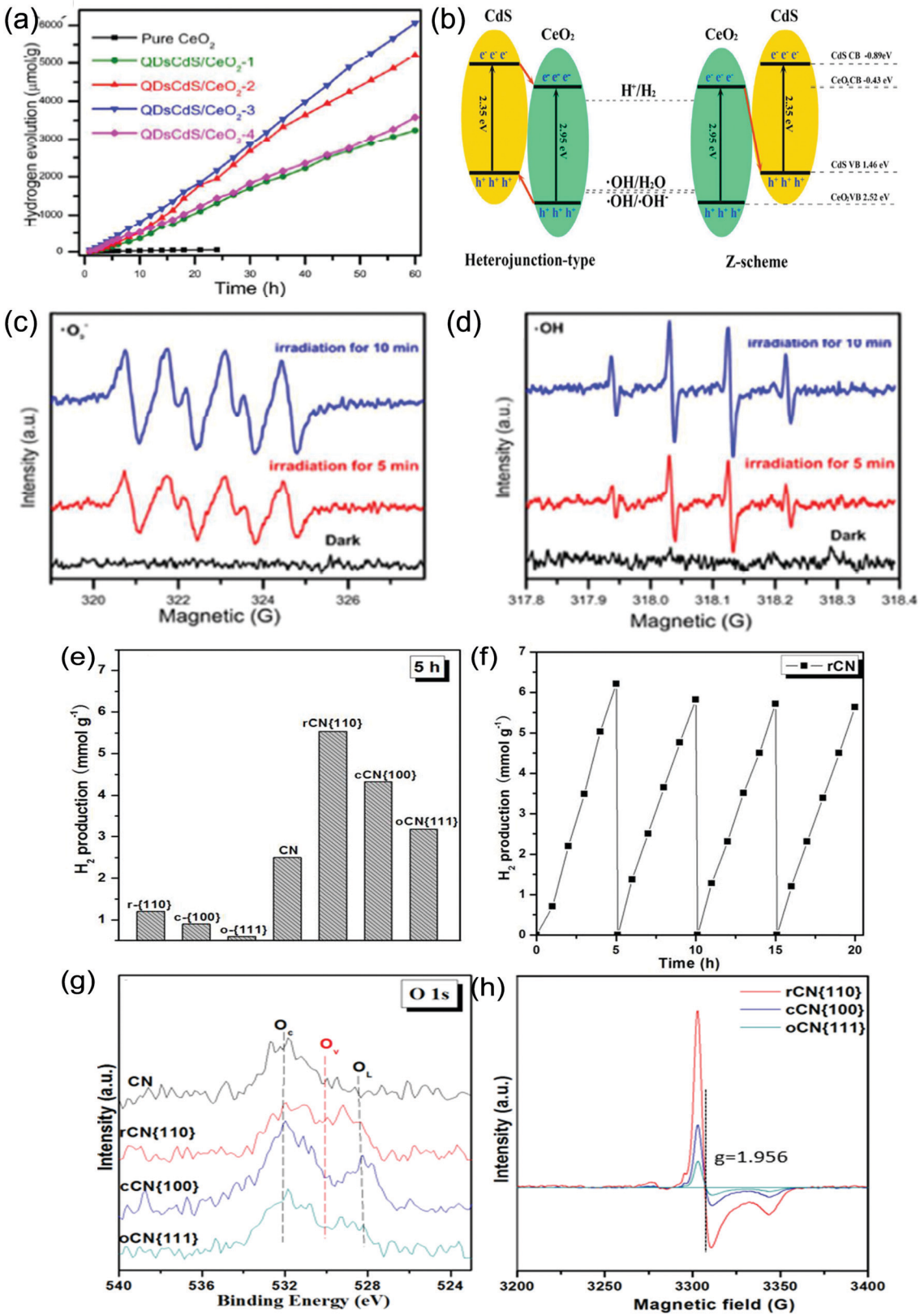

Fig. 7 (a) Photocatalytic hydrogen evolution over CeO_2 nanorods and CdS QD decorated CeO_2 in 60 h. (b) The possible photocatalytic mechanism exploration of the heterojunction-type and Z-scheme over the CdS QDs/CeO_2 nanorod 0D/1D heterostructures. (c and d) The DMPO spin-trapping ESR spectra of CdS QDs/CeO_2-3 composites. Reprinted with permission from ref. 130, copyright 2018 American Chemical Society. (e) H_2 production of CeO_2 nanorods, cubes, octahedra, CN, rCN, cCN, and oCN composites under visible light irradiation after 5 h. (f) Reusability test of the rCN composite. (g) O 1s XPS spectra of CN, rCN, cCN, and oCN. (h) ESR results of rCN, cCN, and oCN. Reprinted from ref. 174 with permission from Elsevier.

helpful for visible-light absorption and CeO_2 nanorod enabled one directional charge transport contributes to higher efficiency of the composite. Moreover, intimate interfacial contacts are formed in the solid Z-scheme heterostructures, which accelerate the charge transfer and separation while retaining the strong reducibility of electrons in the CB of $ZnIn_2S_4$ nanosheets and the oxidizability of holes in the VB of CeO_2 nanorods.[112] Moreover, *in situ*-MOF derived CeO_2 based materials have also come to light.[169,170] With respect to this, Wang *et al.* prepared a CeO_2–ZnO nanoheterostructure from a Ce-doped ZIF-8 MOF as the precursor. Further through an *in situ* vulcanization process the above heterostructure was converted to CeO_2–ZnS, which showed the best photocatalytic hydrogen production performance. However, further loading of the CuS co-catalyst *via* an *in situ* cation exchange method led to a hydrogen production rate of 13.47 mmol g^{-1} h^{-1} which was about 1.4 times that of CeO_2/ZnS.[169]

Nanostructured CeO_2 has also been modified with carbon-based materials such as carbon, graphene, and g-C_3N_4,[121,129,171–174] and it was found to show better photocatalytic activity than neat CeO_2. For example, recently Qian *et al.* reported a new biotemplate oriented synthetic strategy for the synthesis of zero dimensional CeO_2 QDs embedded in a porous carbon tube. The biotemplate carbonization process provided a layer matrix and a small amount of oxygen for QD deposition and growth. The obtained 3D porous CeO_2 QDs/carbon exhibited the highest H_2 evolution rate which was 5.5 times higher than that of the bulk CeO_2 due to the presence of defective CeO_2 along with its quantum dot property. Upon visible light irradiation, the photogenerated electrons and holes were produced at the CeO_2 surface, where the electrons drifted towards the carbon skeleton *via* the Ce–C bond, thereby accelerating charge pair separation as well as effective utilization of these energetic electrons towards the water reduction reaction.[129] Next, Zou *et al.* synthesized CeO_2 nanocubes decorated over g-C_3N_4 nanosheets and described the interaction through hydrogen bonds and a p–π hybrid between c-CeO_2(100) and g-C_3N_4. Further, the H_2 evolution activity was determined to be 4300 μmol g^{-1} for 5 h illumination, which was higher than that of pristine CeO_2, g-C_3N_4 and irregular CeO_2 nanoparticles/g-C_3N_4. The same group performed another extensive study and compared the hydrogen evolution activity of morphology dependent (cube, rod and octahedral) CeO_2 coupled g-C_3N_4. They found that the CeO_2 nanorod with an exposed 110 facet when combined with the g-C_3N_4 nanosheet gave a much higher hydrogen production value than the others because of the stronger built-in interface. In brief, they prepared morphology tunable CeO_2 with (110), (100), and (111) exposed planes and found that the crystal planes of CeO_2 greatly alter some of the characteristics in the CeO_2 and g-C_3N_4 heterostructure. They observed that 110 exposed CeO_2 nanorod modified g-C_3N_4 exhibited higher photocatalytic hydrogen production efficiency than other CeO_2 modified samples as shown in Fig. 7(e) and the order was found to be CeO_2 NR(110)/gC_3N_4 > CeO_2 Cube(100)/g-C_3N_4 > CeO_2 octahedron (111)/g-C_3N_4 > g-C_3N_4. And also the optimally prepared catalyst retained its photoactivity in more than one cycle for up to 20 h (Fig. 7(f)). Furthermore, as shown in Fig. 7(g and h), from the XPS and ESR analysis it was found that the 110 rod shaped CeO_2 possesses more oxygen vacancies and higher Ce^{3+} concentration. Hence, the surface oxygen vacancies played a major role in determining the photoactivity. Further from DFT analysis, it was found that nanorod decorated g-C_3N_4 showed significant charge transport and separation at the interface, as the charge was increased in the C and N of g-C_3N_4 while it was decreased in the Ce atom of CeO_2, which led to better charge separation under light illumination than in the other materials.[173,174]

Further, other metal oxide combined CeO_2 nanostructures have also been explored in the field of the photocatalytic hydrogen evolution reaction.[175–179] For example, Zeng *et al.* reported a CeO_2/ZnONTs FTO heterojunction through a two-step electrodeposition technique and tested its photocatalytic H_2 evolution activity which was found to be 2.7 μmol cm^{-2} h^{-1}. The higher photocatalytic activity was attributed to a larger surface area, more active sites and effective electron–hole separation at the interface between two metal oxides.[175] Recently Shen *et al.* prepared a novel heterojunction photocatalyst $W_{18}O_{49}$/CeO_2 *via* a hydrothermal strategy. Under visible light irradiation, the oxygen vacancy enriched heterostructure exhibited the highest hydrogen production efficiency of about 0.2061 mmol g^{-1} h^{-1} which was 1.93 times higher than that of pure CeO_2. According to the DFT calculations, the authors claimed that between CeO_2 and $W_{18}O_{49}$, the Z-scheme charge transfer mechanism occurred, which retarded the efficient charge recombination, and hence electrons accumulated over the CeO_2 surface and reacted with H^+ to yield H_2.[177] Apart from all of these, nanostructured CeO_2 is also combined with more than one photocatalyst or co-catalyst towards the productive hydrogen evolution reaction.[180–185]

4.2 Oxygen evolution

The oxygen evolution reaction is another half reaction of water splitting, where water is oxidized to generate oxygen gas in the presence of a catalyst. It is a core process of many energy storage and conversion systems, such as solar cells, fuel cells, metal–air batteries, *etc.*[186–197] And for the water electrolysis to produce sustainable H_2 energy, water oxidation is a preliminary reaction. It is a multi-electron and multi-proton reaction, and is therefore kinetically as well as energetically a difficult/sluggish process. This is because for the generation of one molecule of O_2, four protons and four electrons are required. In order to oxidize two water molecules simultaneously, the catalyst must be able to store four electrons–holes close together.[197] So a catalyst which can absorb water and simultaneously oxidize two water molecules is a promising one. Since CeO_2 has the ability to carry out water oxidation smoothly, a number of CeO_2 based materials have been explored in this field which are summarized below.

In general water oxidation over CeO_2 involves two major steps as confirmed from DFT studies. The first step is the sequential dehydrogenation of water, *i.e.* $H_2O \rightarrow OH + H \rightarrow O + 2H$. In particular, on CeO_2(110), H_2O is adsorbed on the top Ce site and the adsorbed H_2O dehydrogenates to OH and H. Then the formed OH group dissociates into O and H, as the H migrates to the neighbouring top O site. Further, the formation of O_2 requires an additional step, in which an additional H_2O further dehydrogenates to form the second OH and H. The second OH

then combines with the O from the first H_2O molecule to form OOH. The formed OOH species binds to the Ce site in the final state. Meanwhile, O_2 is generated by the dehydrogenation of OOH *via* O–H bond scission.[103] Zhang *et al.* studied the theoretical concept behind the water oxidation process involving normal and defective CeO_2(110) nanorods. According to DFT, they found that the presence of oxygen vacancies on CeO_2(110) effectively modulates the electronic structure which enhances the charge transfer required for water dehydrogenation and also narrows the band gap. In brief, as shown in Fig. 8(a) the energy profile of defective CeO_2 for water dehydrogenation to O is very similar to that of perfect CeO_2, but is easier. Moreover, the dissociation of OH is unfortunately very difficult in perfect CeO_2 as the formed O and H tend to combine with each other producing OH again. But in the case of defective CeO_2, OH dehydrogenation is much easier as the reverse reaction is very slow. Further, the presence of oxygen vacancies on CeO_2(110) significantly reduces the activation energy of the rate limiting step (O–O bond formation) of water oxidation, due to the decreased O binding strength. Moreover, the distance between O and the second OH is shortened in the defective CeO_2 compared to that of the perfect one, which indicates that lower activation energy is required for the formation of O_2 *via* the OOH pathway in the defective CeO_2 as shown in Fig. 8(b). They found that normally in CeO_2, the HOOH pathway is not favoured because of its high activation barrier, but the OOH pathway is favoured as described above. In addition to this, defective CeO_2(110) possesses a higher rate constant for the rate limiting step which is about 2–3 orders of magnitude higher compared to that of the perfect CeO_2(110). They also studied the photocatalytic oxygen generation under visible light of the above materials and found that the $NaBH_4$ reduced CeO_2, *i.e.* defective CeO_2 NRs, exhibited the highest photocatalytic activity with the highest oxygen evolution rate (137.7 μmol g^{-1} h^{-1}) than the pristine. For the first time, they reported how to control the defects by varying the $NaBH_4$ amount. They found that on adding a particular amount of $NaBH_4$, the vacancy concentration

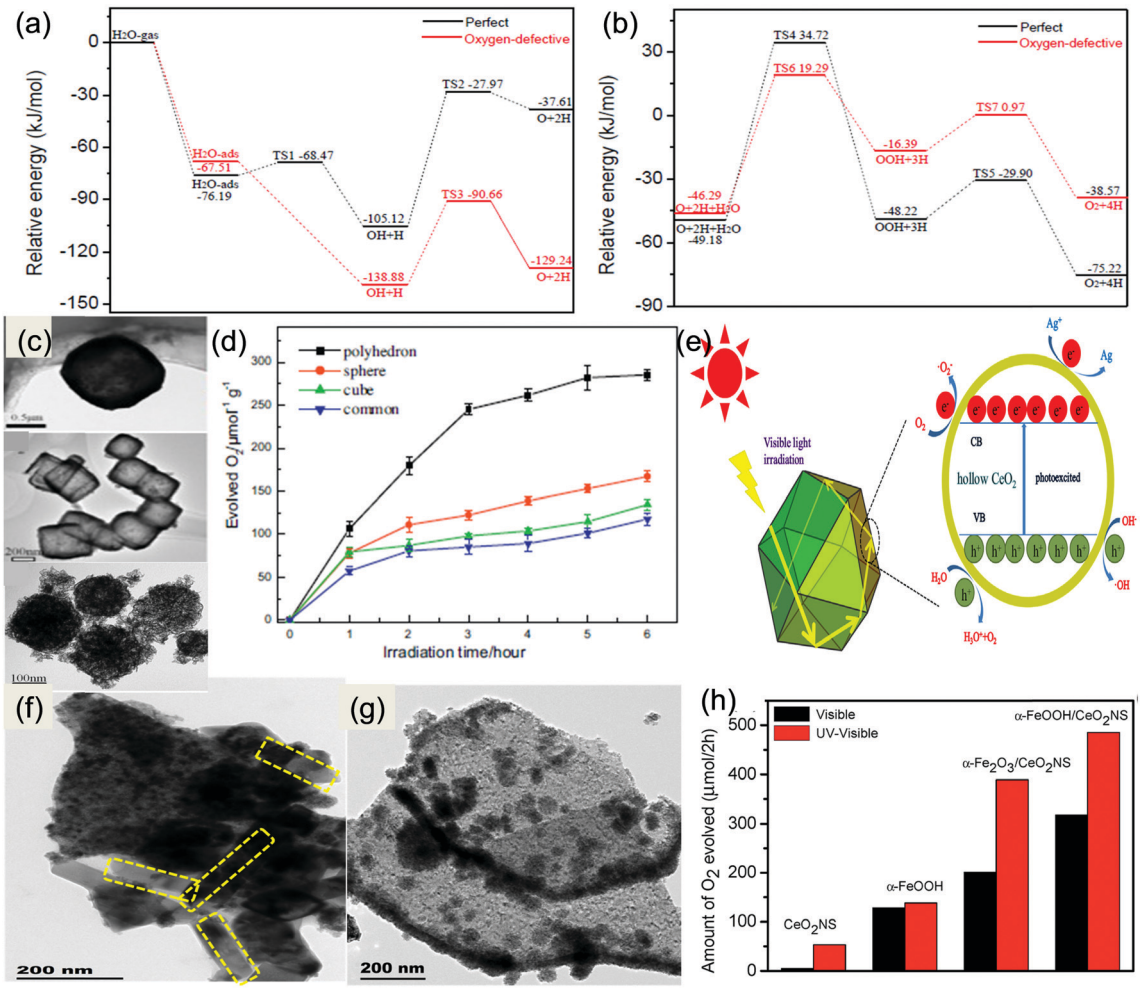

Fig. 8 Potential energy profiles for (a) water dehydrogenation to O and (b) O–O bond formation. Reprinted from ref. 103 with permission from Elsevier. (c) TEM micrographs of polyhedron, cube and sphere shaped CeO_2 (d) and their corresponding photocatalytic O_2 evolution curves under visible light irradiation. (e) The schematic illustration of the photocatalytic O_2 evolution mechanism over CeO_2 hollow structures under visible light irradiation. Reprinted from ref. 90 with permission from Elsevier. (f and g) TEM micrographs of FeOOH/CeO_2NS and Fe_2O_3/CeO_2NS. (h) Oxygen evolution bar graph showing Fe modified CeO_2.[200] Reproduced by permission of The Royal Society of Chemistry.

is optimized, and a further increase in the $NaBH_4$ amount decreases the vacancy density, which strongly affects the photocatalytic hydrogen evolution activity.[103]

Jiang *et al.* reported on the effect of crystal facets on the photocatalytic water oxidation reaction. They prepared CeO_2 of two different shapes, *i.e.* cube (100) and rod (110 + 100), *via* a simple hydrothermal method, where for the rod morphology two different types of precursors (nitrate and chloride) were used. Under 5 sun illumination, CeO_2 NRs prepared from the chloride precursor exhibited the highest oxygen evolution rate of 1.70 μmol h^{-1}, which might be due to the presence of surface bound hydroxyl group at the defect sites and two active planes, *i.e.* 100 and 110, which retarded the photogenerated charge recombination ability.[15] Further, Zhao *et al.* developed another nanostructured CeO_2, *i.e.* CeO_2 NRs, by hydrothermal synthesis followed by post-calcination under different atmosphere conditions. They found that Ar–H_2-800 possesses more active oxygen (24.16%) which is directly related to Ce^{3+}, and hence it emerged as a better water oxidation catalyst. They concluded that CeO_2 NRs prepared under mixed H_2 and Ar gas at 800 °C exhibit higher photocatalytic water oxidation ability at a yield rate of 707.73 μmol g^{-1}, which was 10 times higher than that of CeO_2 NRs calcined under air at 800 °C. The origin of the enhancement in the activity is mainly due to the increased content of surface oxygen vacancies and paramagnetic Ce^{3+} species under the reduced atmosphere which is helpful for reduction of the energy barrier for water adsorption and the corresponding photoxidation.[69] Next, Qi *et al.* synthesized a multi-shell hollow microsphere through a general self-templating method and tested its activity towards photocatalytic water oxidation in the presence of $AgNO_3$ solution (e^- scavenger). They found that the triple shelled CeO_2 hollow microsphere exhibited the highest O_2 evolution activity of 78 mmol g_{cat}^{-1} h^{-1} which was higher than that of the commercial CeO_2 NPs. This outstanding performance of the catalyst was attributed to the hollow structure which absorbs more incident light because of the multiple reflections by the multi-shell and possesses a larger surface area with more active sites for water oxidation.[91] Further Fang and co-workers synthesized different morphology oriented CeO_2 such as polyhedral, cubic and sphere-shaped nanocages through the template (Cu_2O) assisted method as shown in Fig. 8(c). A very interesting observation was made, *i.e.* polyhedral CeO_2 (47.5 μmol g^{-1} h^{-1}) nanocages possessed higher photocatalytic O_2 evolution activity than cubic nanocages (22.4 μmol g^{-1} h^{-1}) and sphere-shaped nanocages (27.8 μmol g^{-1} h^{-1}) as shown in Fig. 8(d).[90] As shown in Fig. 8(e), under light irradiation the CeO_2 hollow structure absorbs photons and excites electron–hole pairs; then the photogenerated holes react with water to give molecular oxygen while the generated electrons are quenched by $AgNO_3$. The activity improvement was ascribed to the polyhedral nanocage containing more active sites, a higher surface area and efficient photogenerated charge transport and separation. Additionally, the light absorption ability is enhanced in this particular nanostructure because of its inner shell which reflects the light properly. Primo *et al.* decorated gold particulate over quantum sized CeO_2 for activity improvement and efficient light absorption. It was found that 1 wt% gold loaded CeO_2 nanoparticles exhibited the highest oxygen evolution rate, *i.e.* 105 μmol h^{-1}, which was much more than that of the standard WO_3 photocatalyst (1.7 μmol h^{-1}). This remarkable photocatalytic activity was mainly due to the small size (5 nm) CeO_2, where they controlled the particle size of ceria (5 nm) by means of electrostatic binding of Ce 4p to alginate gel, subsequent supercritical CO_2 drying, and calcination.[198]

Other than nanostructured CeO_2, very limited work on modified CeO_2 based materials has come into existance.[199–201] For example, Fang *et al.* fabricated CoO_x decorated CeO_2 hollow nanocages for improved water oxidation. With an appropriate amount of CoO_x loading, the CeO_2 based hollow structure not only possessed a higher ability for light absorption but also showed a high O_2 evolution rate, *i.e.* 200 μmol g^{-1} h^{-1}, under visible-light irradiation with excellent durability.[199] Further, Parida and co-workers attempted to exploit new visible light self-healing 1D–2D FeOOH nanorods/CeO_2NS and 3D–2D Fe_2O_3/CeO_2NS hybrids in 2-dimensional nanosheet architecture photocatalysts as shown in Fig. 8(f and g) by a facile hydrothermal method and evaluated their photocatalytic performance towards the oxygen evolution reaction under UV-visible light. The optimised FeOOH/CeO_2NS and Fe_2O_3/CeO_2NS systems exhibit unprecedented photocatalytic activity towards O_2 evolution, *i.e.* 485 μmol/2 h and 389 μmol/2 h respectively (Fig. 8(h)). The enhanced performance of Fe/CeO_2 is attributed to the 2D structure of CeO_2 which provides the perfect site for growth of iron materials and extends the charge separation process throughout the nanohybrid. Additionally, the formation of a n–n junction across the heterointerface modifies the charge separation and transportation process. Further, the Ce^{3+}/Ce^{4+} redox cycle acts as an activator which healed photocorrode Fe^{2+} and regenerating the structural damage caused by irradiation.[200] Recently, Meng *et al.* synthesized a new type of molecular catalyst (MC) combined semiconductor heterostructure, *i.e.* a CoTCPP@CeO_2 nanotube heterostructure. The optimized CoTCPP@CeO_2 nanocomposite exhibited O_2 evolution at a rate of 30 μmol g^{-1} h^{-1} with long term durability and was found to be superior to other MC combined CeO_2, for example H_2TCPP@CeO_2 NTs, Co_3O_4@CeO_2 NTs and TCPP@Co_3O_4@CeO_2 NTs, under the same conditions. They proposed that initially, CoTCPP acts as a charge transporter to propel photoexcited electrons to CeO_2 by d–f electron coupling, which effectively suppresses the photogenerated charge recombination. In addition to this, the interfacial charge transfer results in *in situ* generation of surface oxygen vacancies and CoOOH species, which are found to be the major sites for enhancing water oxidation.[201]

5. CO_2 reduction reaction

The continuous rise in the atmospheric carbon dioxide level and depletion of fossil resources is a pressing concern that is directly threatening the balance of earth's ecosystems and sustainability of life for future generations. Among various on-going research activities for protection and remediation of the environment and solving the energy crisis, carbon dioxide

Table 2 Complete results of the CO_2 photoreduction performance of CeO_2 and CeO_2 based heterostructures

Catalyst	Light source	Reaction conditions	Activity	Ref.
$CeO_2(100)/CeO_2(110)$	300 W Xe lamp	Water, CO_2 gas Pt/MnO_x	CH_4 0.86 μmol h^{-1} g^{-1} 1.12 μmol h^{-1} g^{-1} (Pt, MnO_x co-catalyst)	84
Defective CeO_2 NRs	500 W Xe lamp	CO_2 gas phase reduction	CO 24–28 μmol g^{-1} in 6 h	104
CeO_2–SAC (defective) CeO_2–CSC	300 W Xe lamp	$NaHCO_3$	CH_3OH – 0.702 μmol h^{-1} g^{-1} 0.397 μmol $h^{-1}g^{-1}$	106
r-$CeO_2(110)$ c-$CeO_2(100)$	300 W Xe lamp	Water, CO_2 gas	CO 0.203 μmol h^{-1} g^{-1} CO 0.130 μmol h^{-1} g^{-1}	206
Ordered mesoporous CeO_2–TiO_2	300 W Xe arc lamp	Water, CO_2 gas	CH_4 – nearly 12 mmol g^{-1} in 325 min and CO – nearly 70 mmol g^{-1} in 325 min	207
3D ordered macroporous TiO_2–CeO_2	300 W Xe lamp ($\lambda > 420$ nm)	Water, CO_2 gas	CO – 2.06 μmol/400 min/100 mg	208
ZnO–CeO_2	300 W Xe lamp	Water, CO_2 gas	CO – 0.52 μmol h^{-1} g^{-1} and CH_4 – 0.06 μmol h^{-1} g^{-1}	209
Vacancy Cu_2O/CeO_2	300 W Xe lamp	Water, CO_2 gas	CO nearly 1.2 μmol g^{-1} in 8 h	210
CeO_2/Bi_2MoO_6	300 W Xe arc lamp ($\lambda > 420$ nm)	Water, CO_2 gas	CH_3OH – 32.5 μmol h^{-1} g^{-1} and C_2H_5OH – 25.9 μmol h^{-1} g^{-1} in 4 h	211
CdS@CeO_2 core/shell	300 W Xe lamp ($\lambda > 420$ nm)	Water, CO_2 gas	CH_3OH – nearly 1100 μmol g^{-1} in 8 h CH_4 – nearly 7 μmol g^{-1} in 8 h	212
$ZnIn_2S_4$ flower/CeO_2	300 W Xe lamp ($\lambda > 420$ nm)	$NaHCO_3$, H_2SO_4	CH_3OH 0.542 μmol h^{-1} g^{-1}	213
Defect rich g-C_3N_4@CeO_2	300 W Xe lamp ($\lambda > 420$ nm)	Water, CO_2 gas	CH_4 – 3.5 μmol g^{-1}, CH_3OH – 5.2 μmol g^{-1} and CO – 16.8 μmol g^{-1} in 3 h	214
m-CeO_2/g-C_3N_4	300 W Xe arc lamp	Water, CO_2 gas	CO – 0.590 μmol/50 mg/6 h and CH_4 – 0.694 μmol/50 mg/6 h	215
CeO_2–3D-gC_3N_4	UV light	NaOH, TEOA, CO_2 gas Pt-cocatalyst	CO 4.69 μmol h^{-1} g^{-1} and CH_4 3.03 μmol h^{-1} g^{-1}	216
CeO_2–N-doped graphene–Cu^{2+}	250 W Xe lamp	$NaHCO_3$, Na_2SO_3, CO_2 gas	CH_3OH 507.3 μmol h^{-1} g^{-1}	217
CeO_2MOF	300 W Xe lamp	Water, CO_2 gas	CO 1.68 μmol h^{-1} g^{-1}	218

capture and subsequent conversion into high liquid fuels including value-added chemicals is regarded as a potential strategy to slow down the alarming climate change and sustainably address the upcoming energy crises. Photocatalytic conversion of CO_2 to renewable fuel using solar energy has attracted more attention in the past 3 to 4 decades. Since then, various nanostructured metal oxide photocatalysts have been examined for the reduction of CO_2, and great achievements have been made. However, the rational design and synthesis of photocatalysts with high activity and selectivity towards the reduction of CO_2 is highly challenging.[202,203] CeO_2 has been widely used as the catalyst for CO_2 reduction, so both theoretical and experimental studies have eventually surfaced in this field, as summarized in Table 2.[204–217]

The theoretical concept of CO_2 adsorption, activation and subsequent reduction over the CeO_2 surface is as follows: at first, the CO_2 molecule is adsorbed in a horizontal configuration where the O atoms sit on top of the surface of Ce while the C atom sits on the four-fold hollow site of the top layer CeO_2. Then the adsorbed CO_2 is reduced to either a formate or carboxyl intermediate in the presence of adsorbed hydrogen, while in the absence of any adsorbed hydrogen, the CO_2 directly forms carboxylate species. Further, the formed intermediate (formate/carboxyl) undergoes dissociation to form CO species. However in defective CeO_2, CO_2 is directly dissociated into CO by donating its one oxygen to the oxygen vacancy. On CO_2 activation, the oxygen atom is directly incorporated into the vacant site *via* a redox mechanism and neutralizes the vacancy to generate the CO intermediate. Both the carboxyl and formate intermediates can produce CO while only the carboxyl intermediate will on further hydrogenation produce methanol on the ceria surface. The carboxylate pathway is more favourable for hydrogenation due to the presence of surface vacancies. Hence, the theoretical calculation gives full proof evidence for the effective CO_2 reduction in both oxidized and reduced CeO_2.[204,205] In this regard, there are a number of experimental reports on CO_2 photoreduction over CeO_2 based materials with eye-catching results. For example, Dong and coworkers analyzed the CO_2 reduction over (110) and (100) surfaces through both experimental and theoretical investigations and proposed a mechanism of CO_2 photoreduction over defective CeO_2 as shown in Fig. 9(a). They observed that the synergistic effect of both Lewis acid sites (oxygen vacancy) and Lewis base sites (hydroxyl group) was responsible for CO_2 activation and its subsequent reduction. Combining the results of CO_2-TPD, CO_2-adsorption, DRIFTS and DFT studies (Fig. 9(b and c), the authors concluded that the $CeO_2(100)$ plane possesses more hydroxyl species than the $CeO_2(110)$ plane, which are beneficial for the adsorption and subsequent activation of CO_2. Additionally, they illustrated the CO_2 reduction mechanism as follows (shown in Fig. 9(a)): the O atom of the surface hydroxyl group of CeO_2 donated electrons to the C atom of CO_2 and eventually, the O atom of the CO_2 reactant gave its p electrons to the oxygen vacancy of CeO_2, resulting in the formation of HCO_3^- species. Next, the carboxylate ($^{\bullet}CO_2^-$) radical ion intermediate was formed when the photoexcited electron transferred to the surface HCO_3^- species which was further confirmed by *in situ* ESR analysis. Finally, with the formation of OH, the CO gas was produced from the intermediate carboxylate species. Therefore, the synergistic interactions between the Lewis acidic and basic group are beneficial for CO_2 photoreduction.[95]

Additionally, Jiang *et al.* prepared defective CeO_2 nanorods for the photocatalytic gas-phase CO_2 reduction reaction and *via*

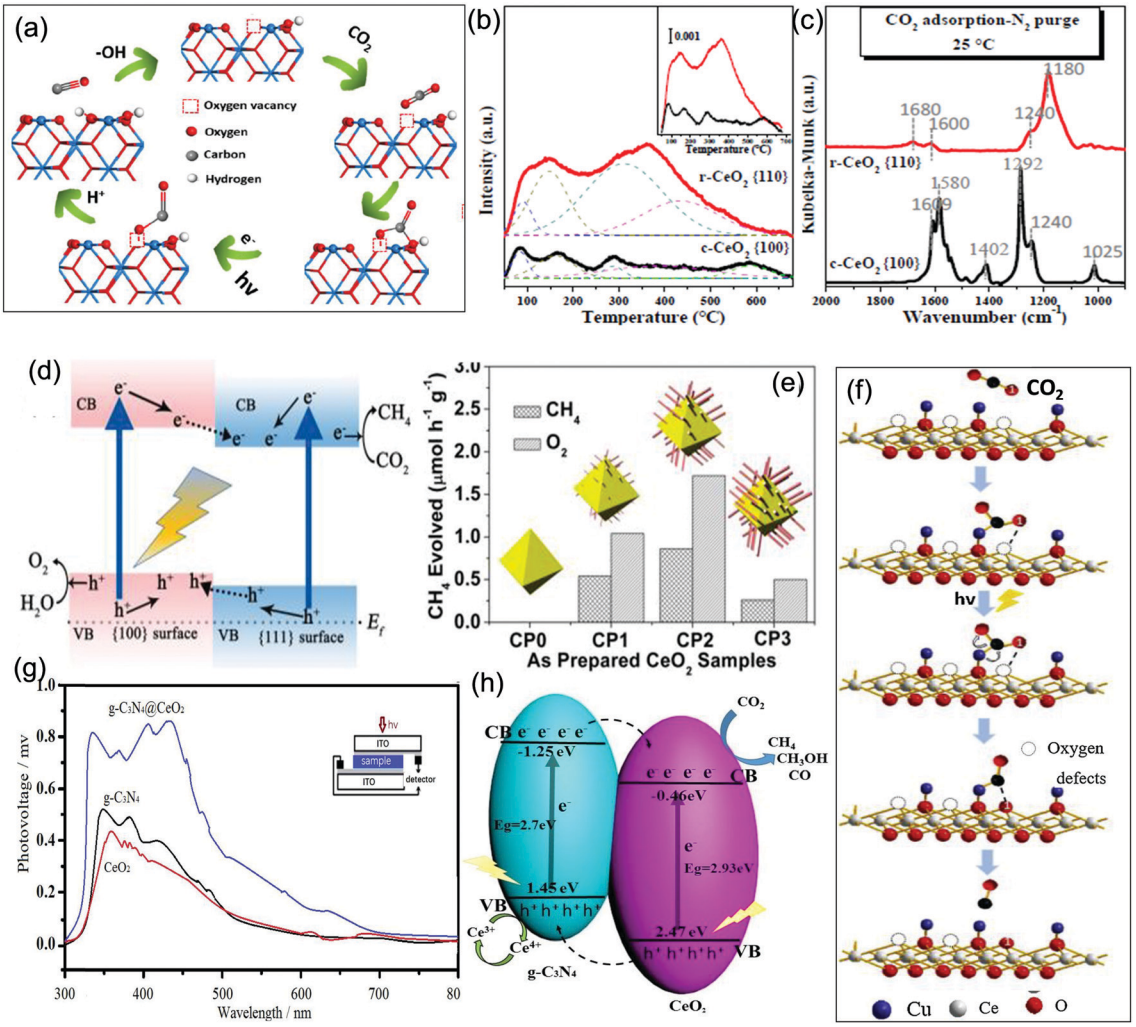

Fig. 9 (a) The possible CO_2 photoreduction mechanism on the oxygen-defective CeO_2(110) surface. (b) and (c) CO_2-TPD and CO_2 adsorption DRIFTS of the CeO_2(110) nanorod and the CeO_2(100) nanocube. (d) Schematic illustration of the photogenerated charge transfer mechanism between two exposed planes within prism anchored octahedral CeO_2. (e) CO_2 photoreduction efficiency showing the best prism anchored octahedron. Reprinted with permission from ref. 84 and 95, copyright 2020, 2015 American Chemical Society. (f) Proposed mechanism of CO_2 photoreduction on CuO decorated CeO_2. Reprinted from ref. 210 with permission from Elsevier. (g) Photocatalytic CO_2 reduction profile of CeO_2, g-C_3N_4 and a series of g-C_3N_4@CeO_2 heterostructures. (h) Plausible photogenerated charge pair separation and transfer and CO_2 photoreduction mechanism over the g-C_3N_4@CeO_2 heterostructure. Reprinted from ref. 214 with permission from Elsevier.

a systematic TEM and HRTEM study they confirmed the lattice distortion and dislocation type surface defects. Further, they found that the prepared CeO_2 can generate CO with nearly 100% selectivity with a yield of 24–28 μmol g_{cat}^{-1} after 6 hours of irradiation, which was like a milestone for neat CeO_2. However, after the prolonged irradiation (more than 20 h), the photoreduction activity was slowed down, as initially the local strain and oxygen vacancy help to activate adsorbed CO_2, but after a certain time, these vacancies were gradually consumed leaving behind massive electrophilic oxygen species over the CeO_2 surface which restricts the further photoreduction, thereby slowing down the formation yield of CO. They further found that the activity was recovered when the exhausted CeO_2 was again treated with $NaBH_4$ solution resulting in the subsequent defect formation.[104] Further, Li *et al.* reported the first kind of nano-structured CeO_2, *i.e.* hexahedron prism anchored octahedron, towards photocatalytic CO_2 reduction. According to the DOS study, there is a slight energy difference between the CB and VB of the (100) plane of the hexahedron prism and the (111) plane exposed octahedron which forms a homojunction between them. This homojunction is mainly responsible for the effective charge pair separation and transfer, where the electrons flow from the higher Fermi level of the hexahedron prism with exposed (100) facets to the (111) octahedron surface and catalyze the adsorbed CO_2 as shown in Fig. 9(d), while holes at the 100 surface react with water to generate oxygen. Hence, the hexahedron with a medium denser arm generated the most CH_4 by the reduction of CO_2 at the rate of 0.86 μmol h^{-1} g^{-1} while in presence of MnO_x co-catalyst the production rate was further increased to 1.12 μmol h^{-1} g^{-1} as depicted in Fig. 9(e).[84]

Recently Hezam *et al.* reported a novel preparation method, *i.e.* solar light assisted combustion synthesis, for the production of 12–18 nm diameter CeO_2 particles containing a high amount of surface defects. Under simulated solar light, the as-prepared O_v CeO_2 exhibited the highest photocatalytic reduction of CO_2 to CH_3OH at the rate of 0.702 μmol h^{-1} g^{-1} with a quantum efficiency of 0.23% at 350 nm, while the conventional solution combustion assisted CeO_2 displayed only a rate of 0.397 μmol h^{-1} g^{-1}. From DFT simulation it was found that the generated oxygen vacancy increases its light absorption by narrowing the band gap of CeO_2, and enhances its CO_2 capture ability. Moreover, the mean crystallite size, low crystallinity and mesoporous structure played a crucial role in the selectivity of CO_2 reduction to methanol.[106] Further, Ullah *et al.* carried out photothermal CO_2 reduction over transition metal (Cu, Co) loaded CeO_2 and found that transition metal loaded CeO_2 exhibits the highest activity as well as selectivity towards methane production compared to pristine CeO_2. The improved photoactivity was attributed to the generation of hot electrons from transition metals which directly activate the CO_2 molecule to undergo smooth degradation and further create *in situ* vacancies in the CeO_2 support which act as localized charge density sites.[206]

In addition to these, a number of articles have recently been reported for various heterostructures/composites of CeO_2 with different metal oxides,[207,211] metal sulphides[212,213] carbonaceous materials,[214–218] *etc.* For example, Wang *et al.* prepared an ordered mesoporous (OM) CeO_2–TiO_2 composite of 2D hexagonal structure with a high specific surface area and hierarchical porosity by using SBA-15 as the template. The introduction of CeO_2 species increased the surface chemisorbed oxygen of the ordered mesoporous TiO_2 and effectively extended the spectral response of the nanohybrid from UV to visible. The composite was effectively utilized for CO_2 photoreduction under simulated solar light with excellent selectivity and catalytic efficiency. The work demonstrated that the 3DOM CeO_2/TiO_2 catalyst showed the highest CO production, *i.e.* nearly 70 mmol g_{cat}^{-1}, and nearly 11.5 mmol g_{cat}^{-1} CH_4 during 325 min light irradiation. The higher activity was attributed to the 2D-open pore structure, which allows fast interparticle reactant diffusion, and the presence of CeO_2 which helped in the effective electric field formation through which photogenerated electrons effectively drifted from the TiO_2 surface to CeO_2 where they took part in the photoreduction reaction.[207] In another work, Dai *et al.* synthesized a series of CeO_2/Bi_2MoO_6 microsphere nanocomposites (0D–2D) towards CO_2 photoreduction and studied the inside mechanism. They found that the CeO_2 surface strengthens the bonding of CO_2 and enhances the formation of intermediates like CO_3^{2-} and HCO_3^-. Moreover, the heterojunction accelerates electron–hole transfer and separation which ultimately uplifts the reduction activity. For this system, the total yield of CH_3OH and C_2H_5OH was 58.4 μmol g_{cat}^{-1} over 5C-BM, which was about 4.1 and 1.9 times higher than that of the neat CeO_2 (14.1 μmol g_{cat}^{-1}) and Bi_2MoO_6 (30.9 μmol g_{cat}^{-1}), respectively.[211] Again, Dong and co-workers developed a very interesting p–n heterojunction composite of Cu_2O/CeO_2 for photon driven CO_2 reduction. They found that the deposition of Cu_2O over the CeO_2 surface created more surface defects and also accelerated the charge transfer process at the Cu_2O and CeO_2 interface. Furthermore, Cu_2O plays an important role by creating Lewis acid–base sites, while the oxygen vacancy over CeO_2 increases the pace of CO_2 reduction to CO. In brief they systematically studied the reaction pathway and the mechanism as presented in Fig. 9(f), and concluded that first Cu atoms of Cu_2O perfectly bound the carbon atoms of CO_2 molecules *via* d-orbital electrons leading to the formation of the carboxylate ion. Further, under light irradiation photogenerated electrons transferred from Cu to the C–O bond of carboxylate, and the O atom of carboxylate interacted with the oxygen vacancy (O_v) on the CeO_2 surface, and then the O atom transferred to O_v. Finally, the above interaction promoted the breaking of the C–O bond of the adsorbed carboxylate species, and thus the CO molecule was generated.[210]

In addition to oxide heterostructures, metal sulphides have also been used as a component for CeO_2 in the CO_2 reduction reaction. For example, a core–shell structure of CdS@CeO_2 towards visible light assisted CO_2 reduction was reported by Ijaz *et al.* In the experiment performed, two types of reduction products are observed, *i.e.* methanol as the major product because of the thermodynamic and kinetic concern and methane as the minor product. The type II heterojunction at the core/shell interface enhances the photogenerated charge pair separation and hence improves the stability of the CdS core as the CeO_2 outer layer inhibits the photocorrosion of CdS. In brief, under the visible light irradiation condition photogenerated electrons and holes were produced on the surface of CdS, and then the electrons transferred from CdS to the conduction band of CeO_2. Further, on the surface of CeO_2 these electrons reduced the adsorbed CO_2 into the negative and metastable superoxide ($^{\bullet}CO_2^-$) radicals, which then eventually led to the formation of CH_4 at the rate of 1100 μmol g^{-1} for 8 h.[212]

Liang's group demonstrated an interesting synthetic strategy for the formation of a hollow heterostructure of g-C_3N_4@CeO_2 with enough oxygen vacancies by using SiO_2 as a template. The catalytic ability of the vacancy enriched heterostructure was tested towards CO_2 photoreduction and the obtained products were CO (16.8 μmol g^{-1}), CH_3OH (5.2 μmol g^{-1}) and CH_4 (3.5 μmol g^{-1}), demonstrating the higher ability of this heterostructure compared to most of the other reported g-C_3N_4 based photocatalysts. Further, the apparent quantum efficiency for CO_2 reduction to methane was found to be 17.1% at 525 nm. They concluded that the reason behind the increment in the performance is mainly due to its unique structure and a delayed charge pair recombination rate as confirmed from SPS analysis (shown in Fig. 9(g)). Although both g-C_3N_4 and CeO_2 showed SPS response the 3D heterostructure exhibited the most intensive response under visible light which confirmed the effective charge carrier separation.[214] As shown in Fig. 9(h), the separation of excitons occurs at the g-C_3N_4 and CeO_2 interface, while the photogenerated electrons accumulate over the CeO_2 surface where the electrons combine with Ce^{4+} to generate Ce^{3+}. Further, Ce^{3+} reacts with the gas phase CO_2 to form $^{\bullet}CO_2^-$ which is further reduced to yield CO, and hence the yield of CO is very high in this case. Further in the presence of adsorbed H and $^{\bullet}CO_2^-$ hydrogenation occurs resulting in other products like methanol and methane.

6. Nitrogen reduction reaction (NRR)

NH_3 is considered as an important chemical for both industries (explosive, resin, plastics and fibres) and agriculture (fertilizer). Recently, the global need for ammonia has seen a sharp increment due to its additional application, *i.e.* as a carbon-neutral fuel and specifically as a potential energy carrier due to its high hydrogen density (17.6 wt%), easy handling/storage and low liquefiable condition (8 bar). Currently, about 150 million tonnes of ammonia is produced per year *via* the traditional energy-intensive Haber–Bosch process (HB) to satisfy the population's food requirement and various other applications. This HB process generally operates under extremely harsh conditions, *i.e.* 400–450 °C and 100–200 atm, and also utilizes 1–3% of global electrical energy (*i.e.* 3.5×10^4 to 5×10^4 J $g_{NH_3}{}^{-1}$). Moreover, the supplied H_2 comes from natural gas (3–5%), and unfortunately releases a substantial amount of CO_2 (1.87 tons per ton of NH_3) which creates an environmental catastrophe.[219–225] To replace the HB process, a renewable, scalable, and eco-friendly strategy towards ammonia production is highly essential. Among different ongoing strategies, photocatalytic reduction of N_2 to NH_3 is a very hot topic of research towards the development of renewable technologies. Photocatalytic nitrogen reduction generally operates under mild reaction conditions and utilizes renewable feedstock, *i.e.* solar light and water. So far many photocatalytic systems have been developed and tested for effective nitrogen fixation. It is found that the materials with intrinsic surface defects are the most suitable candidates for this process.[220] In this perspective, CeO_2 with surface oxygen defects and Ce^{3+} has emerged as one of the active catalytic systems for the NRR.[226–232]

In this context, Qi *et al.* using first principles calculations investigated the NRR process over CeO_2 and found that defective CeO_2 with Ce^{3+} sites (Lewis acid) facilitates N_2 adsorption (Lewis base) *via* an acid–base adduct mechanism as shown in Fig. 10(a). The exposed CeO_2 sites on CeO_2((111), (110), (100)) can cause N_2 to get adsorbed in a lying down manner, which encourages N_2 activation and thus leads to an efficient reduction. The surface oxygen vacancy weakens the adsorbed N≡N bond strength and lowers the adsorption energy of the N_2H^* intermediate as shown in Fig. 10(b) and thereby facilitates further reduction. In brief, in the pristine CeO_2 with (111), (110) and (100) exposed facets, N_2 adsorbs on the surface of Ce sites in a standing up manner indicating weak physical adsorption. Hence the N_2 molecule can't be activated on the surface of perfect/pristine CeO_2 and further, the energy barrier for the first protonation of N_2^* seems to be very high leading to inefficiency of the NRR. However, defective CeO_2(111), (110) and (100) facets containing multiple oxygen vacancies and unsaturated Ce^{3+} Lewis acid cluster sites (tri/bi and tetra-Ce sites) could cause N_2 to be adsorbed in a lying down manner, which further promotes N_2 activation. Moreover, the unsaturated tri and bi-Ce sites could stabilize the intermediate N_2H^*, while lowering ΔG for the first protonation, and then the alternate mechanistic pathway of ammonia formation proceeds. Further, it was found that the NRR activity over the different planes of CeO_2 is determined by their unsaturated Ce sites which are in the following order: (100) > (110) > (111), as the (100) plane contains tetra and tri-Ce sites.[226]

Different CeO_2 based electrocatalysts for NRR activity have also been reported so far[227–229] with a high production rate and selectivity. For example, Xu *et al.* prepared oxygen vacancy enriched CeO_2 nanorods and achieved a great enhancement for the electrocatalytic NRR. However, no significant works regarding CeO_2 and CeO_2 based materials have been explored in the field of photo-fixation of N_2 (PNRR). Among the countable research works, Feng *et al.* prepared a series of ternary photocatalysts $CeCO_3OH$/g-C_3N_4/CeO_2 by using $CeCl_3$ and graphitic carbon nitride (g-C_3N_4) as reaction precursors *via* facile *in situ* self-sacrificing hydrothermal methods. Without using any sacrificial agent, the photocatalyst prepared at 180 °C exhibited the highest nitrogen photoreduction activity, *i.e.* 1.16 mM g^{-1} h^{-1}, which was four times that of pristine g-C_3N_4. The enhanced nitrogen photofixation performance was attributed to the surface defects in CeO_2 where Ce^{3+} acts as a chemisorption site for N_2 molecule adsorption and subsequent activation and the heterostructure interface provides a higher charge transfer and separation efficiency.[230] In another case, Jia *et al.* proposed an innovative synthesis idea of the Au–CeO_2 nanostructure, unlike the reported core–shell structure, *via* a facile wet-chemistry route, where crystalline CeO_2 was selectively grown over the ends of gold nanorods (Au NRs) in the presence of a small amount of bi-functional K_2PtCl_4. A large number of oxygen vacancies were generated in the surface grown ceria which further enhanced the adsorption and the subsequent reduction of di-nitrogen molecules. They tuned their longitudinal plasmon wavelengths finely so that the materials can be adjusted as closely as possible to the laser wavelength as shown in Fig. 10(c). Further, the generation of plasmon-induced hot electrons and the presence of oxygen vacancies enabled the unique structural Au/end-CeO_2 to function as a photocatalyst for nitrogen photofixation. The obtained nanostructured catalyst under 808 nm laser illumination led to a high rate of production of NH_3, *i.e.* 114.3 μmol h^{-1} g^{-1}, which was 6.2-fold more in comparison to the other synthesized core@shell (Au@CeO_2) nanostructure (Fig. 10(c)). As a proof-of-concept, the photocatalytic N_2 fixation ability of the Au/end-CeO_2 nanostructures was also evaluated under 1 sun illumination and the NH_3 generation rate was found to be 25.6 μmol h^{-1} g^{-1}.[113] The author's group have also studied different CeO_2 based materials for photocatalytic nitrogen fixation.[231,232] For example, 3D/2D-FeS_2–FeP–CeO_2 nanohybrids with high surface defects were successfully synthesized through an *in situ* hydrothermal technique followed by a combined sulphidation and phosphidation technique. The as-prepared samples were tested towards PNRR under UV-vis light without the use of any organic scavenger or noble metal co-catalyst. CeO_2 acts as a building block photocatalyst and supports the FeP/FeS_2 particles, and under light irradiation FeS_2 acts as an electron donor and injects photoelectrons on to the CeO_2. Further the presence of oxygen vacancies along with FeP encouraged the productive N_2 activation and photoreduction to ammonia. The key to the remarkable photocatalytic performance was the presence of Fe based materials where FeP serves as the catalytic site for N_2 adsorption and facilitates the photogenerated charge transfer mechanism from CeO_2 to nitrogen as

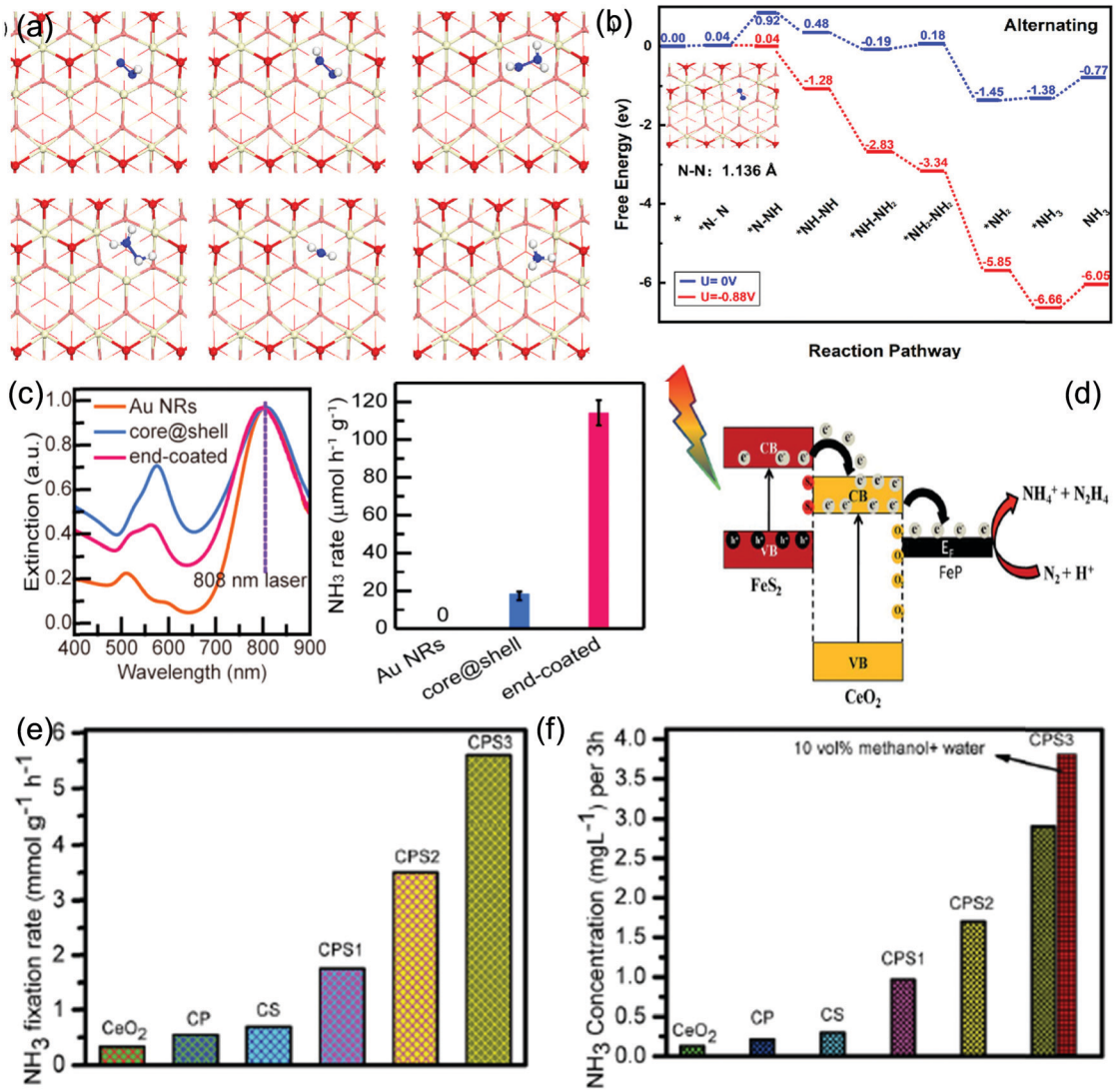

Fig. 10 (a) Optimized geometries of the NRR pathway on defective CeO_2(111). (b) Corresponding Gibbs free energy profiles. Reprinted from ref. 226 with permission from Elsevier. (c) Extinction spectra of three photocatalyst nanostructures and N_2 photofixation rates of Au nanorods, Au@CeO_2 and Au-end coated CeO_2 photocatalysts under NIR light illumination. Reprinted with permission from ref. 113, copyright 2019 American Chemical Society. (d) Proposed mechanism of nitrogen reduction over FeS_2/P-CeO_2 based defective materials. (e) and (f) NH_3 concentration from PNRR over a CeO_2 based catalyst in acidic medium and distilled water.[231] Reproduced by permission of The Royal Society of Chemistry.

shown in Fig. 10(d). The optimized FeP–FeS_2–CeO_2 displayed a very high ammonia production, *i.e.* 2.91 mg L^{-1}, without a sacrificial agent whereas in the presence of aqueous methanol solution, the ammonia production rate was increased significantly. This suggests that methanol both acts as a sacrificial electron donor and produces $CO_2{}^{*-}$ which facilitates the N_2 fixation ability. Further, the nitrogen fixation rate was 5.66 mmol h^{-1} g^{-1} with selectivity in acidic distilled water under mild reaction conditions (Fig. 10(e and f)).[231]

7. Photocatalytic pollution abatement

The 21st century is the era of rapid development covering all sectors of the world but the serious side effect of this progress may result in an environmental catastrophe. The continuous rise of industrial activities and different technological advancements have damaged the growth of society by releasing their additional waste to water bodies, soil and air without proper treatment causing a serious threat to biodiversity. Mainly the wastewater effluents contain maximum contaminants in the form of various organic pollutants such as dyes, phenolic compounds, antibiotics, halogenated hydrocarbons and inorganic toxic pollutants such as highly dangerous heavy metals and radioactive nuclides.[233–239] These pollutants are highly toxic and take a very long time to degrade naturally. So the effective removal and degradation of these pollutants have taken many years of research. A variety of technologies such as chemical oxidation, adsorption, electrochemical conversion, and biodegradation have been used so far but most of them are highly energy demanding and cannot

be used on a regular basis.[240–245] However, the photocatalytic detoxification process has emerged as a more efficient, cost-effective and green strategy which has the ability to clean up all the detrimental pollutants from wastewater as well as air bodies. In this technique, highly energetic radicals such as hydroxyl, superoxide, and hydrogen peroxide along with photogenerated electrons and holes are produced which effectively convert the organic/inorganic pollutant to a non-toxic form very quickly.[246–248] With regard to this, many researchers have developed different photocatalytic materials for their effective utilization towards pollutant removal from different sources.

In the context of the environment cleanup process, various nanostructured CeO_2 and CeO_2 based materials have been reported for air purification and wastewater treatment by efficient photocatalytic degradation/mineralization of different dyes (RhB, MB, acid orange, eosin yellow, *etc.*),[249–274] antibiotics[275–284] and organic pollutants (phenol-based materials),[285–289] as summarized in Table 3. Morphology alteration enhances the surface defects such as Ce^{3+} state and oxygen vacancies, which increases the light absorption parameter with a red-shifted absorption edge and also retards the photogenerated electron–hole recombination rate. Further, these sites act as strong binding and dissociation sites for adsorbate molecules, and hence act as good sites for the photocatalytic degradation process. And it was also found that these CeO_2 materials generate more radical species (hydroxyl and superoxide) because of the prolonged lifetime of excitons and the presence of surface defects. Recently, Amoresi *et al.* studied the photocatalytic decolourization efficiency of RhB over different morphology oriented CeO_2. According to theoretical models and experimental studies, it was found that the photo-degradation rate varies with the morphology and exposed planes. Since the electron density is different for different planes and is of the order (110) > (100) > (111) > (311), different morphologies showed different photocatalytic activity. For the bean (100) shaped morphology, h^+ are the dominant species and for rods (110) it is e^-, while e^-/h^+ are equally responsible for the photocatalytic activity of hexagon (311). For the (111) dominant morphology, OH* act as the major species for degradation purposes, since they have strong e^-/h^+ interaction. Hence different morphologies exhibited different photoactivity for a selected pollutant molecule.[62]

Dye degradation

Zhang *et al.* reported CeO_2 hierarchical nanowires (Fig. 11(a)) and nanorods (Fig. 11(b)) grown on Cu substrates for the photocatalytic degradation of methyl orange (MO) and found that as compared to CeO_2 NPs, the 1-D nanostructure exhibited higher degradation efficiency. Both CeO_2 HNRs and HNWs removed 98.2% and 99.3% of MO under light irradiation for 180 min, revealing a performance which is substantially higher than that of the commercial CeO_2 NPs (68.8%) and P25 (89.5%) as shown in Fig. 11(c) respectively. The high performance in comparison to CeO_2 NPs was achieved only due to their hierarchical 1D nanostructure derived active sites, resulting in a shorter diffusion length of photogenerated holes and increased surface areas. Further, of the two 1-D structures, although both the materials possessed a 3.2 eV band gap, the nanowires exhibited higher absorption in the wavelength range between 400 and 750 nm (Fig. 11(d)), suggesting higher photonic energy absorption.[77] Further, Yu *et al.* reported uniform single crystalline hexagonal CeO_2 nanosheets for RhB degradation and found that the degradation efficiency of the above nanosheets was more than that of the conventional CeO_2 nanoparticles. The activity improvement was attributed to their 2D nanosheet structure which suppressed the charge pair recombination and their intrinsic single-crystal structure which decreased the charge transfer resistance, thereby yielding much stronger reducible electrons.[79] Further, Arul *et al.* synthesized 3D hierarchical rose-flower-like CeO_2 where CeO_2 nanosheets are stalked to form a flower. Under UV light irradiation, the flower like catalyst showed a degradation rate of 65% for the AO7 dye. The 2D NSs provided better diffusion of generated holes and reduced the agglomeration of the 2D NSs which was responsible for the enhanced activity.[249] In another experiment, Yuan *et al.* reported hierarchical CeO_2 sheets for the photocatalytic decomposition of toxic acetaldehyde. They found that CeO_2 HSs decomposed acetaldehyde more efficiently than CeO_2 NPs and as well as the well known P25. This superior degradation activity is mainly attributed to the high surface to volume ratio of the catalyst and the presence of surface defects.[250] Though nanostructured CeO_2 possesses an impressive degradation property it is active only under UV-light illumination. Hence, the fabrication of a CeO_2 based heterostructure is investigated, which visibly improves the interfacial charge transfer, light absorption and the charge separation and lowers the recombination resulting in enhanced photocatalytic degradation. So far, nanostructured CeO_2 has been combined with different metal oxides,[251–257] sulphides,[258–262] carbonaceous materials,[263–267] *etc.* for efficient dye degradation. For example, Arul *et al.* reported CeO_2/Fe_2O_3 spindles as recyclable photocatalysts for the degradation of Eosin Yellow (EY) under visible light irradiation. The degradation was achieved in a very short duration of time (98% in 25 min) in comparison to neat CeO_2 and Fe_2O_3 NRs, because of the excellent charge separation and transfer property derived from the heterostructure (Fig. 11(e)). Fig. 11(f) shows the recycling study of the CeO_2/Fe_2O_3 heterostructure, where the photocatalyst was found to be very stable and the photocatalytic efficiency was reduced by less than 10% even after 4 cyclic runs. Further they calculated the electrical energy per order of the photocatalyst, a term used to calculate the electrical energy required to remove unit mass of the pollutant. From the calculations, they found that the photocatalyst required much less energy to degrade the EY dye by one order of magnitude. Hence they deduced that the heterostructure possesses greater potential for use as a visible light driven catalyst. They deduced the photodegradation mechanism as shown in Fig. 11(g): upon light irradiation photogenerated electrons migrate from Fe_2O_3 to the Ce 4f band where they react with oxygen to generate superoxide radicals, while holes migrate from the VB of CeO_2 towards the VB of Fe_2O_3 yielding hydroxyl radicals. Both the superoxide and hydroxyl radicals were found to be essential for the photodegradation process.[252] Another low cost recyclable CeO_2–metal oxide heterostructure was reported by Tian *et al.*, where CeO_2 nanoparticles assembled on the rough surface of TiO_2

Table 3 Complete results of the pollutant degradation performance of CeO_2 and CeO_2 based heterostructures

Catalyst	Light source	Reaction conditions	Activity	Ref.
CeO_2 hierarchical NRs	White light, 500 W Xe lamp	20 mg L^{-1} MO, 20 mg	98.2% in 180 min	77
CeO_2 hierarchical NWs			99.3% in 180 min	
Single crystalline mesoporous CeO_2 nanosheet	250 W high pressure mercury lamp	1.0×10^{-5} mol L^{-1} RhB, 20 mg	Nearly 80% in 120 min	79
Ordered meso-CeO_2	1000 W Xe lamp ($\lambda > 420$ nm)	70 mg L^{-1} AO 7, 50 mg	95% in 7 h	89
Flower-like CeO_2	UV light ($\lambda = 365$ nm)	0.3 mM AO 7, 1 cm^2	~65% in 10 h	249
CeO_2 microspheres	1000 W Xe lamp ($\lambda > 420$ nm)	50 mg L^{-1} AO 7, 50 mg	69.7% in 180 min	268
CeO_2 NSs	450 W Xe lamp ($\lambda > 420$ nm)	26.7 μM MB, 30 mg	90% in 6 h	269
CeO_2 NCs	310 nm $< \lambda <$ 400 nm	RhB, 50 mg	30% in 2 h	270
CeO_2 lamellar	UV light, 120 W uviol lamp	5 mg L^{-1} MB, 50 mg	96.5% in 60 min	271
Octahedral CeO_2	UV	5, 20 mg L^{-1} MO, 20 mg	98.1% in 5 h	272
CeO_2 NTs			92.8% in 5 h	
Au/CeO_2	400 W Xe lamp ($\lambda > 400$ nm)	10 mg L^{-1} MO, MB, 2 mg	80% in 6 h, 95% in 5 h	273
$BiVO_4$/CeO_2	Halogen lamp, visible ($\lambda > 400$ nm)	2×10^{-5} M MB, 50 mg	~80% in 30 min	251
CeO_2/Fe_2O_3 nanospindles	White, 150 Xe lamp	0.1 mM EY, 1 mg	98% in 25 min	252
CuO/CeO_2	15 W UV tube	0.15 mM MB, 100 mg	91.3% in 2 h	253
CeO_2/TiO_2 nanobelt	350 W mercury lamp (max. emission 356 nm)	20 mg L^{-1} MO, 20 mg	100% in 25 min	254
	300 W Xe arc lamp ($\lambda > 410$ nm)		87% in 25 min	
CeO_2–TiO_2	300 W Xe arc lamp ($\lambda > 400$ nm)	Bph-dye	~72% in 3 h	255
CeO_2/ZnO nanodisks	Natural solar light	50 mg L^{-1} direct blue 15, 50 mg	93% in 5 h	256
Hierarchical CeO_2/ZnO	300 W Xe lamp	10 mg L^{-1} RhB, 50 Mg	96% in 80 min	257
CdS/CeO_2	154 W halogen lamps	3 mg L^{-1} MB, 20 mg	70% in 120 min	258
CdS NRs–CeO_2 NPs	300 W Xe lamp	40 mg L^{-1} dye, 40 mg	96.68% in 48 min	259
CdS NWs/CeO_2 nanoparticles	300 W Xe arc lamp ($\lambda > 400$ nm)	10 mg L^{-1} nitroaromatics, 6 mg	4-nitrophenol ~90% in 3 min	260
Flower like CeO_2/MoS_2	150 W Xe lamp-visible light	25 mg L^{-1} MO, 25 mg	96.1% in 90 min	261
CeO_2/CuS composite nanofibers	Strip blue LED lamp	3 mg L^{-1} MB	96.38% in 40 min	262
CeO_2/C_3N_4	300 W Xe lamp ($\lambda > 400$ nm)	10 mg L^{-1} MB, 100 mg	95% in 2 h	274
CeO_2/g-C_3N_4	300 W Xe lamp ($\lambda > 400$ nm)	10 mg L^{-1} MB, 25 mg	~98.59% in 3.5 h	263
CeO_2/g-C_3N_4	36 W UV lamp (OS72) with a wavelength of 254 nm	10 mg L^{-1} MB, 50 mg	90.1% in 180 min	264
CeO_2/g-C_3N_4	8 W Xe lamp	10^{-5} M concentration, 10 mg	97% (MB dye) and 96% (Rh-B dye) in 60 min	265
rGO/CeO_2 NCs	Hg lamp UV	1×10^{-5} M MB, 30 mg	~87% in 90 min	266
rGO/CeO_2	Visible light source with intensity 14.5 W m^{-2}	1 mM MO	88.3% in 60 min	267
CeO_2	300 W Xe lamp	10 mg L^{-1} CIP, 50 mg	More than 90% in 15 min	275
Hollow BiOCl@CeO_2	300 W Xe lamp ($\lambda > 400$ nm)	10 mg L^{-1} TC, 50 mg	92% for TC in 120 min	276
CeO_2/Ti_3C_2–MXene	350 W Xe lamp	10 mg L^{-1} TC, 30 mg	80.2% of TC in 60 min	277
Nebula-like ZnO/CeO_2@HNTs	300 W Xe lamp (780–1100 nm)	20 mg L^{-1} TC, 30 mg	87% in 60 min	278
Ag_2O/CeO_2	300 W Xe lamp ($\lambda > 420$ nm)	10 mg L^{-1} enrofloxacin, 50 mg	87.1% in 120 min	279
CeO_2/Co_3O_4 porous nanosheet	Xe lamp (350 nm $< \lambda <$ 780 nm)	10 mg L^{-1} MB	96.42% in 70 min	280
		5 mg	85.35% in 30 min	
		20 mg L^{-1} TC		
Bi_2O_3@CeO_2	500 W Xe lamp ($\lambda > 420$ nm)	10 mg L^{-1} TC, 20 mg	100% in 180 min	281
Shuttle-like CeO_2/g-C_3N_4	150 W high pressure Xe lamp ($\lambda > 420$ nm)	10 mg L^{-1} NOR, 50 mg	88.6% in 60 min	282
CeO_2/nitrogen-doped carbon quantum dot/gC_3N_4	300 W Xe lamp ($\lambda > 420$ nm)	20 mg L^{-1} TC, 100 mg	100% in 60 min	283
2D-CeO_2 on 2D-MoS_2	250 W Xe lamp ($\lambda > 420$ nm)	10 mg L^{-1} CIP, 50 mg	88.5% in 120 min	284
Defective CeO_2	Direct sunlight visible region (420–800 nm)	50 ppm phenol 200 mg	35% in 180 min	105
		50 ppm cholorphenol	98% in 180 min	
		50 ppm bromophenol	96% in 180 min	
		50 ppm nitrophenol	99% in 180 min	
CeO_2/g-C_3N_4 nanosheet	300 W Xe lamp ($\lambda > 420$ nm)	Phenol, bisphenol-A	93.7% in 80 min (BPA) 97.5% (phenol)	285
CeO_2/ZnCo–layered double hydroxide	—	20 mg L^{-1} phenol	99.8% in 30 min	286
CoS/CeO_2	300 W Xe lamp ($\lambda > 420$ nm)	25 mg L^{-1} phenol, 50 mg	85.5% in 60 min	287
		20 mg L^{-1} TC	96.5% in 60 min	
CeO_2-rod/g-C_3N_4	300 W Xe lamp ($\lambda > 300$ nm)	0.10 g benzylamine, 50 mg	81.2% in 5 h	288

nanobelts producing the CeO_2–TiO_2 heterostructure. The heterostructure was tested for MO degradation under both UV and visible light, and they found that MO molecules were preferentially captured by CeO_2 nanoparticles and were degraded by the free radicals and further released to the solution, and hence a capture, photodegradation and release process was followed. The heterostructure possessed enhanced photoactivity due to the efficient charge separation and transfer due to the well matching energy band between CeO_2 and TiO_2 and the large active surface area.[254] Further Parida and co-workers prepared a series of 2D/2D-BiOI/CeO_2

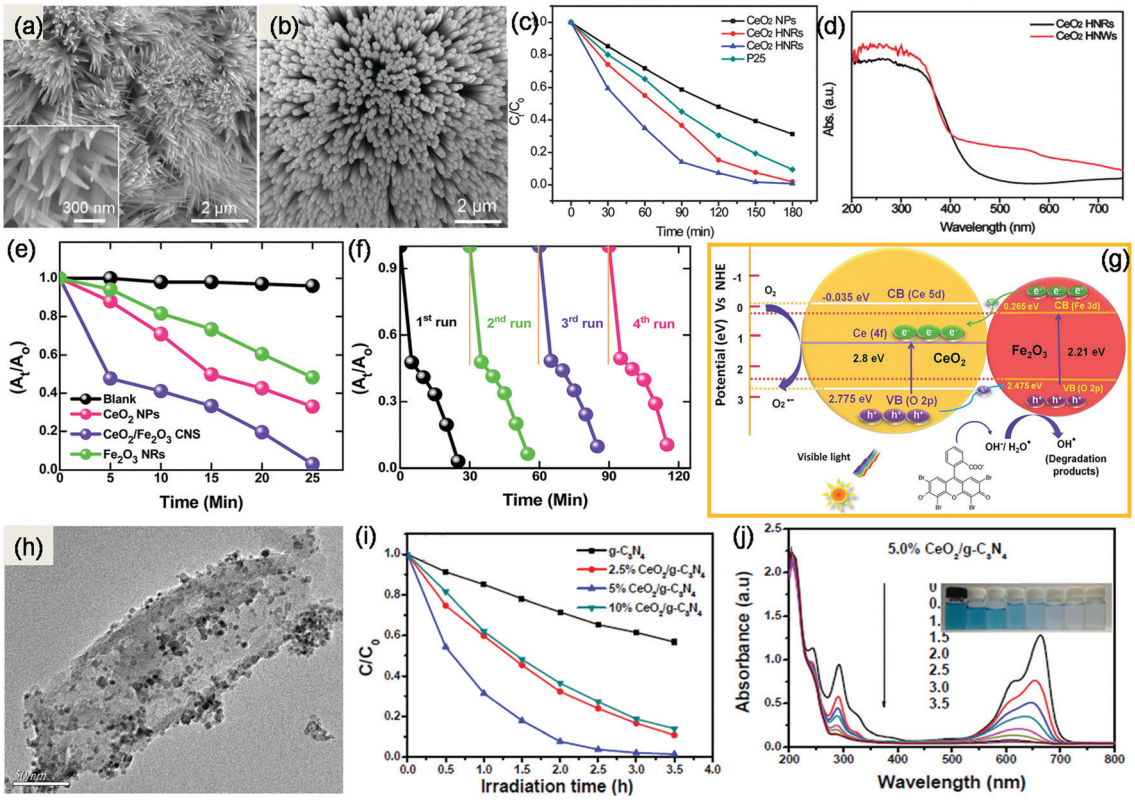

Fig. 11 (a and b) SEM micrographs of CeO_2 nanowires and nanorods respectively. (c) Photocatalytic degradation of MO over CeO_2 HNRs and CeO_2 HNWs in addition to that over CeO_2 NPs and P25 with respect to light irradiation time. (d) UV-DRS spectra of CeO_2 nanowires and nanorods.[77] Reproduced by permission of The Royal Society of Chemistry. (e) Degradation efficiency of the blank EY with CeO_2 nanoparticles, CeO_2/Fe_2O_3 and Fe_2O_3 nanorod catalysts *versus* irradiation time. (f) Reusability test of the CeO_2–Fe_2O_3 photocatalyst in degrading EY under visible light irradiation. (g) Proposed photodegradation mechanism of CeO_2/Fe_2O_3 CNSs in degrading the EY dye under visible light irradiation.[252] Reproduced by permission of The Royal Society of Chemistry. (h) TEM micrographs of CeO_2–g-C_3N_4. (i) Photodegradation efficiency of the MB dye by g-C_3N_4 and CeO_2/g-C_3N_4 catalysts *versus* light irradiation. (j) Changes in the ultraviolet-visible absorbance spectra of MB dye solutions with optimized CeO_2–g-C_3N_4.[263] Reproduced by permission of The Royal Society of Chemistry.

nanocomposites and tested their effectivity towards RhB decolourization efficiency. Among the very best catalysts, 40%BiOI–CeO_2 was proven to be the best and within a very short time 89% decolourization efficiency was achieved for 100 ppm RhB under sunlight. The major cause behind the enhanced photoactivity was found to be the presence of excess surface oxygen vacancies and better charge separation efficiency through the Z-scheme at the interface.[117] Further, Gu *et al.* reported a heterostructure photocatalyst consisting of one-dimensional (1D) CdS nanorods (NRs) and CeO_2 nanoparticles (NPs). They found that the photocatalytic degradation of RhB was around 97% for the CdS/CeO_2 heterostructure, which was much higher than that of its neat counterparts. The rate constant of CdS/CeO_2 was nearly 28 times and 3.4 times higher than that of neat CeO_2 and CdS respectively, due to the inhibition of electron–hole pair recombination benefitting from efficient electron transfer from CdS NRs to CeO_2 NPs producing effective superoxide radicals. They studied the degradation pathway of RhB and found that after 16 min *N*-de-ethylated intermediates were formed but further with time, these products' intensity decreased down. Further, a high mineralization rate (86% TOC removal) was observed, which confirmed the complete mineralization of RhB.[259] Additionally, She *et al.* reported an important synthetic strategy to design a beautiful heterostructure between the CeO_2(111) cube and the g-C_3N_4 nanosheet as shown in Fig. 11(h and i). The heterostructure exhibited 98.59% degradation efficiency of MB within 3.5 h under visible light which was much higher than that of the neat materials. The variation in the optical absorption spectra of MB degradation over 5%CeO_2–gC_3N_4 is shown in Fig. 11(j). With light irradiation, as the time passed the colour of MB gradually disappeared which confirmed the photodegradation process.[263] Verma *et al.* reported an *in situ* CeO_2/rGO nanocomposite prepared through the one step ammonia assisted hydrothermal method for the elimination of MO under visible light. The heterostructure between CeO_2 (0D) and graphene (2D) increased charge separation and transportation ability simultaneously and extended the range of the solar absorption spectrum as well as increased the dye molecule absorptivity over its surface. In brief, under light irradiation photogenerated electrons and holes are produced over the CeO_2 surface; since rGO acts as a sink, electrons drift to the rGO surface and produce superoxide radicals, while the holes at the CeO_2 surface react with water to generate hydroxyl radicals. Through the π–π interaction between rGO and the MO dye molecule, the dyes are efficiently adsorbed over the surface of rGO where they react with both superoxide and hydroxyl radicals to yield the degraded product.[267]

Antibiotics removal

Nowadays, the excessive use of antibiotics like tetracycline, norfloxacin, enrofloxacin, ciprofloxacin (CIP), *etc.* is a major headache for society, as these are non-biodegradable and cause adverse effects on the ecosystem. Amoresi *et al.* verified the morphological effect of different exposed plane CeO_2 on CIP drug molecule photodegradation. They found that nanostructured CeO_2 with different exposed planes has a site selective tendency for CIP molecule cleavage and yields different degraded products. In brief, the CIP molecule contains multiple functional groups; hence electrostatic potential maps show negative sites corresponding to nitrogen atoms and oxygen atoms of COOH termination and positive sites corresponding to low electron density aromatic rings and cyclopropyl groups as shown in Fig. 12(a). As we have already discussed in the above section, rod and bean morphologies with the (110) and (100) predominant surfaces have a more negative surface layer, hence show higher affinity towards the positive site of the CIP drug during the photodegradation process. On the other hand, the hexagon with the (311) exposed plane and the rod/cube morphology with the (111) exposed plane show good affinity for the negative site of the CIP molecule, as these morphologies contain a more positive surface layer.[62] Further, a number of bismuth based materials along with other low-dimensional materials have been studied with CeO_2 towards the elimination of different antibiotics.[127,276–284] Recently an efficient hollow BiOCl@CeO_2 heterostructured microsphere with type-II staggered-arrangement was reported for the photodegradation of an antibiotic, *i.e.* tetracycline (TC). The authors observed that the above heterostructure degraded 92% TC within 120 min owing to the distinctive hollow structures and better charge carrier transportation and separation. Due to the matched band energy between n-CeO_2 and p-BiOCl an effective p–n junction was formed *via* Fermi level equilibration, which enhanced the interfacial charge transfer, because of which energetic electrons are now available at the CeO_2 surface while holes are present at BiOCl. From the ESR trapping experiment, the authors concluded that both superoxide and hydroxyls were found to be active species, while the higher peak strength of DMPO–O_2^- confirmed the greater participation of superoxide radicals in TC degradation.[276] Liu *et al.* presented a method of preparation of a 1D–2D heterostructure composite between shuttle like CeO_2 and g-C_3N_4 nanosheets and tested its photocatalytic activity towards norfloxacin degradation. The group found that the composite exhibited higher mineralization efficiency, *i.e.* 63.8%, than that of neat 1D-CeO_2 (31.8%) and g-C_3N_4 (39.4%) in a duration of 60 min. They found that gradual shedding of functional groups in norfloxacin molecules occurred during the course of reaction and ultimately the molecules decomposed into CO_2 and H_2O.[282] A series of 2D/2D MoS_2/CeO_2 heterojunctions were successfully prepared by Ji *et al.* following a facile hydrothermal method. In comparison to neat MoS_2 and CeO_2, the optimized MoS_2/CeO_2 heterojunction (88.5%) exhibited higher photocatalytic performance for ciprofloxacin (CIP) degradation as shown in Fig. 12(b). The enhanced degradation efficiency of the MoS_2/CeO_2 heterojunction was attributed to its 2D/2D structure. Due to the presence of an effective 2D–2D interface, the photogenerated charge carriers were effectively separated and transferred, and meanwhile, the generated oxygen vacancies broadened the light absorption range of the heterojunction and overall both the factors helped to generate reactive oxidizing

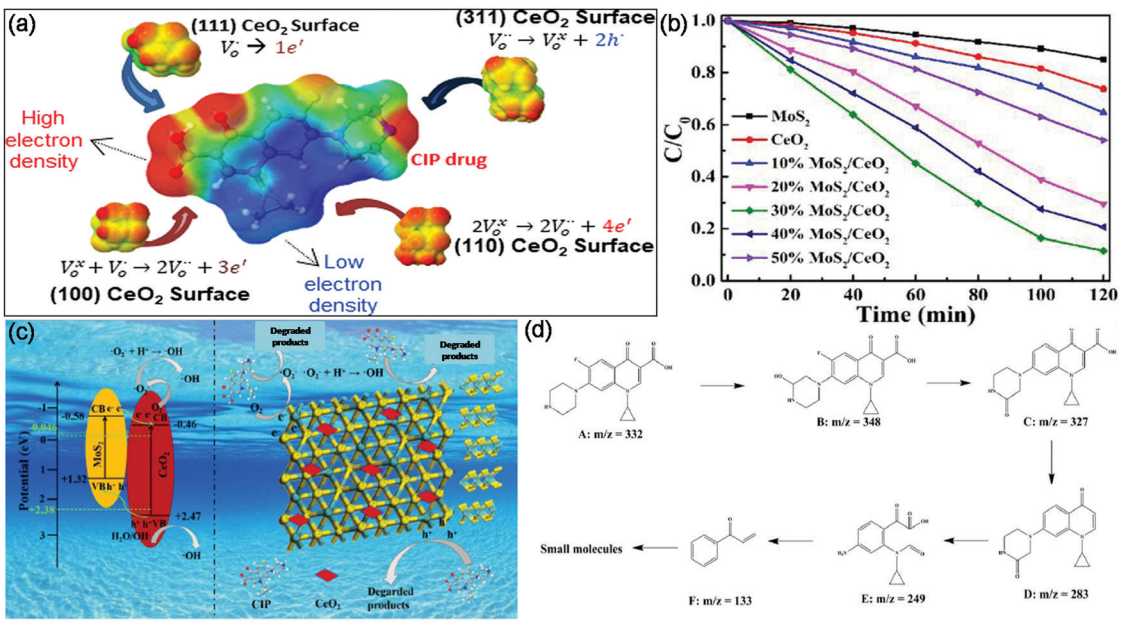

Fig. 12 (a) Electrostatic potential maps showing different positive and negative sites for the ciprofloxacin molecule and the attacking affinity of (111), (311), (110), and (100) surfaces of CeO_2 towards CIP. Reprinted with permission from ref. 62, copyright 2019 American Chemical Society. (b) Degradation efficiency of the CIP drug in the presence of different MoS_2/CeO_2 samples under visible light irradiation. (c) Schematic illustration of charge transfer and generation of active species for photodegradation by optimized MoS_2/CeO_2. (d) Proposed degradation pathway of the CIP drug. Reprinted from ref. 284 with permission from Elsevier.

species for the degradation purpose (Fig. 12(c)). Further, they analyzed the CIP degradation pathway which can be described as follows: as CIP contains a piperazine ring, the generated hydroxyl radicals at first cleaved the piperazine ring to yield B (m/z = 348). Then the degradation reaction continued, where by losing the F and OH groups, C (m/z = 327) was formed. Further, the product D (m/z = 283) was formed from the subsequent cleavage of the carboxyl group. Meanwhile, E (m/z = 249) was formed by the cleavage of the carbon–carbon double bond adjacent to the carboxylic acid group. Finally, F (m/z = 133) was further degraded into smaller molecules, *i.e.* CO_2 and H_2O. The complete degradation pathway is given in Fig. 12(d).[284]

Phenolic compound degradation to non-toxic products

Phenolic group organic materials are now the major threat to air, water and soil. In light of this, different CeO_2 based materials were synthesized and tested for the effective removal of these pollutants. For example, Aslam *et al.* studied the photocatalytic degradation of phenolic compounds such as phenol, 2-bromophenol (bp), 2-chlorophenol (cp) and 2-nitrophenol (np) over a uniform particle sized (11 nm) CeO_2 nanostructure upon exposure to the visible region (420–800 nm) and the complete spectrum of sunlight (Fig. 13(a)) and found an enhanced degradation rate in the full spectrum of sunlight. The exposure to direct sunlight enhanced the defect formation as the irradiated photons help the surface oxygen to escape from the CeO_2 surface as shown in Fig. 13(b). The induction of defects composed of CeO_{2-x} states which act as trap and transfer centers for the effective separation of electrons resulted in the formation of reactive oxidative species. Further, they found that Ce^{3+} played a key role in the generation of superoxide anion radicals (Fig. 13(c)) which were held responsible for complete mineralization of 2-NP and 2-CP, while less toxic aromatic intermediates were formed from phenol and 2-BP.[105] Further, Ma *et al.* reported a type-II n–n heterostructure containing CeO_2 over g-C_3N_4 nanosheets and tested its efficiency towards bisphenol-A degradation. Under visible light irradiation, only 65% removal efficiency was obtained for the g-C_3N_4 nanosheet and 14.4% for CeO_2. However, the removal efficiency was found to be 93.7% at a time span of 80 min as shown in Fig. 13(d) with an apparent rate constant of 0.0199 min^{-1} for the type-II heterostructure. The higher efficiency of the heterostructure is mainly due to the efficient photogenerated charge transfer and separation process across the interface of the n–n junction. As the VB potential of n-type CNNS is unable to produce hydroxyl radicals, only the photogenerated superoxide combined with holes actively takes part in the degradation process as shown in Fig. 13(e).[285] Recently, Gao *et al.* prepared a CeO_2 incorporated ZnCo layered double hydroxide and employed it for phenol degradation in the presence of peroxymonosulfate. The generated oxidising species such as sulphate, hydroxyl, superoxide and holes were held responsible for the 99.8% degradation of phenol.[286] Moreover, Chai *et al.* reported another 1D/2D heterostructure containing CeO_2 NRs and g-C_3N_4 NSs and tested its efficiency towards oxidative coupling of benzylamine. Under UV-visible light irradiation, the 1D/2D heterostructure exhibited a 3 times higher oxidation rate constant compared to neat g-C_3N_4 and CeO_2. They found that the presence of surface defects on CeO_2 was the major reason behind the higher oxidation activity. In brief, the oxygen vacancy traps the oxygen and generates superoxide radicals which break to form hydroxyl species; along with the hydroxyl species, holes also take part in the oxidative coupling process.[288]

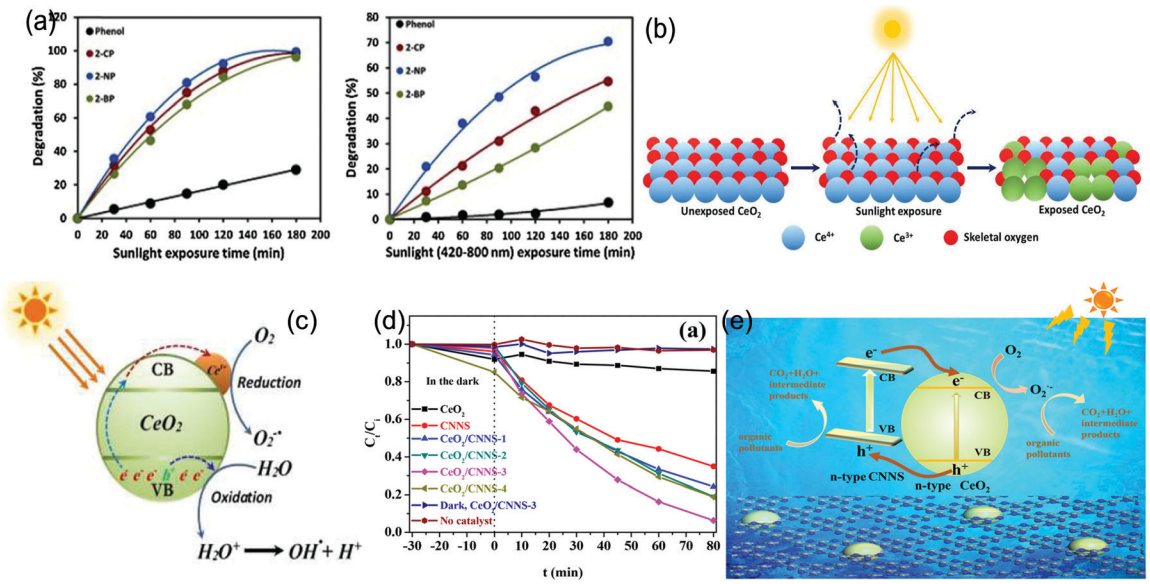

Fig. 13 (a) Degradation curve of 50 ppm phenol, 2-CP, 2-BP, and 2-NP over CeO_2 under direct sunlight and in the visible region (420–800 nm). (b) Schematic illustration of defect formation in CeO_2 under sunlight exposure. (c) Schematic illustration of the generation of active species over defective CeO_2. Reprinted from ref. 105 with permission from Elsevier. (d) Photocatalytic degradation of phenol in the presence of different CeO_2–CNNS heterojunctions. (e) Plausible mechanism of charge transfer and photodegradation of phenol in CeO_2 and CNNS n–n junction. Reprinted with permission from ref. 285, copyright 2019 American Chemical Society.

Heavy metal removal

Worldwide industrialization and technological advancement have brought a lot of troubles to the environment by releasing large quantities of heavy metals to the wastewater which represents a serious threat to global health. Now the heavy metal contaminants are beyond the recommended limit (Cr (0.1 mg L^{-1}), Pb (0.015 mg L^{-1}), As (0.010 mg L^{-1}), Cd (0.005 mg L^{-1}) and Hg (0.00003 mg L^{-1})) and are non-biodegradable which has attracted wide public concern. Unlike organic pollutants or dyes, heavy metals can't be easily broken down biologically or chemically; however they can be reduced/transformed to a less toxic form.[289–294] Hence, a variety of nanostructured CeO_2 and CeO_2 based heterostructures have been designed in this respect.[295–304]

To start with, Wu *et al.* synthesized CeO_2 nanotubes (NTs) *via* the template-assisted method and tested their photocatalytic activity for Cr(VI) reduction in the presence of oxalic acid. Under UV light irradiation, the photocatalytic reduction efficiency of 100 ppm Cr(VI) reached up to 99.6% within 50 min (Fig. 14(a)) with an apparent rate constant of 0.10294 min^{-1}. The effective reduction of Cr(VI) to Cr(III) was confirmed by the XPS spectra shown in Fig. 14(b) where a prominent Cr 2p peak corresponding to Cr(III) is visualised. The template directed CeO_2 nanotube showed good potential towards chromium reduction because of the high photonic energy capture ability arising from its one dimensional characteristic and more importantly the oxalic acid–CeO_2 surface complex formation. In brief, the small molecular weight oxalic acid formed a metal complex with the Ce of CeO_2, and enabled intramolecular electron transfer from the oxalic acid ligand to the Ce metal leading to the formation of organic radicals promoting Cr(VI) reduction under light irradiation as shown in Fig. 14(c).[75] Further, a lot of work has been reported on the photoreduction of Cr(VI) by using different CeO_2 based materials. For example, Yang and co-workers reported 0D/2D CeO_2 QDs/BiOX (X = Cl, Br) nanoplate heterojunctions. Under 5 W white LED light irradiation, the as-prepared 0D/2D heterojunction exhibited high photocatalytic performance not only for the reduction of Cr(VI) but also for the degradation of tetracycline (TC). After 1 h irradiation, the photoreduction rates of Cr(VI) over CeO_2 QDs/BiOBr (CBB) and CBC were found to be 97% and 57% respectively with a pseudo first order kinetics as shown in Fig. 14(d and e). As compared to CeO_2 QD decorated BiOBr, the BiOCl based composite possessed lower photoactivity due to its higher band gap and incapability of visible light absorption. However, the superior photocatalytic activity of the composite compared to pristine materials was attributed to mutual interaction of carriers leading to the efficient transfer and separation of photoexcited carriers and increment in the light absorption ability. Further, the formation of a strongly coupled interface between BiOX nanoplates and CeO_2 QDs and inner Ce^{4+}/Ce^{3+} redox centres enhances the activity further (Fig. 14(f)).[297] Later by the same group, another heterojunction between CeO_2 QDs and Bi_2MoO_6 (BMO) was reported which exhibited more efficient charge carrier transfer and separation capacity. Under light irradiation, the optimized CeO_2–BMO heterojunction showed maximum Cr(VI) reduction (97%) within 90 min, which was higher than that of CeO_2 (30%) and Bi_2MoO_6 (19%) respectively.[298] Parida and his team recently reported a 1D–2D heterostructure between CeO_2 nanorods and $BiFeO_3$ nanosheets and *in situ* decorated nitrogen doped carbon over it. Interestingly, $MCeO_2$–BFO was found to be the best photocatalyst (98.2%) for Cr(VI) reduction compared to the neat counterparts CeO_2 (35%), $MCeO_2$ (56%) and BFO (75%), which was attributed to the effective charge separation and transfer at the heterojunction.[232] Li *et al.* fabricated sandwiched TiO_2@Pt@CeO_2 double shell hollow spheres and tested their photocatalytic performance towards hexavalent chromium reduction. Under solar light irradiation, they found the highest reduction rate for TiO_2@Pt@CeO_2 (1.901) as compared to neat TiO_2 (1.040) and

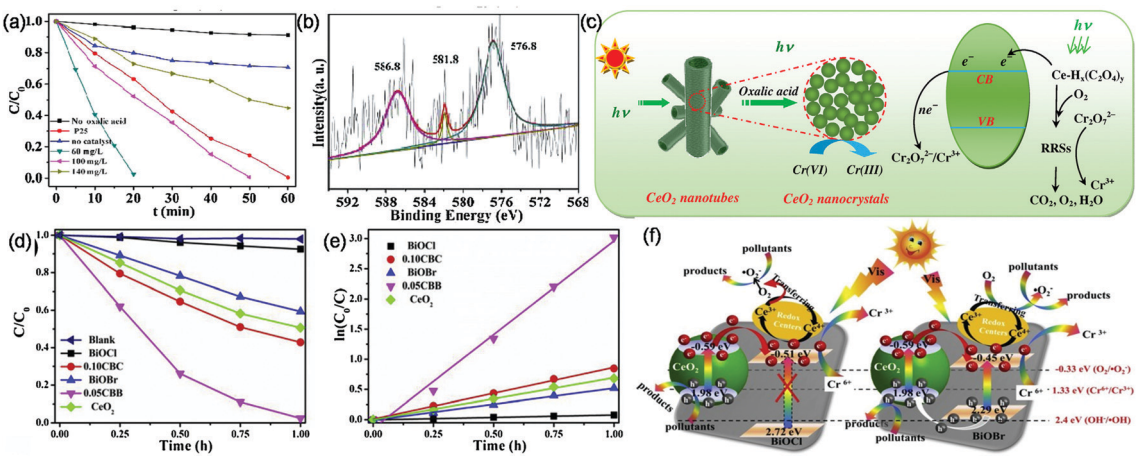

Fig. 14 (a) Photoreduction activity of Cr(VI) solutions of different ppm over CeO_2 nanotubes in the presence of oxalic acid. (b) High-resolution Cr 2p XPS spectra of the CeO_2 catalyst after photoreduction. (c) Proposed scheme of the underlying mechanism of Cr(VI) photoreduction assisted by oxalic acid over CeO_2 nanotubes under UV light irradiation.[75] (d) and (e) The hexavalent chromium photoreduction curves and (e) the pseudo-first-order kinetics curves of BiOX, CeO_2 and BiOX modified CeO_2. (f) Schematic illustration of the photogenerated charge transfer and separation mechanism across CeO_2/BiOCl and CeO_2/BiOBr heterojunction photocatalysts.[297] Reprinted with permission from Elsevier.

CeO_2 (0.992). The enhanced photoreduction activity was mainly due to the unique sandwiched double shell structure and the presence of two oxides (TiO_2 and CeO_2). Further, the addition of the Pt co-catalyst (electron trap site) stores and shuttles the photogenerated excitons, and increases the formation of active radicals responsible for photoreduction reaction.[300] Additionally, Kashinath and his unit reported a facile *in situ* fabrication method for the development of cerium oxide decorated graphene oxide (CeO_2–GO) binary nanocomposites. The hexagonal nano CeO_2 were embedded on the layered graphene oxide sheets *via* a simple microwave irradiation technique and the binary hybrid was tested for the removal of hexavalent chromium ions, dye degradation and antibacterial activities. Under UV (ultraviolet) light irradiation, the binary hybrid showed a rapid hexavalent chromium removal efficiency compared to neat GO and CeO_2.[301]

8. Conclusion and further prospective

Nanostructured CeO_2 and CeO_2 based heterostructure materials with distinct morphology, exposed planes/facets and interfaces have aroused extensive research interest across the globe due to their extraordinary properties and widespread application in the field of photocatalysis. In this review, we have systematically summarized various synthetic routes towards the fabrication of several morphology oriented CeO_2 and its heterostructures as well as their application towards different solar energy conversion-based reactions (hydrogen production, O_2 production, CO_2 reduction and nitrogen reduction) and environmental pollutant (organic/inorganic) remediation. Additionally, theoretical aspects and experimental evidence behind the enhancement in the activity have been well explained. Although a large number of experimental and theoretical studies relating to nanostructured CeO_2 and CeO_2 based materials have been published in recent years, some fundamental aspects still need more attention. However, research in this area still faces a lot of challenges and encouragingly is filled with a lot of opportunities to explore new science. CeO_2 has two key features, *i.e.* abundant oxygen defects and flexible oxidation state ($Ce^{3+} \leftrightarrow Ce^{4+}$) shuttling ability, which make it a promising candidate for various photocatalytic applications. This rare earth oxide and its composites are also extensively studied for different electrocatalytic reactions because upon forming a hybrid, the number of active site increases which strongly influences the electronic structure of the other combining unit (novel metals, metal nitrides, phosphides, *etc.*) which ultimately improves the performance and durability of the system.

But in this review, we mainly focused on the photocatalytic aspect. However, the major shortcoming of CeO_2 as a semiconductor photocatalyst is its low solar light absorption efficiency, fast carrier recombination and higher bandgap. Yet, intrinsic O_v have the ability to alter the band gap of CeO_2 without causing serious damage to the crystal lattice. Hence, a low band gap CeO_2 (3 to 2.6 eV) with a stable surface structure can bring about a revolution in the field of visible light driven photocatalysis. We have also discussed different modification techniques adopted for enhancing the catalytic efficiency of CeO_2 and its composites by taking examples from reported literature.

Adding more to it, the oxygen vacancy is largely responsible for the higher photoactivity; however its controlled generation is very challenging and needs more experimental exploration. Further, the surface oxygen vacancy is very crucial for determining the tensile or compressive strain, which is also an issue for vacancy stabilization. For example, Wu *et al.* stated that tensile strain stabilizes the reduced states of ceria such as oxygen vacancies and surface hydroxyls, while compressive strain destabilizes the reduced states. In addition to these, there are many theoretical and experimental studies which have stated the qualitative influence of the oxygen vacancy and Ce^{3+}, but have not stated how to control the amount of defects to achieve an optimum result. So the controlled generation of surface defects and inhibition of the bulk vacancy still suffer from the lack of a viable facile synthetic route. In order to know more about the electronic and geometric structure of surface vacancies over CeO_2 based materials, more advanced techniques such as scanning tunnelling microscopy, HDAAF, XAFS, XANES, *etc.* should be used in more detail and in a regular manner. Further, the effect of O_v and the Ce^{3+}/Ce^{4+} ratio on photocatalytic reactions needs more *in situ* characterization and computation studies. Additionally, current articles mainly give qualitative ideas on the effect of O_v and Ce^{3+} on catalytic efficiency but it needs direct confirmation which can be achieved by advanced *in situ* characterization and theoretical optimization that can develop a strong understanding of structure–activity interlinkage and hence guide researchers to design extraordinary photocatalytic systems. In brief, the precise synthesis of CeO_2 based systems with a required amount of O_v and Ce^{3+}/Ce^{4+} is very essential as it helps in providing useful information on the catalytic mechanism.

Considerable work has been done with regard to the preparation of morphology oriented CeO_2 based materials and their catalytic as well as photocatalytic application. However, exposure of one facet or controlled growth of one or two facets changes the photoactivity drastically in comparison to the bulk nanostructure. For example, the exposed (100) plane is more suitable for dye degradation, while the (311) plane is more efficient for organic pollutant removal. Hence, this field needs more scientific attention. In this aspect, theoretical studies can show the path of designing desired exposed facet CeO_2 based materials towards a particular type of photocatalytic reaction. In addition to the above stated modification, it is also quite effective to prepare specific nanostructured oriented CeO_2 based systems such as core–shell, porous, hollow structures, hydrophilic/hydrophobic surfaces, *etc.* to achieve benchmark conversion efficiency.

Moreover, a viable, soft and precise synthetic route for designing nanostructured CeO_2 and CeO_2 based materials with higher yield also needs more attention. Different green, environmentally friendly approaches should be followed for the preparation of morphology oriented CeO_2. In addition to using organic solvents and a lot of structure directing agents, common solvents like water, alcohol and biosurfactants should be used for the preparation of the above.

Further, in the preparation of CeO_2 based heterostructures selection of a compatible lower dimensional other half photocatalyst with a distinctly shaped facet is also crucial for constructing an efficient photocatalytic system. So the design of a CeO_2 based photocatalytic system with appropriate interfacial contact between CeO_2 and the other photocatalyst still needs more study. This interface generally inhibits the photogenerated charge pair recombination, and hence the atomic level interaction of different nanostructures also needs more scientific research. In addition to this, the interfacial charge separation and transfer across the interface of two materials and the mechanism behind it are still in ambiguity. The charge transfer may be junctional type (p–n, n–n) or may be Z-scheme type or heterostructure type; hence more thorough theoretical as well as experimental evidence is required in this field. Moreover, coupling of CeO_2 with other materials apart from conventional metal oxides, CdS, g-C_3N_4, and materials like metal phosphides, selenides, and borides can provide a better compatible partner for CeO_2, and hence this field needs more experimental verification. Furthermore, the charge conducting ability of CeO_2 framed systems can be increased by either integrating CeO_2 with highly conductive substances or nucleating CeO_2 on conductive materials like carbon cloth, metal foam, *etc.*

Theoretical analysis of different photocatalytic reactions especially water oxidation, CO_2 reduction and active radical generation over normal and defective CeO_2 with different exposed planes needs more systematic study. Further, there are a handful of attractive reports citing the photocatalytic dye degradation and organic pollutant oxidation, but very few studies have been carried out on photocatalytic water splitting and the NRR. However the oxygen vacancy enriched CeO_2 has shown some outstanding results in photocatalytic water splitting. So, efficient O_v enriched CeO_2 based catalysts with appropriate exposed facets, higher light absorption capacity and lower photogenerated charge recombination still need continuous research. Further, with the increasing efforts of the research community, we strongly believe that future CeO_2 based photocatalytic systems will act as promising materials towards sustainable energy generation and environmental pollution abatement on an industrial scale.

Conflicts of interest

There are no conflicts to declare.

Acknowledgements

The authors are very much thankful to the SOA University management for their support and encouragement.

References

1 J. Tian, Z. Zhao, A. Kumar, R. I. Boughton and H. Liu, Recent progress in design, synthesis, and applications of one-dimensional TiO_2 nanostructured surface heterostructures: A review, *Chem. Soc. Rev.*, 2014, **43**, 6920–6937.

2 C. Xu, P. R. Anusuyadevi, C. Aymonier, R. Luque and S. Marre, Nanostructured materials for photocatalysis, *Chem. Soc. Rev.*, 2019, **48**, 3868–3902.

3 L. Mohapatra and K. Parida, A review of solar and visible light active oxo-bridged materials for energy and environment, *Catal. Sci. Technol.*, 2017, **7**, 2153–2164.

4 P. Kuang, J. Low, B. Cheng, J. Yu and J. Fan, MXene-based photocatalysts, *J. Mater. Sci. Technol.*, 2020, **56**, 18.

5 S. Wageh, A. A. Al-Ghamdi, R. Jafer, X. Li and P. Zhang, A new heterojunction in photocatalysis: S-scheme heterojunction, *Chin. J. Catal.*, 2021, **42**, 667.

6 X. Liu, S. Gu, Y. Zhao, G. Zhou and W. Li, Bi_2WO_6 and Bi_2MoO_6 photocatalysis: A brief review, *J. Mater. Sci. Technol.*, 2020, **56**, 45–68.

7 Y. Li, M. Zhou, B. Cheng and Y. Shao, Recent advances in g-C_3N_4-based heterojunction photocatalysts, *J. Mater. Sci. Technol.*, 2020, **56**, 1–17.

8 Y. Li, X. Li, H. Zhang, J. Fan and Q. Xiang, Design and application of active sites in g-C_3N_4-based photocatalysts, *J. Mater. Sci. Technol.*, 2020, **56**, 69–88.

9 Y. Wang, Q. Wang, X. Zhan, F. Wang, M. Safdar and J. He, Visible light driven type II heterostructures and their enhanced photocatalysis properties: A review, *Nanoscale*, 2013, **5**, 8326–8339.

10 J. Baxter, Z. Bian, G. Chen, D. Danielson, M. S. Dresselhaus, A. G. Fedorov, T. S. Fisher, C. W. Jones, E. Maginn, U. Kortshagen and A. Manthiram, Nanoscale design to enable the revolution in renewable energy, *Energy Environ. Sci.*, 2009, **2**, 559–588.

11 K. L. Materna, R. H. Crabtree and G. W. Brudvig, Anchoring groups for photocatalytic water oxidation on metal oxide surfaces, *Chem. Soc. Rev.*, 2017, **46**, 6099.

12 S. Zhu and D. Wang, Photocatalysis: basic principles, diverse forms of implementations and emerging scientific opportunities, *Adv. Energy Mater.*, 2017, **7**, 1700841.

13 K. M. Young, B. M. Klahr, O. Zandi and T. W. Hamann, Photocatalytic water oxidation with hematite electrodes, *Catal. Sci. Technol.*, 2013, **3**, 1660–1671.

14 W. Tu, W. Guo, J. Hu, H. He, H. Li, Z. Li, W. Luo, Y. Zhou and Z. Zou, State-of-the-art advancements of crystal facet-exposed photocatalysts beyond TiO_2: Design and dependent performance for solar energy conversion and environment applications, *Mater. Today*, 2020, **33**, 75–86.

15 D. Jiang, W. Wang, L. Zhang, Y. Zheng and Z. Wang, Insights into the surface-defect dependence of photoreactivity over CeO_2 nanocrystals with well-defined crystal facets, *ACS Catal.*, 2015, **5**, 4851–4858.

16 G. Liu, C. Y. Jimmy, G. Q. M. Lu and H. M. Cheng, Crystal facet engineering of semiconductor photocatalysts: Motivations, advances and unique properties, *Chem. Commun.*, 2011, **47**, 6763–6783.

17 S. Wang, G. Liu and L. Wang, Crystal facet engineering of photoelectrodes for photoelectrochemical water splitting, *Chem. Rev.*, 2019, **119**, 5192–5247.

18 M. H. Huang, G. Naresh and H. S. Chen, Facet-dependent electrical, photocatalytic, and optical properties

of semiconductor crystals and their implications for applications, *ACS Appl. Mater. Interfaces*, 2018, **10**, 4–15.
19 W. Xu, Y. Bai and Y. Yin, Surface engineering of nanostructured energy materials, *Adv. Mater.*, 2018, **30**, 1802091.
20 S. Bai, L. Wang, Z. Li and Y. Xiong, Facet-engineered surface and interface design of photocatalytic materials, *Adv. Sci.*, 2017, **4**, 1600216.
21 S. Bai, W. Jiang, Z. Li and Y. Xiong, Surface and interface engineering in photocatalysis, *ChemNanoMat*, 2015, **1**, 223–239.
22 M. D'Arienzo, J. Carbajo, A. Bahamonde, M. Crippa, S. Polizzi, R. Scotti, L. Wahba and F. Morazzoni, Photogenerated defects in shape-controlled TiO_2 anatase nanocrystals: A probe to evaluate the role of crystal facets in photocatalytic processes, *J. Am. Chem. Soc.*, 2011, **133**, 17652–17661.
23 M. R. D. Bomio, R. L. Tranquilin, F. V. D. Motta, C. A. Paskocimas, R. M. D. Nascimento, L. Gracia, J. Andres and E. Longo, Toward understanding the photocatalytic activity of $PbMoO_4$ powders with predominant (111), (100), (011), and (110) facets. A combined experimental and theoretical study, *J. Phys. Chem. C*, 2013, **117**(41), 21382–21395.
24 J. Zhu, F. Fan, R. Chen, H. An, Z. Feng and C. Li, Direct imaging of highly anisotropic photogenerated charge separations on different facets of a single $BiVO_4$ photocatalyst, *Angew. Chem.*, 2015, **127**(31), 9239–9242.
25 G. Naresh, P. L. Hsieh, V. Meena, S. K. Lee, Y. H. Chiu, M. Madasu, A. T. Lee, H. Y. Tsai, T. H. Lai, Y. J. Hsu and Y. C. Lo, Facet-dependent photocatalytic behaviors of ZnS-decorated Cu_2O polyhedra arising from tunable interfacial band alignment, *ACS Appl. Mater. Interfaces*, 2018, **11**(3), 3582–3589.
26 L. Sun, L. Xiang, X. Zhao, C. J. Jia, J. Yang, Z. Jin, X. Cheng and W. Fan, Enhanced visible-light photocatalytic activity of BiOI/BiOCl heterojunctions: Key role of crystal facet combination, *ACS Catal.*, 2015, **5**(6), 3540–3551.
27 T. Montini, M. Melchionna, M. Monai and P. Fornasiero, Fundamentals and catalytic applications of CeO_2-based materials, *Chem. Rev.*, 2016, **116**, 5987–6041.
28 J. Xiong, J. Di, J. Xia, W. Zhu and H. Li, Surface defect engineering in 2D nanomaterials for photocatalysis, *Adv. Funct. Mater.*, 2018, **28**, 1801983.
29 X. Sun, X. Zhang and Y. Xie, Surface defects in two-dimensional photocatalysts for efficient organic synthesis, *Matter*, 2020, **2**, 842–861.
30 W. Zhou and H. Fu, Defect-mediated electron–hole separation in semiconductor photocatalysis, *Inorg. Chem. Front.*, 2018, **5**, 1240–1254.
31 M. Kong, Y. Li, X. Chen, T. Tian, P. Fang, F. Zheng and X. Zhao, Tuning the relative concentration ratio of bulk defects to surface defects in TiO_2 nanocrystals leads to high photocatalytic efficiency, *J. Am. Chem. Soc.*, 2011, **133**, 16414–16417.
32 F. Wang, W. Ge, T. Shen, B. Ye, Z. Fu and Y. Lu, The effect of bulk/surface defects ratio change on the photocatalysis of TiO_2 nanosheet film, *Appl. Surf. Sci.*, 2017, **410**, 513–518.
33 F. Bai, L. Xu, X. Zhai, X. Chen and W. Yang, Vacancy in ultrathin 2D nanomaterials toward sustainable energy application, *Adv. Energy Mater.*, 2020, **10**, 1902107.
34 S. Bai, N. Zhang, C. Gao and Y. Xiong, Defect engineering in photocatalytic materials, *Nano Energy*, 2018, **53**, 296–336.
35 Z. Zafar, S. Yi, J. Li, C. Li, Y. Zhu, A. Zada, W. Yao, Z. Liu and X. Yue, Recent development in defects engineered photocatalysts: An overview of the experimental and theoretical strategies, *Energy Environ. Mater.*, 2021, 1–47.
36 H. Li, J. Shang, Z. Ai and L. Zhang, Efficient visible light nitrogen fixation with BiOBr nanosheets of oxygen vacancies on the exposed {001} facets, *J. Am. Chem. Soc.*, 2015, **137**(19), 6393–6399.
37 N. Zhang, X. Li, H. Ye, S. Chen, H. Ju, D. Liu, Y. Lin, W. Ye, C. Wang, Q. Xu and J. Zhu, Oxide defect engineering enables to couple solar energy into oxygen activation, *J. Am. Chem. Soc.*, 2016, **138**(28), 8928–8935.
38 S. Zhang, X. Liu, C. Liu, S. Luo, L. Wang, T. Cai, Y. Zeng, J. Yuan, W. Dong, Y. Pei and Y. Liu, MoS_2 quantum dot growth induced by S vacancies in a $ZnIn_2S_4$ monolayer: Atomic-level heterostructure for photocatalytic hydrogen production, *ACS Nano*, 2018, **12**(1), 751–758.
39 C. Sun, H. Li and L. Chen, Nanostructured ceria-based materials: Synthesis, properties, and applications, *Energy Environ. Sci.*, 2012, **5**, 8475–8505.
40 E. Murray, T. Tsai and S. A. Barnett, A direct-methane fuel cell with a ceria-based anode, *Nature*, 1999, **400**, 649.
41 Z. Shao, S. M. Haile, J. Ahn, D. Ronney, Z. Zhan and S. A. Barnett, A thermally self-sustained micro solid-oxide fuel-cell stack with high power density, *Nature*, 2005, **435**, 795.
42 T. Morimoto, H. Tomonaga and A. Mitani, Ultraviolet ray absorbing coatings on glass for automobiles, *Thin Solid Films*, 1999, **351**, 61–65.
43 S. Zhang, Z. Xia, Y. Zou, F. Cao, Y. Liu, Y. Ma and Y. Qu, Interfacial frustrated Lewis pairs of CeO_2 activate CO_2 for selective tandem transformation of olefins and CO_2 into cyclic carbonates, *J. Am. Chem. Soc.*, 2019, **141**, 11353–11357.
44 M. Mogensen, N. M. Sammes and G. A. Tompsett, Physical, chemical and electrochemical properties of pure and doped ceria, *Solid State Ionics*, 2000, **129**, 63–94.
45 D. Zhang, X. Du, L. Shi and R. Gao, Shape-controlled synthesis and catalytic application of ceria nanomaterials, *Dalton Trans.*, 2012, **41**, 14455–14475.
46 Z. Wang and R. Yu, Hollow micro/nanostructured ceria-based materials: Synthetic strategies and versatile applications, *Adv. Mater.*, 2018, **31**, 1800592.
47 S. Xie, Z. Wang, F. Cheng, P. Zhang, W. Mai and Y. Tong, Ceria and ceria-based nanostructured materials for photoenergy applications, *Nano Energy*, 2017, **34**, 313–337.
48 J. Wang, X. Xiao, Y. Liu, K. Pan, H. Pang and S. Wei, The application of CeO_2-based materials in electrocatalysis, *J. Mater. Chem. A*, 2019, **7**, 17675–17702.
49 J. Graciani, A. M. Márquez, J. J. Plata, Y. Ortega, N. C. Hernández, A. Meyer, C. M. Zicovich-Wilson and J. F. Sanz,

Comparative study on the performance of hybrid DFT functionals in highly correlated oxides: The case of CeO_2 and Ce_2O_3, *J. Chem. Theory Comput.*, 2011, **7**, 56–65.

50 Y. Ma, W. Gao, Z. Zhang, S. Zhang, Z. Tian, Y. Liu, J. C. Ho and Y. Qu, Regulating the surface of nanoceria and its applications in heterogeneous catalysis, *Surf. Sci. Rep.*, 2018, **73**, 1–36.

51 F. A. Kröger and H. J. Vink, Relations between the concentrations of imperfections in crystalline solids, *Solid State Phys.*, 1956, **3**, 307–435.

52 B. Huang, R. Gillen and J. Robertson, Study of CeO_2 and its native defects by density functional theory with repulsive potential, *J. Phys. Chem. C*, 2014, **118**, 24248–24256.

53 Y. P. Lan and H. Y. Sohn, Effect of oxygen vacancies and phases on catalytic properties of hydrogen-treated nanoceria particles, *Mater. Res. Express*, 2018, **5**, 035501.

54 R. C. de Oliveira, R. A. C. Amoresi, N. L. Marana, M. A. Zaghete, M. Ponce, A. J. Chiquito, J. R. Sambrano, E. Longo and A. Z. Simoes, Influence of synthesis time on the morphology and properties of CeO_2 nanoparticles: An experimental–theoretical study, *Cryst. Growth Des.*, 2020, **20**, 5031–5042.

55 Y. Huang, C.-F. Yan, C.-Q. Guo and Y. Shi, Experimental and first-principles DFT study on oxygen vacancies on cerium dioxide and its effect on enhanced photocatalytic hydrogen production, *Int. J. Hydrogen Eng.*, 2016, **41**, 7919–7926.

56 C. R. A. Catlow, Atomistic mechanisms of ionic transport in fast-ion conductors, *Faraday Trans.*, 1990, **86**, 1167–1176.

57 F. Esch, S. Fabris, L. Zhou, T. Montini, C. Africh, P. Fornasiero, G. Comelli and R. Rosei, Electron localization determines defect formation on ceria substrates, *Science*, 2005, **309**, 752–755.

58 R. C. Deus, R. A. C. Amoresi, P. M. Desimone, F. Schipani, L. S. R. Rocha, M. A. Ponce, A. Z. Simoes and E. Longo, Electrical behavior of cerium dioxide films exposed to different gases atmospheres, *Ceram. Int.*, 2016, **42**, 15023–15029.

59 S. Y. Chen, C. H. Tsai, M. Z. Huang, D. C. Yan, T. W. Huang, A. Gloter, C. L. Chen, H. J. Lin, C. T. Chen and C. L. Dong, Concentration dependence of oxygen vacancy on the magnetism of CeO_2 nanoparticles, *J. Phys. Chem. C*, 2012, **116**, 8707–8713.

60 Z. Liu, C. C. Sorrell, P. Koshy and J. N. Hart, DFT study of methanol adsorption on defect-free CeO_2 low-index surfaces, *ChemPhysChem*, 2019, **20**, 2074–2081.

61 M. Nolan, S. C. Parker and G. W. Watson, The electronic structure of oxygen vacancy defects at the low index surfaces of ceria, *Surf. Sci.*, 2005, **595**, 223–232.

62 R. A. Amoresi, R. C. Oliveira, N. L. Marana, P. B. De Almeida, P. S. Prata, M. A. Zaghete, E. Longo, J. R. Sambrano and A. Z. Simoes, CeO_2 nanoparticle morphologies and their corresponding crystalline planes for the photocatalytic degradation of organic pollutants, *ACS Appl. Nano Mater.*, 2019, **2**, 6513–6526.

63 Z. Wu, M. Li, J. Howe, H. M. Meyer III and S. H. Overbury, Probing defect sites on CeO_2 nanocrystals with well-defined surface planes by Raman spectroscopy and O_2 adsorption, *Langmuir*, 2010, **26**, 16595–16606.

64 X. Zheng, Y. Li, L. Zhang, L. Shen, Y. Xiao, Y. Zhang, C. Au and L. Jiang, Insight into the effect of morphology on catalytic performance of porous CeO_2 nanocrystals for H2S selective oxidation, *Appl. Catal., B*, 2019, **252**, 98–110.

65 Y. Xin, X. Yang, P. Jiang, Z. Zhang, Z. Wang and Y. Zhang, Synthesis of CeO_2-based quantum dots through a polyol-hydrolysis method for fuel-borne catalysts, *ChemCatChem*, 2011, **3**, 1772–1778.

66 M. S. Hassan, R. Khan, T. Amna, J. Yang, I. H. Lee, M. Y. Sun, M. H. EL-Newehy, S. S. Al-Deyab and M. S. Khil, The influence of synthesis method on size and toxicity of CeO_2 quantum dots: Potential in the environmental remediation, *Ceram. Int.*, 2016, **42**, 576–582.

67 T. Lehnen, J. Schläfer and S. Mathur, Rapid microwave synthesis of CeO_2 quantum dots, *Z. Anorg. Allg. Chem.*, 2014, **640**, 819–825.

68 D. Arumugam, M. Thangapian, A. Jayaram, G. S. Okram, N. P. Lalla and M. F. B. Amirtham, Induced aggregation of steric stabilizing anionic-rich 2-amino-3-chloro-5-trifluoromethylpyridine on CeO_2 QDs: Surface charge and electro-osmotic flow analysis, *J. Phys. Chem. C*, 2016, **120**, 26544–26555.

69 K. Zhao, J. Qi, H. Yin, Z. Wang, S. Zhao, X. Ma, J. Wan, L. Chang, Y. Gao, R. Yu and Z. Tang, Efficient water oxidation under visible light by tuning surface defects on ceria nanorods, *J. Mater. Chem. A*, 2015, **3**, 20465–20470.

70 F. Cao, M. Zhang, K. Yang, Z. Tian, J. Li and Y. Qu, Single crystalline CeO_2 nanotubes, *Nano Res.*, 2021, **14**, 715–719.

71 B. Dong, L. Li, Z. Dong, R. Xu and Y. Wu, Fabrication of CeO_2 nanorods for enhanced solar photocatalysts, *Int. J. Hydrogen Energy*, 2018, **43**, 5275–5282.

72 S. C. Kuiry, S. D. Patil, S. Deshpe and S. Seal, Spontaneous self-assembly of cerium oxide nanoparticles to nanorods through supraaggregate formation, *J. Phys. Chem. B*, 2005, **109**, 6936–6939.

73 K. L. Yu, G. L. Ruan, Y. H. Ben and J. Zou, Convenient synthesis of CeO_2 nanotubes, *J. Mater. Sci. Eng., B*, 2007, **139**, 197–200.

74 Y. J. Feng, L. L. Liu and X. D. Wang, Hydrothermal synthesis and automotive exhaust catalytic performance of CeO_2 nanotube arrays, *J. Mater. Chem.*, 2011, **21**, 15442–15448.

75 J. Wu, J. Wang, Y. Du, H. Li, Y. Yang and X. Jia, Chemically controlled growth of porous CeO_2 nanotubes for Cr(VI) photoreduction, *Appl. Catal., B*, 2015, **174–175**, 435–444.

76 X. Lu, T. Zhai, H. Cui, J. Shi, S. Xie, Y. Huang, C. Liang and Y. Tong, Redox cycles promoting photocatalytic hydrogen evolution of CeO_2 nanorods, *J. Mater. Chem.*, 2011, **21**, 5569–5572.

77 C. Zhang, X. Zhang, Y. Wang, S. Xie, Y. Liu, X. Lu and Y. Tong, Facile electrochemical synthesis of CeO_2 hierarchical nanorods and nanowires with excellent photocatalytic activities, *New J. Chem.*, 2014, **38**, 2581–2586.

78 T. Yu, B. Lim and Y. Xia, Aqueous-phase synthesis of single-crystal ceria nanosheets, *Angew. Chem., Int. Ed.*, 2010, **49**, 4484–4487.

79 Y. Yu, Y. Zhu and M. Meng, Preparation, formation mechanism and photocatalysis of ultrathin mesoporous single-crystal-like CeO_2 nanosheets, *Dalton Trans.*, 2013, **42**, 12087–12092.

80 Y. Huang, B. Long, M. Tang, Z. Rui, M. S. Balogun, Y. Tong and H. Ji, Bifunctional catalytic material: an ultrastable and high-performance surface defect CeO_2 nanosheets for formaldehyde thermal oxidation and photocatalytic oxidation, *Appl. Catal., B*, 2016, **181**, 779–787.

81 D. Wang, Y. Kang, V. Doan-Nguyen, J. Chen, R. Küngas, N. L. Wieder, K. Bakhmutsky, R. J. Gorte and C. B. Murray, Synthesis and oxygen storage capacity of two-dimensional ceria nanocrystals, *Angew. Chem., Int. Ed.*, 2011, **50**, 4378–4381.

82 T. Taniguchi, Y. Sonoda, M. Echikawa, Y. Watanabe, K. Hatakeyama, S. Ida, M. Koinuma and Y. Matsumoto, Intense photoluminescence from ceria-based nanoscale lamellar hybrid, *ACS Appl. Mater. Interfaces*, 2012, **4**, 1010–1015.

83 H. Ding, J. Yang, S. Ma, N. Yigit, J. Xu, G. Rupprechter and J. Wang, Large dimensional CeO_2 Nanoflakes by microwave-assisted synthesis: Lamellar nano-channels and surface oxygen vacancies promote catalytic activity, *ChemCatChem*, 2018, **10**, 4100–4108.

84 P. Li, Y. Zhou, Z. Zhao, Q. Xu, X. Wang, M. Xiao and Z. Zou, Hexahedron prism-anchored octahedronal CeO_2: Crystal facet-based homojunction promoting efficient solar fuel synthesis, *J. Am. Chem. Soc.*, 2015, **137**, 9547–9550.

85 N. S. Arul, D. Mangalaraj and J. I. Han, Solvothermal synthesis of three-dimensional CeO_2 micropillows and their photocatalytic property, *Phys. Status Solidi RRL*, 2014, **8**, 643–647.

86 C. Sun, J. Sun, G. Xiao, H. Zhang, X. Qiu, H. Li and L. Chen, Mesoscale organization of nearly monodisperse flowerlike ceria microspheres, *J. Phys. Chem. B*, 2006, **110**, 13445–13452.

87 C. Sun, H. Li and L. Chen, Study of flowerlike CeO_2 microspheres used as catalyst supports for CO oxidation reaction, *J. Phys. Chem. Solids*, 2007, **68**, 1785–1790.

88 J. Sun, Y. Wang, J. Li, G. Xiao, L. Zhang, H. Li, Y. Cheng, C. Sun, Z. Cheng, Z. Dong and L. Chen, H_2 production from stable ethanol steam reforming over catalyst of NiO based on flowerlike CeO_2 microspheres, *Int. J. Hydrogen Energy*, 2010, **35**, 3087–3091.

89 P. Ji, J. Zhang, F. Chen and M. Anpo, Ordered mesoporous CeO_2 synthesized by nanocasting from cubic Ia3d mesoporous MCM-48 silica: Formation, characterization and photocatalytic activity, *J. Phys. Chem. C*, 2008, **112**, 17809–17813.

90 S. Fang, Y. Xin, L. Ge, C. Han, P. Qiu and L. Wu, Facile synthesis of CeO_2 hollow structures with controllable morphology by template-engaged etching of Cu_2O and their visible light photocatalytic performance, *Appl. Catal., B*, 2015, **179**, 458–467.

91 J. Qi, K. Zhao, G. Li, Y. Gao, H. Zhao, R. Yu and Z. Tang, Multi-shelled CeO_2 hollow microspheres as superior photocatalysts for water oxidation, *Nanoscale*, 2014, **6**, 4072–4077.

92 N. Lv, J. Zhang, G. Li, X. Wang and J. Ni, Novel strategy for facile synthesis of C-shaped CeO_2 nanotubes with enhanced catalytic properties, *J. Phys. Chem. C*, 2017, **121**, 11926–11931.

93 H.-X. Mai, L.-D. Sun, Y.-W. Zhang, R. Si, W. Feng, H.-P. Zhang, H.-C. Liu and C.-H. Yan, Shape-selective synthesis and oxygen storage behavior of ceria nanopolyhedra, nanorods, and nanocubes, *J. Phys. Chem. B*, 2005, **109**, 24380–24385.

94 Q. Wu, F. Zhang, P. Xiao, H. Tao, X. Wang, Z. Hu and Y. Lü, Great influence of anions for controllable synthesis of CeO_2 nanostructures: From nanorods to nanocubes. *J. Phys. Chem. C*, 2008, 112, 17076–17080.

95 C. Zhu, X. Wei, W. Li, Y. Pu, J. Sun, K. Tang, H. Wan, C. Ge, W. Zou and L. Dong, Crystal-Plane Effects of CeO_2{110} and CeO_2{100} on Photocatalytic CO_2 Reduction: Synergistic Interactions of Oxygen Defects and Hydroxyl Groups, *ACS Sustainable Chem. Eng.*, 2020, **8**, 14397–14406.

96 D. Majumder, I. Chakraborty, K. Mandal and S. Roy, Facet-dependent photodegradation of methylene blue using pristine CeO_2 nanostructures, *ACS Omega*, 2019, **4**(2), 4243–4251.

97 H. Imagawa and S. Sun, Controlled synthesis of monodisperse CeO_2 nanoplates developed from assembled nanoparticles, *J. Phys. Chem. C*, 2012, **116**(4), 2761–2765.

98 H. L. Lin, C. Y. Wu and R. K. Chiang, Facile synthesis of CeO_2 nanoplates and nanorods by [100] oriented growth, *J. Colloid Interface Sci.*, 2010, **341**(1), 12–17.

99 X. Hao, A. Yoko, C. Chen, K. Inoue, M. Saito, G. Seong, S. Takami, T. Adschiri and Y. Ikuhara, Atomic-scale valence state distribution inside ultrafine CeO_2 nanocubes and its size dependence, *Small*, 2018, **14**(42), 1802915.

100 S. Yang and L. Gao, Controlled synthesis and self-assembly of CeO_2 nanocubes, *J. Am. Chem. Soc.*, 2006, **128**(29), 9330–9331.

101 B. Liu, M. Yao, B. Liu, Z. Li, R. Liu, Q. Li, D. Li, B. Zou, T. Cui, G. Zou and J. Liu, High-pressure studies on CeO_2 nano-octahedrons with a (111)-terminated surface., *J. Phys. Chem. C*, 2011, **115**(11), 4546–4551.

102 T. Tsuzuki, R. He, A. Dodd and M. Saunders, Challenges in determining the location of dopants, to study the influence of metal doping on the photocatalytic activities of ZnO nanopowders, *Nanomaterials*, 2019, **9**(3), 481.

103 Y. C. Zhang, Z. Li, L. Zhang, L. Pan, X. Zhang, L. Wang and J. J. Zou, Role of oxygen vacancies in photocatalytic water oxidation on ceria oxide: Experiment and DFT studies, *Appl. Catal., B*, 2018, **224**, 101–108.

104 D. Jiang, W. Wang, E. Gao, S. Sun and L. Zhang, Highly selective defect-mediated photochemical CO_2 conversion over fluorite ceria under ambient conditions, *Chem. Commun.*, 2014, **50**, 2005–2007.

105 M. Aslam, M. T. Qamar, M. T. Soomro, I. M. Ismail, N. Salah, T. Almeelbi, M. A. Gondal and A. Hameed, The effect of sunlight induced surface defects on the photocatalytic activity of nanosized CeO_2 for the degradation of phenol and its derivatives, *Appl. Catal., B*, 2016, **180**, 391–402.

106 A. Hezam, K. Namratha, Q. A. Drmosh, D. Ponnamma, J. Wang, S. Prasad, M. Ahamed, C. Cheng and K. Byrappa, CeO_2 nanostructures enriched with oxygen vacancies for

photocatalytic CO_2 reduction, *ACS Appl. Nano Mater.*, 2019, **3**, 138–148.

107 D. Kandi, S. Martha and K. M. Parida, Quantum dots as enhancer in photocatalytic hydrogen evolution: a review, *Int. J. Hydrogen Energy*, 2017, **42**, 9467–9481.

108 Y. N. Xia, P. D. Yang, Y. G. Sun, Y. Y. Wu, B. Mayers, B. Gates, Y. D. Yin, F. Kim and Y. Q. Yan, One-dimensional nanostructures: Synthesis, characterization, and applications, *Adv. Mater.*, 2003, **15**, 353–389.

109 J. Di, J. Xiong, H. Li and Z. Liu, Ultrathin 2D photocatalysts: Electronic-structure tailoring, hybridization, and applications, *Adv. Mater.*, 2018, **30**, 1704548.

110 Y. Sakamoto, M. Kaneda, O. Terasaki, D. Y. Zhao, J. M. Kim, G. Stucky, H. J. Shin and R. Ryoo, Direct imaging of the pores and cages of three-dimensional mesoporous materials, *Nature*, 2000, **408**, 449–453.

111 H. Du, Y. Wang, H. Ariyan, A. Younis, J. Scott, B. Qu, T. Wan, X. Lin, J. Chen and D. Chu, Design and synthesis of CeO_2 nanowire/MnO_2 nanosheet heterogeneous structure for enhanced catalytic properties, *Mater. Today Commun.*, 2017, **11**, 103–111.

112 C. Jiang, H. Wang, Y. Wang and H. Ji, All solid-state Z-scheme CeO_2/$ZnIn_2S_4$ hybrid for the photocatalytic selective oxidation of aromatic alcohols coupled with hydrogen evolution, *Appl. Catal., B*, 2020, **277**, 119235.

113 H. Jia, A. Du, H. Zhang, J. Yang, R. Jiang, J. Wang and C. Y. Zhang, Site-selective growth of crystalline ceria with oxygen vacancies on gold nanocrystals for near-infrared nitrogen photofixation, *J. Am. Chem. Soc.*, 2019, **141**, 5083–5086.

114 J. X. Feng, S. H. Ye, H. Xu, Y. X. Tong and G. R. Li, Design and synthesis of FeOOH/CeO_2 heterolayered nanotube electrocatalysts for the oxygen evolution reaction, *Adv. Mater.*, 2016, **28**, 4698–4703.

115 Q. Ma, Q. Zhang, S. Chu, J. Guo, H. Li and Z. Lin, ZIF-67-induced double-tubular 1D CeO_2/Co_3O_4 heterostructures allowing electron transfer synergetic mechanism for enhanced photocatalytic performance, *Mater. Lett.*, 2021, **289**, 129391.

116 X. J. Wen, C. Zhang, C. G. Niu, L. Zhang, G. M. Zeng and X. G. Zhang, Highly enhanced visible light photocatalytic activity of CeO_2 through fabricating a novel p–n junction BiOBr/CeO_2, *Catal. Commun.*, 2017, **90**, 51–55.

117 S. Sultana, S. Mansingh and K. M. Parida, Facile synthesis of CeO_2 nanosheets decorated upon BiOI microplate: A surface oxygen vacancy promoted Z-scheme-based 2D-2D nanocomposite photocatalyst with enhanced photocatalytic activity, *J. Phys. Chem. C*, 2018, **122**, 808–819.

118 R. Zhang, X. Ren, S. Hao, R. Ge, Z. Liu, A. M. Asiri, L. Chen, Q. Zhang and X. Sun, Selective phosphidation: an effective strategy toward CoP/CeO_2 interface engineering for superior alkaline hydrogen evolution electrocatalysis, *J. Mater. Chem. A*, 2018, **6**, 1985–1990.

119 X. Yang, Y. Zhang, Y. Wang, C. Xin, P. Zhang, D. Liu, B. B. Mamba, K. K. Kefeni, A. T. Kuvarega and J. Gui, Hollow β-Bi_2O_3@ CeO_2 heterostructure microsphere with controllable crystal phase for efficient photocatalysis, *Chem. Eng. J.*, 2020, **387**, 124100.

120 X. Gong, Y. Q. Gu, N. Li, H. Zhao, C. J. Jia and Y. Du, Thermally stable hierarchical nanostructures of ultrathin MoS_2 nanosheet-coated CeO_2 hollow spheres as catalyst for ammonia decomposition, *Inorg. Chem.*, 2016, **55**, 3992–3999.

121 M. Li, C. Chen, L. Xu, Y. Jia, Y. Liu and X. Liu, Surface defect-rich ceria quantum dots anchored on sulfur-doped carbon nitride nanotubes with enhanced charge separation for solar hydrogen production, *J. Energy Chem.*, 2020, **52**, 51–59.

122 K. Wang, Y. Liang, J. Yang, G. Yang, Z. Zeng, R. Xu and X. Xie, Free-standing and flexible 0D CeO_2 nanodot/1D $La(OH)_3$ nanofiber heterojunction net as a novel efficient and easily recyclable photocatalyst, *Inorg. Chem. Front.*, 2020, **7**, 4701–4710.

123 P. Xia, S. Cao, B. Zhu, M. Liu, M. Shi, J. Yu and Y. Zhang, Designing a 0D/2D S-scheme heterojunction over polymeric carbon nitride for visible-light photocatalytic inactivation of bacteria, *Angew. Chem., Int. Ed.*, 2020, **59**, 5218–5225.

124 M. Zhang, J. Yao, M. Arif, B. Qiu, H. Yin, X. Liu and S. M. Chen, 0D/2D CeO_2/$ZnIn_2S_4$ Z-scheme heterojunction for visible-light-driven photocatalytic H_2 evolution, *Appl. Surf. Sci.*, 2020, **526**, 145749.

125 H. Duan, T. Wang, X. Wu, Z. Su, J. Zhuang, S. Liu, R. Zhu, C. Chen and H. Pang, CeO_2 quantum dots doped Ni-Co hydroxide nanosheets for ultrahigh energy density asymmetric supercapacitors, *Chin. Chem. Lett.*, 2020, **31**, 2330–2332.

126 Q. Li, Z. Yan, N. Wang, Z. Xu, G. Wang and G. Huang, 0D/2D CeO_2 quantum dot/NiO nanoplate supported an ultralow-content Pt catalyst for the efficient oxidation of formaldehyde at room temperature, *Catal. Sci. Technol.*, 2020, **10**, 4030–4041.

127 C. C. Hao, Y. B. Tang, W. L. Shi, F. Y. Chen and F. Guo, Facile solvothermal synthesis of a Z-Scheme 0D/3D CeO_2/$ZnIn_2S_4$ heterojunction with enhanced photocatalytic performance under visible light irradiation, *Chem. Eng. J.*, 2020, **409**, 128168.

128 D. Luo, B. Chen, X. Li, Z. Liu, X. Liu, X. Liu, C. Shi and X. S. Zhao, Three-dimensional nitrogen-doped porous carbon anchored CeO_2 quantum dots as an efficient catalyst for formaldehyde oxidation, *J. Mater. Chem. A*, 2018, **6**, 7897–7902.

129 J. Qian, Z. Chen, H. Sun, F. Chen, X. Xu, Z. Wu, P. Li and W. Ge, Enhanced photocatalytic H_2 production on three-dimensional porous CeO_2/carbon nanostructure. ACS Sustain, *Chem. Eng.*, 2018, **6**, 9691–9698.

130 Y. Ma, Y. Bian, Y. Liu, A. Zhu, H. Wu, H. Cui, D. Chu and J. Pan, Construction of Z-scheme system for enhanced photocatalytic H_2 evolution based on CdS quantum dots/CeO_2 nanorods heterojunction, *ACS Sustainable Chem. Eng.*, 2018, **6**, 2552–2562.

131 Y. Ma, P. Ou, Z. Wang, A. Zhu, L. Lu, Y. Zhang, W. Zeng, J. Song and J. Pan, Interface engineering in CeO_2 (111) facets decorated with CdSe quantum dots for photocatalytic hydrogen evolution, *J. Colloid Interface Sci.*, 2020, **579**, 707–713.

132 S. Sultana, S. Mansingh, M. Scurrell and K. M. Parida, Controlled synthesis of CeO_2NS–Au–CdSQDs ternary nanoheterostructure: A promising visible light responsive photocatalyst for H_2 evolution, *Inorg. Chem.*, 2017, **56**, 12297–12307.

133 D. Ma, D. Sun, Y. Zou, S. Mao, Y. Lv, Y. Wang, J. Li and J. W. Shi, The synergy between electronic anchoring effect and internal electric field in CdS quantum dots decorated dandelion-like Fe–CeO_2 nanoflowers for improved photocatalytic hydrogen evolution, *J. Colloid Interface Sci.*, 2019, **549**, 179–188.

134 B. Luo, G. Liu and L. Wang, Recent advances in 2D materials for photocatalysis, *Nanoscale*, 2016, **8**, 6904–6920.

135 N. Fajrina and M. Tahir, A critical review in strategies to improve photocatalytic water splitting towards hydrogen production, *Int. J. Hydrogen Energy*, 2019, **44**, 540–577.

136 G. A. Olah, Beyond oil and gas: the methanol economy, *Angew. Chem., Int. Ed.*, 2005, **44**, 2636–2639.

137 Z. Liang, R. Shen, Y. H. Ng, P. Zhang, Q. Xiang and X. Li, A review on 2D MoS_2 cocatalysts in photocatalytic H_2 production, *J. Mater. Sci. Technol.*, 2020, **56**, 89.

138 D. Ren, Z. Liang, Y. H. Ng, P. Zhang, Q. Xiang and X. Li, Strongly coupled 2D-2D nanojunctions between P-doped Ni_2S (Ni_2SP) cocatalysts and CdS nanosheets for efficient photocatalytic H_2 evolution, *Chem. Eng. J.*, 2020, **390**, 124496.

139 C. Zhu, Y. Wang, Z. Jiang, F. Xu, Q. Xian, C. Sun, Q. Tong, W. Zou, X. Duan and S. Wang, CeO_2 nanocrystal-modified layered MoS_2/g-C_3N_4 as 0D/2D ternary composite for visible-light photocatalytic hydrogen evolution: Interfacial consecutive multi-step electron transfer and enhanced H_2O reactant adsorption, *Appl. Catal., B*, 2019, **259**, 118072.

140 Z. Jiang, Q. Chen, Q. Zheng, R. Shen, P. Zhang and X. Li, Constructing 1D/2D Schottky-based heterojunctions between $Mn_{0.2}Cd_{0.8}S$ nanorods and Ti_3C_2 nanosheets for boosted photocatalytic H_2 evolution, *Acta Phys.-Chim. Sin.*, 2021, **37**, 2010059.

141 H. Yu, Y. Zhao, C. Zhou, L. Shang, Y. Peng, Y. Cao, L. Z. Wu, C. H. Tung and T. Zhang, Carbon quantum dots/TiO_2 composites for efficient photocatalytic hydrogen evolution, *J. Mater. Chem. A*, 2014, **2**(10), 3344–3351.

142 Z. Shao, X. Meng, H. Lai, D. Zhang, X. Pu, C. Su, H. Li, X. Ren and Y. Geng, Coralline-like Ni_2P decorated novel tetrapod-bundle $Cd_{0.9}Zn_{0.1}S$ ZB/WZ homojunctions for highly efficient visible-light photocatalytic hydrogen evolution, *Chin. J. Catal.*, 2021, **42**, 25.

143 R. Shen, K. He, A. Zhang, N. Li, Y. H. Ng, P. Zhang, J. Hu and X. Li, *In situ* construction of metallic Ni_3C@ Ni core–shell cocatalysts over g-C_3N_4 nanosheets for shell-thickness-dependent photocatalytic H_2 production, *Appl. Catal., B*, 2021, **291**, 120104.

144 R. Shen, X. Lu, Q. Zheng, Q. Chen, Y. H. Ng, P. Zhang and X. Li, Tracking S-scheme charge transfer pathways in Mo_2C/CdS H_2-evolution photocatalysts, *Sol. RRL*, 2021, 2100177.

145 N. Xiao, S. Li, S. Liu, B. Xu, Y. Li, Y. Gao, L. Ge and G. Lu, Novel PtPd alloy nanoparticle-decorated g-C_3N_4 nanosheets with enhanced photocatalytic activity for H_2 evolution under visible light irradiation, *Chin. J. Catal.*, 2019, **40**, 352–361.

146 M. K. Bhunia, K. Yamauchi and K. Takanabe, Harvesting solar light with crystalline carbon nitrides for efficient photocatalytic hydrogen evolution, *Angew. Chem.*, 2014, **126**(41), 11181–11185.

147 Z. Hu, Z. Shen and C. Y. Jimmy, Phosphorus containing materials for photocatalytic hydrogen evolution, *Green Chem.*, 2017, **19**(3), 588–613.

148 X. L. Li, X. J. Wang, J. Y. Zhu, Y. P. Li, J. Zhao and F. T. Li, Fabrication of two-dimensional Ni_2P/$ZnIn_2S_4$ heterostructures for enhanced photocatalytic hydrogen evolution, *Chem. Eng. J.*, 2018, **353**, 15–24.

149 M. Wang, S. Shen, L. Li, Z. Tang and J. Yang, Effects of sacrificial reagents on photocatalytic hydrogen evolution over different photocatalysts, *J. Mater. Sci.*, 2017, **52**(9), 5155–5164.

150 L. Wang, C. Zhu, L. Yin and W. Huang, Construction of Pt–M (M = Co, Ni, Fe)/g-C_3N_4 Composites for Highly Efficient Photocatalytic H_2 Generation, *Acta Phys.-Chim. Sin.*, 2020, **36**, 1907001.

151 S. Sun, X. Zhang, X. Liu, L. Pan, X. Zhang and J. Zou, Design and construction of cocatalysts for photocatalytic water splitting, *Acta Phys.-Chim. Sin.*, 2020, **36**, 1905007.

152 P. Jinbo, S. Sheng, Z. Wei, T. Jie, D. Hongzhi, W. Jinbo, C. Lang, A. Chak-Tong and Y. Shuang-Feng, Recent progress in photocatalytic hydrogen evolution, *Acta Phys.-Chim. Sin.*, 2020, **36**, 1905068.

153 M. Schwarze, D. Stellmach, M. Schröder, K. Kailasam, R. Reske, A. Thomas and R. Schomäcker, Quantification of photocatalytic hydrogen evolution, *Phys. Chem. Chem. Phys.*, 2013, **15**(10), 3466–3472.

154 X. Wang, L. Chen, S. Y. Chong, M. A. Little, Y. Wu, W. H. Zhu, R. Clowes, Y. Yan, M. A. Zwijnenburg, R. S. Sprick and A. I. Cooper, Sulfone-containing covalent organic frameworks for photocatalytic hydrogen evolution from water, *Nat. Chem.*, 2018, **10**(12), 1180–1189.

155 L. Ge and C. Han, Synthesis of MWNTs/g-C_3N_4 composite photocatalysts with efficient visible light photocatalytic hydrogen evolution activity, *Appl. Catal., B*, 2012, **117**, 268–274.

156 G. Zhang, Z. A. Lan and X. Wang, Conjugated polymers: Catalysts for photocatalytic hydrogen evolution, *Angew. Chem., Int. Ed.*, 2016, **55**(51), 15712–15727.

157 Z. Shao, X. Meng, H. Lai, D. Zhang, X. Pu, C. Su, H. Li, X. Ren and Y. Geng, Coralline-like Ni_2P decorated novel tetrapod-bundle $Cd_{0.9}Zn_{0.1}$SZB/WZ homojunctions for highly efficient visible-light photocatalytic hydrogen evolution, *Chin. J. Catal.*, 2021, **42**, 439–449.

158 B. Chen, Y. Ma, L. Ding, L. Xu, Z. Wu, Q. Yuan and W. Huang, Reactivity of hydroxyls and water on a CeO_2(111) thin film surface: The role of oxygen vacancy, *J. Phys. Chem. C*, 2013, **117**, 5800–5810.

159 T. Wu, T. Vegge and H. A. Hansen, Improved electrocatalytic water splitting reaction on CeO_2(111) by strain engineering: A DFT+*U* study, *ACS Catal.*, 2019, **9**, 4853–4861.

160 H. A. Hansen and C. Wolverton, Kinetics and thermodynamics of H_2O dissociation on reduced $CeO_2(111)$, *J. Phys. Chem. C*, 2014, **118**, 27402–27414.

161 D. R. Mullins, P. M. Albrecht, T. L. Chen, F. C. Calaza, M. D. Biegalski, H. M. Christen and S. H. Overbury, Water dissociation on $CeO_2(100)$ and $CeO_2(111)$ thin films, *J. Phys. Chem. C*, 2012, **116**, 19419–19428.

162 D. Van Dao, T. T. Nguyen, T. D. Le, S. H. Kim, J. K. Yang, I. H. Lee and Y. T. Yu, Plasmonically driven photocatalytic hydrogen evolution activity of a Pt-functionalized Au@CeO_2 core–shell catalyst under visible light, *J. Mater. Chem. A*, 2020, **8**, 7687–7694.

163 D. Van Dao, T. T. Nguyen, P. Uthirakumar, Y. H. Cho, G. C. Kim, J. K. Yang, D. T. Tran, T. D. Le, H. Choi, H. Y. Kim and Y. T. Yu, Insightful understanding of hot-carrier generation and transfer in plasmonic Au@CeO_2 core–shell photocatalysts for light-driven hydrogen evolution improvement, *Appl. Catal., B*, 2021, **286**, 119947.

164 M. Sridharan, P. Kamaraj, M. Arthanareeswari, J. Arockiaselvi and E. Sundaravadivel, Quaternary CZTS nanoparticle decorated CeO_2 as a noble metal free p–n heterojunction photocatalyst for efficient hydrogen evolution, *Catal. Sci. Technol.*, 2019, **9**, 3686–3696.

165 D. You, B. Pan, F. Jiang, Y. Zhou and W. Su, CdS nanoparticles/CeO_2 nanorods composite with high-efficiency visible-light-driven photocatalytic activity, *Appl. Surf. Sci.*, 2016, **363**, 154–160.

166 Y. Wang, X. Hao, L. Zhang, Y. Li and Z. Jin, Rational design of all-solid-state 0D/2D $Mn_{0.2}Cd_{0.8}S/CeO_2$ direct Z-scheme for photocatalytic hydrogen evolution, *Energy Fuels*, 2020, **34**, 2599–2611.

167 G. Swain, S. Sultana, B. Naik and K. Parida, Coupling of crumpled-type novel MoS_2 with CeO_2 nanoparticles: A noble-metal-free p–n heterojunction composite for visible light photocatalytic H_2 production, *ACS Omega*, 2017, **2**, 3745–3753.

168 Z. Cheng, F. Wang, T. A. Shifa, C. Jiang, Q. Liu and J. He, Efficient photocatalytic hydrogen evolution *via* band alignment tailoring: Controllable transition from type-I to type-II, *Small*, 2017, **13**, 1702163.

169 X. L. Wang, Y. Xiao, H. Yu, Y. Yang, X. T. Dong and L. Xia, Noble-metal-free MOF derived ZnS/CeO_2 decorated with CuS cocatalyst photocatalyst with efficient photocatalytic hydrogen production character, *ChemCatChem*, 2020, **12**, 5669–5678.

170 J. Hao, W. Zhan, L. Sun, G. Zhuang, X. Wang and X. Han, Combining N,S-codoped C and CeO_2: A unique hinge-like structure for efficient photocatalytic hydrogen evolution, *Inorg. Chem.*, 2019, **59**, 937–942.

171 X. Liu, L. He, X. Chen, L. Du, X. Gu, S. Wang, M. Fu, F. Dong and H. Huang, Facile synthesis of CeO_2/g-C_3N_4 nanocomposites with significantly improved visible-light photocatalytic activity for hydrogen evolution, *Int. J. Hydrogen Energy*, 2019, **44**, 16154–16163.

172 N. Gnanaseelan, M. Latha, A. Mantilla, K. Sathish-Kumar and F. Caballero-Briones, The role of redox states and junctions in photocatalytic hydrogen generation of MoS_2–TiO_2–rGO and CeO_2–$Ce_2Ti_3O_{8.7}$–TiO_2–rGO composites, *Mater. Sci. Semicond. Process.*, 2020, **118**, 105185.

173 W. Zou, Y. Shao, Y. Pu, Y. Luo, J. Sun, K. Ma, C. Tang, F. Gao and L. Dong, Enhanced visible light photocatalytic hydrogen evolution *via* cubic CeO_2 hybridized g-C_3N_4 composite, *Appl. Catal., B*, 2017, **218**, 51–59.

174 W. Zou, B. Deng, X. Hu, Y. Zhou, Y. Pu, S. Yu, K. Ma, J. Sun, H. Wan and L. Dong, Crystal-plane-dependent metal oxide–support interaction in CeO_2/g-C_3N_4 for photocatalytic hydrogen evolution, *Appl. Catal., B*, 2018, **238**, 111–118.

175 C. H. Zeng, S. Xie, M. Yu, Y. Yang, X. Lu and Y. Tong, Facile synthesis of large-area CeO_2/ZnO nanotube arrays for enhanced photocatalytic hydrogen evolution, *J. Power Sources*, 2014, **247**, 545–550.

176 Y. Hao, L. Li, J. Zhang, H. Luo, X. Zhang and E. Chen, Multilayer and open structure of dendritic crosslinked CeO_2–ZrO_2 composite: Enhanced photocatalytic degradation and water splitting performance, *Int. J. Hydrogen Energy*, 2017, **42**, 5916–5929.

177 C. H. Shen, X. J. Wen, Z. H. Fei, Z. T. Liu and Q. M. Mu, Novel Z-scheme $W_{18}O_{49}$/CeO_2 heterojunction for improved photocatalytic hydrogen evolution, *J. Colloid Interface Sci.*, 2020, **579**, 297–306.

178 P. Li, M. Zhang, X. Li, C. Wang, R. Wang, B. Wang and H. Yan, MOF-derived NiO/CeO_2 heterojunction: a photocatalyst for degrading pollutants and hydrogen evolution, *J. Mater. Sci.*, 2020, **55**, 15930–15944.

179 X. Cui, Z. Liu, G. Li, M. Zhang, Y. Song and J. Wang, Self-generating $CeVO_4$ as conductive channel within CeO_2/$CeVO_4$/V_2O_5 to induce Z-scheme-charge-transfer driven photocatalytic degradation coupled with hydrogen production, *Int. J. Hydrogen Energy*, 2019, **44**, 23921–23935.

180 C. Zhu, Q. Xian, Q. He, C. Chen, W. Zou, C. Sun, S. Wang and X. Duan, Edge-rich bicrystalline 1T/2H-MoS_2 cocatalyst-decorated{110} terminated CeO_2 nanorods for photocatalytic hydrogen evolution, *ACS Appl. Mater. Interfaces*, 2021, **13**(30), 35818–35827.

181 J. Qian, Z. Chen, F. Chen, Y. Wang, Z. Wu, W. Zhang, Z. Wu and P. Li, Exploration of CeO_2–CuO quantum dots in situ grown on graphene under hypha assistance for highly efficient solar-driven hydrogen production, *Inorg. Chem.*, 2018, **57**, 14532–14541.

182 Y. Hao, L. Li, D. Liu, H. Yu and Q. Zhou, The synergy of SPR effect and Z-scheme of Ag on enhanced photocatalytic performance of 3DOM Ag/CeO_2-ZrO_2 composite, *Mol. Catal.*, 2018, **447**, 37–46.

183 A. Hezam, J. Wang, Q. A. Drmosh, P. Karthik, M. A. Bajiri, K. Namratha, M. Zare, T. R. Lakshmeesha, S. Shivanna, C. Cheng and B. Neppolian, Rational construction of plasmonic Z-scheme Ag–ZnO–CeO_2 heterostructures for highly enhanced solar photocatalytic H_2 evolution, *Appl. Surf. Sci.*, 2020, **541**, 148457.

184 H. Yu, J. Xu, Z. Liu, Y. Li and Z. Jin, Functionalization of sheet structure MoS_2 with CeO_2–Co_3O_4 for efficient photocatalytic hydrogen evolution, *J. Mater. Sci.*, 2018, **53**, 15271–15284.

185 M. A. Sha, P. C. Meenu, V. S. Sumi, T. C. Bhagya, B. R. Sreelekshmy and S. M. A. Shibli, Tuning of electron transfer by Ni–P decoration on CeO_2–TiO_2 heterojunction for enhancement in photocatalytic hydrogen generation, *Mater. Sci. Semicond. Process.*, 2020, **105**, 104742.

186 S. Chen, J. Duan, P. Bian, Y. Tang, R. Zheng and S. Z. Qiao, Three-dimensional smart catalyst electrode for oxygen evolution reaction, *Adv. Energy Mater.*, 2015, **5**, 1500936.

187 L. Yang, H. Zhou, T. Fan and D. Zhang, Semiconductor photocatalysts for water oxidation: Current status and challenges, *Phys. Chem. Chem. Phys.*, 2014, **16**, 6810–6826.

188 Y. Gorlin and T. F. Jaramillo, A bifunctional nonprecious metal catalyst for oxygen reduction and water oxidation, *J. Am. Chem. Soc.*, 2010, **132**(39), 13612–13614.

189 G. Chen, D. A. Delafuente, S. Sarangapani and T. E. Mallouk, Combinatorial discovery of bifunctional oxygen reduction—water oxidation electrocatalysts for regenerative fuel cells, *Catal. Today*, 2001, **67**(4), 341–355.

190 J. Liu, Y. Zou, B. Jin, K. Zhang and J. H. Park, Hydrogen peroxide production from solar water oxidation, *ACS Energy Lett.*, 2019, **4**(12), 3018–3027.

191 A. R. Jadhav, J. M. C. Puguan and H. Kim, Microwave-assisted synthesis of a stainless steel mesh-supported Co_3O_4 microrod array as a highly efficient catalyst for electrochemical water oxidation, *ACS Sustainable Chem. Eng.*, 2017, **5**(11), 11069–11079.

192 J. W. D. Ng, M. Tang and T. F. Jaramillo, A carbon-free, precious-metal-free, high-performance O_2 electrode for regenerative fuel cells and metal–air batteries, *Energy Environ. Sci.*, 2014, **7**(6), 2017–2024.

193 A. Vignesh, M. Prabu and S. Shanmugam, Porous $LaCo_{1-x}Ni_xO_{3-\delta}$ nanostructures as an efficient electrocatalyst for water oxidation and for a zinc–air battery, *ACS Appl. Mater. Interfaces*, 2016, **8**(9), 6019–6031.

194 K. J. Young, L. A. Martini, R. L. Milot, R. C. Snoeberger III, V. S. Batista, C. A. Schmuttenmaer, R. H. Crabtree and G. W. Brudvig, Light-driven water oxidation for solar fuels, *Coord. Chem. Rev.*, 2012, **256**(21–22), 2503–2520.

195 H. Dau and I. Zaharieva, Principles, efficiency, and blueprint character of solar-energy conversion in photosynthetic water oxidation, *Acc. Chem. Res.*, 2009, **42**(12), 1861–1870.

196 X. Fan, M. S. Balogun, Y. Huang and Y. Tong, Oxygen-deficient three-dimensional porous Co_3O_4 nanowires as an electrode material for water oxidation and energy storage, *ChemElectroChem*, 2017, **4**(10), 2453–2459.

197 B. He, P. Kuang, X. Li, H. Chen, J. Yu and K. Fan, In Situ transformation of Prussian-blue analogue-derived bimetallic carbide nanocubes by water oxidation: Applications for energy storage and conversion, *Chem. – Eur. J.*, 2020, **26**(18), 4052–4062.

198 A. Primo, T. Marino, A. Corma, R. Molinari and H. Garcia, Efficient visible-light photocatalytic water splitting by minute amounts of gold supported on nanoparticulate CeO_2 obtained by a biopolymer templating method, *J. Am. Chem. Soc.*, 2011, **133**, 6930–6933.

199 S. Fang, S. Li, L. Ge, C. Han, P. Qiu and Y. Gao, Synthesis of novel CoO_x decorated CeO_2 hollow structures with an enhanced photocatalytic water oxidation performance under visible light irradiation, *Dalton Trans.*, 2017, **46**, 10578–10585.

200 S. Sultana, S. Mansingh and K. M. Parida, Rational design of light induced self healed Fe based oxygen vacancy rich CeO_2(CeO_2 NS–FeOOH/Fe_2O_3) nanostructure materials for photocatalytic water oxidation and Cr(VI) reduction, *J. Mater. Chem. A*, 2018, **6**, 11377–11389.

201 J. Meng, Y. Zhao, H. Li, R. Chen, X. Sun and X. Sun, Metalloporphyrin immobilized CeO_2: *In situ* generation of active sites and synergistic promotion of photocatalytic water oxidation, *Catal. Sci. Technol.*, 2021, **11**, 2560–2569.

202 X. Li, J. Yu, M. Jaroniec and X. Chen, Cocatalysts for selective photoreduction of CO_2 into solar fuels, *Chem. Rev.*, 2019, **119**, 3962–4179.

203 D. Voiry, H. S. Shin, K. Loh and M. Chhowalla, Low-dimensional catalysts for hydrogen evolution and CO_2 reduction, *Nat. Rev. Chem.*, 2018, **2**, 1–17.

204 N. Kumari, M. A. Haider, M. Agarwal, N. Sinha and S. Basu, Role of reduced CeO_2(110) surface for CO_2 reduction to CO and methanol, *J. Phys. Chem. C*, 2016, **120**, 16626–16635.

205 N. Kumari, N. Sinha, M. A. Haider and S. Basu, CO_2 reduction to methanol on CeO_2(110) surface: A density functional theory study, *Electrochim. Acta*, 2015, **177**, 21–29.

206 S. Ullah, E. C. Lovell, R. J. Wong, T. H. Tan, J. Scott and R. Amal, Light-enhanced CO_2 reduction to CH_4 using nonprecious transition-metal catalysts, *ACS Sustainable Chem. Eng.*, 2020, **8**, 5056–5066.

207 Y. Wang, B. Li, C. Zhang, L. Cui, S. Kang, X. Li and L. Zhou, Ordered mesoporous CeO_2–TiO_2 composites: Highly efficient photocatalysts for the reduction of CO_2 with H_2O under simulated solar irradiation, *Appl. Catal., B*, 2013, **130**, 277–284.

208 J. Jiao, Y. Wei, Z. Zhao, J. Liu, J. Li, A. Duan and G. Jiang, Photocatalysts of 3D ordered macroporous TiO_2-supported CeO_2 nanolayers: Design, preparation, and their catalytic performances for the reduction of CO_2 with H_2O under simulated solar irradiation, *Ind. Eng. Chem. Res.*, 2014, **53**, 17345–17354.

209 Z. Xiong, Z. Lei, Z. Xu, X. Chen, B. Gong, Y. Zhao, H. Zhao, J. Zhang and C. Zheng, Flame spray pyrolysis synthesized ZnO/CeO_2 nanocomposites for enhanced CO_2 photocatalytic reduction under UV-Vis light irradiation, *J. CO_2 Util.*, 2017, **18**, 53–61.

210 Y. Pu, Y. Luo, X. Wei, J. Sun, L. Li, W. Zou and L. Dong, Synergistic effects of Cu_2O-decorated CeO_2 on photocatalytic CO_2 reduction: Surface Lewis acid/base and oxygen defect, *Appl. Catal., B*, 2019, **254**, 580–586.

211 W. Dai, X. Hu, T. Wang, W. Xiong, X. Luo and J. Zou, Hierarchical CeO_2/Bi_2MoO_6 heterostructured nanocomposites for photoreduction of CO_2 into hydrocarbons under visible light irradiation, *Appl. Surf. Sci.*, 2018, **434**, 481–491.

212 S. Ijaz, M. F. Ehsan, M. N. Ashiq, N. Karamat and T. He, Preparation of CdS@ CeO_2 core/shell composite for photocatalytic reduction of CO_2 under visible-light irradiation, *Appl. Surf. Sci.*, 2016, **390**, 550–559.

213 C. Yang, Q. Li, Y. Xia, K. Lv and M. Li, Enhanced visible-light photocatalytic CO_2 reduction performance of $Znln_2S_4$ microspheres by using CeO_2 as cocatalyst, *Appl. Surf. Sci.*, 2019, **464**, 388–395.

214 M. Liang, T. Borjigin, Y. Zhang, B. Liu, H. Liu and H. Guo, Controlled assemble of hollow heterostructured g-C_3N_4@CeO_2 with rich oxygen vacancies for enhanced photocatalytic CO_2 reduction, *Appl. Catal., B*, 2019, **243**, 566–575.

215 M. Li, L. Zhang, M. Wu, Y. Du, X. Fan, M. Wang, L. Zhang, Q. Kong and J. Shi, Mesostructured CeO_2/g-C_3N_4 nanocomposites: Remarkably enhanced photocatalytic activity for CO_2 reduction by mutual component activations, *Nano Energy*, 2016, **19**, 145–155.

216 X. Zhao, J. Guan, J. Li, X. Li, H. Wang, P. Huo and Y. Yan, CeO_2/3D g-C_3N_4 heterojunction deposited with Pt cocatalyst for enhanced photocatalytic CO_2 reduction, *Appl. Surf. Sci.*, 2021, **537**, 147891.

217 S. Q. Liu, S. S. Zhou, Z. G. Chen, C. B. Liu, F. Chen and Z. Y. Wu, An artificial photosynthesis system based on CeO_2 as light harvester and N-doped graphene Cu(II) complex as artificial metalloenzyme for CO_2 reduction to methanol fuel, *Catal. Commun.*, 2016, **73**, 7–11.

218 T. Ye, W. Huang, L. Zeng, M. Li and J. Shi, CeO_{2-x} platelet from monometallic cerium layered double hydroxides and its photocatalytic reduction of CO_2, *Appl. Catal., B*, 2017, **210**, 141–148.

219 C. Mao, J. Wang, Y. Zou, H. Li, G. Zhan, J. Li, J. Zhao and L. Zhang, Anion (O, N, C, and S) vacancies promoted photocatalytic nitrogen fixation, *Green Chem.*, 2019, **21**, 2852–2867.

220 X. Chen, N. Li, Z. Kong, W. J. Ong and X. Zhao, Photocatalytic fixation of nitrogen to ammonia: State-of-the-art advancements and future prospects, *Mater. Horiz.*, 2018, **5**, 9–27.

221 R. Zhang, X. Ren, X. Shi, F. Xie, B. Zheng, X. Guo and X. Sun, Enabling effective electrocatalytic N_2 conversion to NH_3 by the TiO_2 nanosheets array under ambient conditions, *ACS Appl. Mater. Interfaces*, 2018, **10**, 28251–28255.

222 L. Ye, C. Han, Z. Ma, Y. Leng, J. Li, X. Ji, D. Bi, H. Xie and Z. Huang, Ni_2P loading on $Cd_{0.5}Zn_{0.5}S$ solid solution for exceptional photocatalytic nitrogen fixation under visible light, *Chem. Eng. J.*, 2017, **307**, 311–318.

223 S. Sun, X. Li, W. Wang, L. Zhang and X. Sun, Photocatalytic robust solar energy reduction of dinitrogen to ammonia on ultrathin MoS_2, *Appl. Catal., B*, 2017, **200**, 323–329.

224 Y. Zhao, Y. Zhao, G. I. Waterhouse, L. Zheng, X. Cao, F. Teng, L. Z. Wu, C. H. Tung, D. O'Hare and T. Zhang, Layered-double-hydroxide nanosheets as efficient visible-light-driven photocatalysts for dinitrogen fixation, *Adv. Mater.*, 2017, **29**, 1703828.

225 S. Mukherjee, D. A. Cullen, S. Karakalos, K. Liu, H. Zhang, S. Zhao, H. Xu, K. L. More, G. Wang and G. Wu, Metal–organic framework-derived nitrogen-doped highly disordered carbon for electrochemical ammonia synthesis using N_2 and H_2O in alkaline electrolytes, *Nano Energy*, 2018, **48**, 217–226.

226 J. Qi, S. Zhou, K. Xie and S. Lin, Catalytic role of assembled Ce Lewis acid sites over ceria for electrocatalytic conversion of dinitrogen to ammonia, *J. Energy Chem.*, 2021, **60**, 249–258.

227 B. Xu, L. Xia, F. Zhou, R. Zhao, H. Chen, T. Wang, Q. Zhou, Q. Liu, G. Cui, X. Xiong and F. Gong, Enhancing electrocatalytic N_2 reduction to NH_3 by CeO_2 nanorod with oxygen vacancies, *ACS Sustainable Chem. Eng.*, 2019, **7**, 2889–2893.

228 H. Xie, H. Wang, Q. Geng, Z. Xing, W. Wang, J. Chen, L. Ji, L. Chang, Z. Wang and J. Mao, Oxygen vacancies of Cr-doped CeO_2 nanorods that efficiently enhance the performance of electrocatalytic N_2 fixation to NH_3 under ambient conditions, *Inorg. Chem.*, 2019, **58**, 5423–5427.

229 H. Xie, Q. Geng, X. Li, T. Wang, Y. Luo, A. A. Alshehri, K. A. Alzahrani, B. Li, Z. Wang and J. Mao, Ceria-reduced graphene oxide nanocomposite as an efficient electrocatalyst towards artificial N_2 conversion to NH_3 under ambient conditions, *Chem. Commun.*, 2019, **55**, 10717–10720.

230 X. Feng, H. Chen, F. Jiang and X. Wang, One-pot fabrication of a double Z-scheme $CeCO_3OH$/gC_3N_4/CeO_2 photocatalyst for nitrogen fixation under solar irradiation, *Catal. Sci. Technol.*, 2019, **9**, 2849–2857.

231 S. Sultana, S. Mansingh and K. M. Parida, Phosphide protected FeS_2 anchored oxygen defect oriented CeO_2 NS based ternary hybrid for electrocatalytic and photocatalytic N_2 reduction to NH_3, *J. Mater. Chem. A*, 2019, **7**, 9145–9153.

232 S. Mansingh, S. Sultana, R. Acharya, M. K. Ghosh and K. M. Parida, Efficient photon conversion via double charge dynamics CeO_2–$BiFeO_3$ p–n heterojunction photocatalyst promising toward N_2 fixation and phenol–Cr(VI) detoxification, *Inorg. Chem.*, 2020, **59**, 3856–3873.

233 X. Li, J. Xie, C. Jiang, J. Yu and P. Zhang, Review on design and evaluation of environmental photocatalysts, *Front. Environ. Sci. Eng.*, 2018, **12**, 1–32.

234 V. Hasija, P. Raizada, A. Sudhaik, K. Sharma, A. Kumar, P. Singh, S. B. Jonnalagadda and V. K. Thakur, Recent advances in noble metal free doped graphitic carbon nitride based nanohybrids for photocatalysis of organic contaminants in water: A review, *Appl. Mater. Today*, 2019, **15**, 494–524.

235 M. L. Brusseau and J. F. Artiola, Chemical contaminants, in *Environmental and pollution science*, Academic Press, 2019, pp. 175–190.

236 N. Warren, I. J. Allan, J. E. Carter, W. A. House and A. Parker, Pesticides and other micro-organic contaminants in freshwater sedimentary environments—A review, *Appl. Geochem.*, 2003, **18**(2), 159–194.

237 P. Gu, J. Xing, T. Wen, R. Zhang, J. Wang, G. Zhao, T. Hayat, Y. Ai, Z. Lin and X. Wang, Experimental and theoretical calculation investigation on efficient Pb(II) adsorption on etched Ti_3AlC_2 nanofibers and nanosheets, *Environ. Sci.: Nano*, 2018, **5**, 946–955.

238 R. Ma, L. Yin, L. Li, S. Zhang, T. Wen, C. Zhang, X. Wang, Z. Chen, T. Hayat and X. Wang, Comparative investigation of Fe_2O_3 and $Fe_{1-x}S$ nanostructures for uranium decontamination, *ACS Appl. Nano Mater.*, 2018, **1**, 5543–5552.

239 P. Gu, S. Zhang, X. Li, X. Wang, T. Wen, R. Jehan, A. Alsaedi, T. Hayat and X. Wang, Recent advances in layered double hydroxide-based nanomaterials for the removal of radionuclides from aqueous solution, *Environ. Pollut.*, 2018, **240**, 493–505.

240 C. C. Wang, J. R. Li, X. L. Lv, Y. Q. Zhang and G. Guo, Photocatalytic organic pollutants degradation in metal–organic frameworks, *Energy Environ. Sci.*, 2014, **7**, 2831–2867.

241 M. Hepel and J. Luo, Photoelectrochemical mineralization of textile diazo dye pollutants using nanocrystalline WO_3 electrodes, *Electrochim. Acta*, 2001, **47**(5), 729–740.

242 M. L. Marin, L. Santos-Juanes, A. Arques, A. M. Amat and M. A. Miranda, Organic photocatalysts for the oxidation of pollutants and model compounds, *Chem. Rev.*, 2012, **112**(3), 1710–1750.

243 P. Singh and A. Borthakur, A review on biodegradation and photocatalytic degradation of organic pollutants: A bibliometric and comparative analysis, *J. Clean. Prod.*, 2018, **196**, 1669–1680.

244 M. Zhang, Q. Shi, X. Song, H. Wang and Z. Bian, Recent electrochemical methods in electrochemical degradation of halogenated organics: A review, *Environ. Sci. Pollut. Res.*, 2019, **26**(11), 10457–10486.

245 Y. L. Pang, A. Z. Abdullah and S. Bhatia, Review on sonochemical methods in the presence of catalysts and chemical additives for treatment of organic pollutants in wastewater, *Desalination*, 2011, **277**, 1–14.

246 M. Sillanpää, M. C. Ncibi and A. Matilainen, Advanced oxidation processes for the removal of natural organic matter from drinking water sources: A comprehensive review, *J. Environ. Manage.*, 2018, **208**, 56–76.

247 G. Darabdhara, K. Boruah, P. Borthakur, N. Hussain, M. R. Das, T. Ahamad, S. M. Alshehri, V. Malgras, K. C. W. Wu and Y. Yamauchi, Reduced graphene oxide nanosheets decorated with Au–Pd bimetallic alloy nanoparticles towards efficient photocatalytic degradation of phenolic compounds in water, *Nanoscale*, 2016, **8**, 8276–8287.

248 D. Chatterjee and S. Dasgupta, Visible light induced photocatalytic degradation of organic pollutants, *J. Photochem. Photobiol., C*, 2005, **6**(2–3), 186–205.

249 N. Sabari Arul, D. Mangalaraj and T. Whan Kim, Photocatalytic degradation mechanisms of self-assembled rose-flower-like CeO_2 hierarchical nanostructures, *Appl. Phys. Lett.*, 2013, **102**, 223115.

250 S. Yuan, Q. Zhang, B. Xu, Z. Jin, Y. Zhang, Y. Yang, M. Zhang and T. Ohno, Porous cerium dioxide hollow spheres and their photocatalytic performance, *RSC Adv.*, 2014, **4**, 62255–62261.

251 N. Wetchakun, S. Chaiwichain, B. Inceesungvorn, K. Pingmuang, S. Phanichphant, A. I. Minett and J. Chen, $BiVO_4/CeO_2$ nanocomposites with high visible-light-induced photocatalytic activity, *ACS Appl. Mater. Interfaces*, 2012, **4**, 3718–3723.

252 N. S. Arul, D. Mangalaraj, R. Ramachran, A. N. Grace and J. I. Han, Fabrication of CeO_2/Fe_2O_3 composite nanospindles for enhanced visible light driven photocatalysts and supercapacitor electrodes, *J. Mater. Chem. A*, 2015, **3**, 15248–15258.

253 Z. Li, D. Liu, W. Huang, Y. Sun, S. Li and X. Wei, Applying facilely synthesized CuO/CeO_2 photocatalyst to accelerate methylene blue degradation in hypersaline wastewater, *Surf. Interface Anal.*, 2019, **51**, 336–344.

254 J. Tian, Y. Sang, Z. Zhao, W. Zhou, D. Wang, X. Kang, H. Liu, J. Wang, S. Chen, H. Cai and H. Huang, Enhanced photocatalytic performances of CeO_2/TiO_2 nanobelt heterostructures, *Small*, 2013, **9**, 3864–3872.

255 S. Ameen, M. S. Akhtar, H. K. Seo and H. S. Shin, Solution-processed CeO_2/TiO_2 nanocomposite as potent visible light photocatalyst for the degradation of bromophenol dye, *Chem. Eng. J.*, 2014, **247**, 193–198.

256 R. Lamba, A. Umar, S. K. Mehta and S. K. Kansal, CeO_2ZnO hexagonal nanodisks: Efficient material for the degradation of direct blue 15 dye and its simulated dye bath effluent under solar light, *J. Alloys Compd.*, 2015, **620**, 67–73.

257 L. Zhu, H. Li, P. Xia, Z. Liu and D. Xiong, Hierarchical ZnO decorated with CeO_2 nanoparticles as the direct Z-scheme heterojunction for enhanced photocatalytic activity, *ACS Appl. Mater. Interfaces*, 2018, **10**, 39679–39687.

258 D. Channei, K. Chansaenpak, P. Jannoey and S. Phanichphant, The staggered heterojunction of CeO_2/CdS nanocomposite for enhanced photocatalytic activity, *Solid State Sci.*, 2019, **96**, 105951.

259 S. Gu, Y. Chen, X. Yuan, H. Wang, X. Chen, Y. Liu, Q. Jiang, Z. Wu and G. Zeng, Facile synthesis of CeO_2 nanoparticle sensitized CdS nanorod photocatalyst with improved visible-light photocatalytic degradation of rhodamine B, *RSC Adv.*, 2015, **5**, 79556–79564.

260 X. Zhang, N. Zhang, Y. J. Xu and Z. R. Tang, One-dimensional CdS nanowires–CeO_2 nanoparticles composites with boosted photocatalytic activity, *New J. Chem.*, 2015, **39**, 6756–6764.

261 X. Liu, F. Meng, B. Yu and H. Wu, Self-assembly synthesis of flower-like CeO_2/MoS_2 heterojunction with enhancement of visible light photocatalytic activity for methyl orange, *J. Mater. Sci.: Mater. Electron.*, 2020, **31**, 6690–6697.

262 M. M. Sabzehmeidani, H. Karimi and M. Ghaedi, Visible light-induced photo-degradation of methylene blue by n–p heterojunction CeO_2/CuS composite based on ribbon-like CeO_2 nanofibers *via* electrospinning, *Polyhedron*, 2019, **170**, 160–171.

263 X. She, H. Xu, H. Wang, J. Xia, Y. Song, J. Yan, Y. Xu, Q. Zhang, D. Du and H. Li, Controllable synthesis of CeO_2/gC_3N_4 composites and their applications in the environment, *Dalton Trans.*, 2015, **44**, 7021–7031.

264 X. Wei, X. Wang, Y. Pu, A. Liu, C. Chen, W. Zou, Y. Zheng, J. Huang, Y. Zhang, Y. Yang and M. Naushad, Facile ball-milling synthesis of CeO_2/g-C_3N_4 Z-scheme heterojunction for synergistic adsorption and photodegradation of methylene blue: Characteristics, kinetics, models, and mechanisms, *Chem. Eng. J.*, 2020, 127719.

265 A. Subashini, P. V. Prasath, S. Sagadevan, J. A. Lett, I. Fatimah, F. Mohammad, H. A. Al-Lohedan, S. F. Alshahateet and W. C. Oh, Enhanced photocatalytic degradation efficiency of graphitic carbon nitride-loaded CeO_2 nanoparticles, *Chem. Phys. Lett.*, 2021, **769**, 138441.

266 W. Ming Yan, Z. Wei, Z. Dong En, L. Shu An, M. Wei Xing, T. Zhi Wei and C. Jun, CeO_2 hollow nanospheres decorated reduced graphene oxide composite for efficient photocatalytic dye-degradation, *Mater. Lett.*, 2014, **137**, 229–232.

267 R. Verma and S. K. Samdarshi, *In situ* decorated optimized CeO_2 on reduced graphene oxide with enhanced adsorptivity and visible light photocatalytic stability and reusability, *J. Phys. Chem. C*, 2016, **120**, 22281–22290.

268 T. Feng, X. Wang and G. Feng, Synthesis of novel CeO_2 microspheres with enhanced solar light photocatalyic properties, *Mater. Lett.*, 2013, **100**, 36–39.

269 J. W. Ko, J. H. Kim and C. B. Park, Synthesis of visible light-active CeO_2 sheets *via* mussel-inspired $CaCO_3$ mineralization, *J. Mater. Chem. A*, 2013, **1**, 241–245.

270 Y. C. Zhang, M. Lei, K. Huang, C. Liang, Y. J. Wang, S. S. Ding, R. Zhang, D. Y. Fan, H. J. Yang and Y. G. Wang, A facile route to mono-dispersed CeO_2 nanocubes and their enhanced photocatalytic properties, *Mater. Lett.*, 2014, **116**, 46–49.

271 F. Chen, Y. Cao and D. Jia, Preparation and photocatalytic property of CeO_2 lamellar, *Appl. Surf. Sci.*, 2011, **257**, 9226–9231.

272 M. Xu, S. Xie, X.-H. Lu, Z.-Q. Liu, Y. Huang, Y. Zhao, J. Ye and Y.-X. Tong, Controllable electrochemical synthesis and photocatalytic activity of CeO_2 octahedra and nanotubes, *J. Electrochem. Soc.*, 2011, **158**, E41–E44.

273 M. M. Khan, S. A. Ansari, M. O. Ansari, B. Min, J. Lee and M. H. Cho, Biogenic fabrication of Au@CeO_2 nanocomposite with enhanced visible light activity, *J. Phys. Chem. C*, 2014, **118**, 9477–9484.

274 L. Huang, Y. Li, H. Xu, Y. Xu, J. Xia, K. Wang, H. Li and X. Cheng, Synthesis and characterization of CeO_2/g-C_3N_4 composites with enhanced visible-light photocatatalytic activity, *RSC Adv.*, 2013, **3**, 22269–22279.

275 S. Xing, T. Li, Y. Gao and J. Liu, Insight into the mechanism for photocatalytic degradation of ciprofloxacin with CeO_2, *Optik*, 2019, **183**, 266–272.

276 H. Wang, B. Liao, T. Lu, Y. Ai and G. Liu, Enhanced visible-light photocatalytic degradation of tetracycline by a novel hollow BiOCl@CeO_2 heterostructured microspheres: Structural characterization and reaction mechanism, *J. Hazard. Mater.*, 2020, **385**, 121552.

277 J. Shen, J. Shen, W. Zhang, X. Yu, H. Tang, M. Zhang and Q. Liu, Built-in electric field induced CeO_2/Ti_3C_2-MXene Schottky-junction for coupled photocatalytic tetracycline degradation and CO_2 reduction, *Ceram. Int.*, 2019, **45**, 24146–24153.

278 Z. Ye, J. Li, M. Zhou, H. Wang, Y. Ma, P. Huo, L. Yu and Y. Yan, Well-dispersed nebula-like ZnO/CeO_2@ HNTs heterostructure for efficient photocatalytic degradation of tetracycline, *Chem. Eng. J.*, 2016, **304**, 917–933.

279 X. J. Wen, C. G. Niu, L. Zhang, C. Liang and G. M. Zeng, A novel Ag_2O/CeO_2 heterojunction photocatalysts for photocatalytic degradation of enrofloxacin: possible degradation pathways, mineralization activity and an in depth mechanism insight, *Appl. Catal., B*, 2018, **221**, 701–714.

280 B. Wu, C. Shan, X. Zhang, H. Zhao, S. Ma, Y. Shi, J. Yang, H. Bai and Q. Liu, CeO_2/Co_3O_4 porous nanosheet prepared using rose petal as biotemplate for photo-catalytic degradation of organic contaminants, *Appl. Surf. Sci.*, 2020, **543**, 148677.

281 X. Yang, Y. Zhang, Y. Wang, C. Xin, P. Zhang, D. Liu, B. B. Mamba, K. K. Kefeni, A. T. Kuvarega and J. Gui, Hollow β-Bi_2O_3@CeO_2 heterostructure microsphere with controllable crystal phase for efficient photocatalysis, *Chem. Eng. J.*, 2020, **387**, 124100.

282 W. Liu, J. Zhou and J. Yao, Shuttle-like CeO_2/g-C_3N_4 composite combined with persulfate for the enhanced photocatalytic degradation of norfloxacin under visible light, *Ecotoxicol. Environ. Safety*, 2020, **190**, 110062.

283 H. Qi, C. Shi, X. Jiang, M. Teng, Z. Sun, Z. Huang, D. Pan, S. Liu and Z. Guo, Constructing CeO_2/nitrogen-doped carbon quantum dot/gC_3N_4 heterojunction photocatalysts for highly efficient visible light photocatalysis, *Nanoscale*, 2020, **12**, 19112–19120.

284 R. Ji, Z. Zhu, W. Ma, X. Tang, Y. Liu and P. Huo, A heterojunction photocatalyst constructed by the modification of 2D-CeO_2 on 2D-MoS_2 nanosheets with enhanced degrading activity, *Catal. Sci. Technol.*, 2020, **10**, 788–800.

285 R. Ma, S. Zhang, L. Li, P. Gu, T. Wen, A. Khan, S. Li, B. Li, S. Wang and X. Wang, Enhanced visible-light-induced photoactivity of type-II CeO_2/g-C_3N_4 nanosheet toward organic pollutants degradation, *ACS Sustainable Chem. Eng.*, 2019, **7**, 9699–9708.

286 Q. Gao, Y. Cui, S. Wang, B. Liu and C. Liu, Enhanced photocatalytic activation of peroxymonosulfate by CeO_2 incorporated ZnCo–layered double hydroxide toward organic pollutants removal, *Sep. Purif. Technol.*, 2021, **263**, 118413.

287 B. Yu, F. Meng, T. Zhou, A. Fan, Z. Zhao and M. Wasim Khan, Construction of CoS/CeO_2 heterostructure nanocages with enhanced photocatalytic performance under visible light, *J. Am. Ceram. Soc.*, 2020, **103**, 6136–6148.

288 Y. Chai, L. Zhang, Q. Liu, F. Yang and W. L. Dai, Insights into the relationship of the heterojunction structure and excellent activity: Photo-oxidative coupling of benzylamine on CeO_2-rod/g-C_3N_4 hybrid under mild reaction conditions, *ACS Sustainable Chem. Eng.*, 2018, **6**, 10526–10535.

289 A. Azimi, A. Azari, M. Rezakazemi and M. Ansarpour, Removal of heavy metals from industrial wastewaters: A review, *ChemBioEng Rev.*, 2017, **4**, 37–59.

290 A. Ayangbenro and O. Babalola, A new strategy for heavy metal polluted environments: A review of microbial biosorbents, *Int. J. Environ. Res. Publ. Health*, 2017, **14**, 94.

291 C. E. Barrera-Díaz, V. Lugo-Lugo and B. Bilyeu, A review of chemical, electrochemical and biological methods for aqueous Cr(VI) reduction, *J. Hazard. Mater.*, 2012, **223**, 1–12.

292 D. K. Padhi and K. Parida, Facile fabrication of α-FeOOH nanorod/RGO composite: A robust photocatalyst for reduction of Cr(VI) under visible light irradiation, *J. Mater. Chem. A*, 2014, **2**, 10300–10312.

293 Y. Li, Z. Liu, Y. Wu, J. Chen, J. Zhao, F. Jin and P. Na, Carbon dots–TiO_2 nanosheets composites for photoreduction of Cr(VI)

under sunlight illumination: Favorable role of carbon dots, *Appl. Catal., B*, 2018, **224**, 508–517.

294 Q. Meng, Y. Zhou, G. Chen, Y. Hu, C. Lv, L. Qiang and W. Xing, Integrating both homojunction and heterojunction in QDs self-decorated Bi_2MoO_6/BCN composites to achieve an efficient photocatalyst for Cr(VI) reduction, *Chem. Eng. J.*, 2018, **334**, 334–343.

295 S. Peng, J. Yang, L. Guo, J. Wang, J. Zhao, J. Xu and Z. Li, Shape-dependent CeO_2@ BiOI for degradation of aqueous Cr(VI), *Adv. Mater. Interfaces*, 2020, **7**, 1901879.

296 Y. Xiao, S. Tan, D. Wang, J. Wu, T. Jia, Q. Liu, Y. Qi, X. Qi, P. He and M. Zhou, $CeO_2/BiOIO_3$ heterojunction with oxygen vacancies and Ce^{4+}/Ce^{3+} redox centers synergistically enhanced photocatalytic removal heavy metal, *Appl. Surf. Sci.*, 2020, **530**, 147116.

297 J. Yang, Y. Liang, K. Li, G. Yang and S. Yin, One-step low-temperature synthesis of 0D CeO_2 quantum dots/2D BiOX (X = Cl, Br) nanoplates heterojunctions for highly boosting photo-oxidation and reduction ability, *Appl. Catal., B*, 2019, **250**, 17–30.

298 G. Yang, Y. Liang, K. Li, J. Yang, R. Xu and X. Xie, Construction of a Ce^{3+} doped CeO_2/Bi_2MoO_6 heterojunction with a mutual component activation system for highly enhancing the visible-light photocatalytic activity for removal of TC or Cr(VI), *Inorg. Chem. Front.*, 2019, **6**, 1507–1517.

299 H. Shen, M. Lin, L. Wang, Z. Huang, X. Wu, X. Jiang, Q. Li, C. L. Chen, J. Zhao, G. Jing and C. S. Yuan, Experimental and theoretical investigation of the enhancement of the photo-oxidation of Hg^0 by CeO_2-modified morphology-controlled anatase TiO_2, *J. Hazard. Mater.*, 2020, **406**, 124535.

300 S. Li, J. Cai, X. Wu, B. Liu, Q. Chen, Y. Li and F. Zheng, TiO_2@ Pt@ CeO_2 nanocomposite as a bifunctional catalyst for enhancing photo-reduction of Cr(VI) and photo-oxidation of benzyl alcohol, *J. Hazard. Mater.*, 2018, **346**, 52–61.

301 L. Kashinath, K. Namratha and K. Byrappa, Microwave mediated synthesis and characterization of CeO_2–GO hybrid composite for removal of chromium ions and its antibacterial efficiency, *J. Environ. Sci.*, 2019, **76**, 65–79.

302 L. Guo, J. Yang, H. Zhang, R. Wang, J. Xu and J. Wang, Highly enhanced visible-light photocatalytic activity *via* a novel surface structure of CeO_2/g-C_3N_4 toward removal of 2,4-dichlorophenol and Cr(VI), *ChemCatChem*, 2021, **13**, 2034–2044.

303 T. Jia, J. Wu, Y. Xiao, Q. Liu, Q. Wu, Y. Qi and X. Qi, Self-grown oxygen vacancies-rich CeO_2/BiOBr Z-scheme heterojunction decorated with rGO as charge transfer channel for enhanced photocatalytic oxidation of elemental mercury, *J. Colloid Interface Sci.*, 2020, **587**, 402–416.

304 J. Bai, X. Wang, G. Han, Z. Xie and G. Diao, CQDs decorated oxygen vacancy-rich CeO_2/BiOCl heterojunctions for promoted visible light photoactivity towards chromium(VI) reduction and rhodamine B degradation, *J. Alloys Compd.*, 2020, **859**, 157837.